Chapter 1

Introduction

From the viewpoint of fundamental condensed-matter physics, over three past decades, the quasi-one-dimensional (Q1D) systems has attracted many experimental and theoretical researchers to explore the physics inside them. For the field of electrical transport, different materials may correspond to different topics in which the sample dimensions, characteristic lengths (e.g. elastic mean free path, phase coherent length …), band structure, type of defects, geometric structure inside, dimensions of electrons and phonons, and etc., are concerned. Recently, the techniques for synthesizing Q1D and nanowires (NWs) systems are extensively developed for many kinds of materials. Some of them, such as carbon nanotubes (CNTs) and Zinc oxide (ZnO), have not only the potential of application but also the novel properties for fundamental research [1][4].

New bottom-up growth methods, combining with well developed top-down techniques, result in various kinds of interesting Q1D and NW-related structures, such as nanotubes, axial heterostructures, radial core-shell heterostructures [2], cross-wire devices, coded NWs [3], NW QDs [5][6], and so on. Various Q1D and NW structures imply various probable functionalities, such as field-effect transistors (FETs), logic circuits, memories, photonic emitters and detectors, biological and chemical sensors, and so on [1][6].

To accomplish the fascinating applications with NWs, fair understanding of the intrinsic electronic transport processes in the NWs is the first and key step for the realization of the promising applicability. However, although numerous NW systems are successfully synthesized, intrinsic electrical characterizations on individual NWs have been comparatively less reported. In most of the experiments, the electrical measurements were performed on the NW devices with two electrical contacts or FET structures. In that way, the influence of contacts can not be explicitly excluded and the properties of individual NWs can not be determined in an unambiguous way. It is why we emphasize in the context that the NWs devices were fabricated to contact with more than four electrodes in order to perform four-probe measurements and extract the intrinsic electrical properties.

The growth of NWs with the bottom-up methods, in contrast to conventional top-down methods, possesses several advantages, one of which is that the single-crystalline structure and desirable lattice orientations are easier to achieve. In this thesis, four kinds of single-crystalline NWs, including Sn-doped In_2O_3 (indium tin oxide, ITO), natively doped

ZnO, indium-doped ZnO (In:ZnO), and lead-doped ZnO (Pb:ZnO) are synthesized by the thermal evaporation method (for the former two) or the laser-assisted chemical vapor deposition (CVD) (for the later two).

ITO is a transparent conducting oxide which is widely used in the optoelectronic industrial. In view of the nanoelectronic and optoelectronic applications, it is very useful to clarify whether the ITO NWs still preserve the desirable electrical properties, such as metallic conduction and low resistivities. Thus far, there have been only a few reports on charge-transport measurements of single ITO NWs. Besides, those measurements were performed on a two-probe configuration where the contributions from contact resistances and lithographic electrode resistances could not be excluded.

ZnO is a very promising material for application. There are several distinct properties as follows. The theoretical calculation showed that ZnO could be a candidate of room-temperature dilute magnetic semiconductor which is the key material for spintronics [7] [7]. The direct bandgap (~3.4 eV) and higher exciton binding energy, 60 meV, which is much larger than that of GaN (25 meV) and the thermal energy at room temperature, can ensure an efficient exciton emission at room temperature. Hence, ZnO is recognized as a potential photonic material in the blue-UV region. The electrical property of single ZnO NWs is easy to be affected by the ambient gases [3]. It implies that the surface related electrical conduction may dominate the whole electrical property when ZnO NWs possess the structure with high surface-volume ratio. This property could be useful for chemical or biological sensors. For those potential applications, it is valuable and necessary to clarify the intrinsic electrical properties inside the ZnO NWs.

To realize electronic applications in a certain semiconductor, the related doped types may play the same important roles as the undoped type. Therefore various doped ZnO NWs were synthesized. The dopants may cause considerable changes in the host material. For example, after doping, both the In- and Pb- doped ZnO NWs were changed from semiconducting to metallic and showed the feature of degenerate Fermi gas. For these systems, the quantum interference effects will be more significant and act as the power probe to understand the microscopic properties inside the NWs [8], especially the surface-related conduction processes.

Here is an overview of this thesis. Chapter 2 contains the experimental methods for fabricating single NW devices and electrical measurements. Chapter 3 is the study of intrinsic electrical transport in single ITO NWs. Chapter 4 is the study of electrical transport in natively doped ZnO NWs. Chapter 5 contains the study of electrical transport in In-doped and

Pb-doped ZnO NWs. Chapter 6 is the conclusion and the suggestion for the future work.

Chapter 2

Sample fabrication and measurement setup

2.1 Growth of nanowires [9][10]

The NWs used in our work are provided by Profs. Fu-Rong Chen and Ji-Jung Kai's group at the Department of Engineering and System Science of National Tsing Hua University (ITO and natively doped ZnO) and by Prof. Jia G. Lu's group at the Department of Physics and Department of Electrical Engineering of University of Southern California (In:ZnO and Pb:ZnO). The fabrication processes are briefly introduced here.

ITO and natively doped NWs are synthesized on silicon or quartz substrates by the thermal evaporation method. Gold nanoparticles with a diameter of 20 to 40 nm are first dispersed on the substrates as catalysts. Mixtures of source materials (e.g. pure ZnO powders) were placed in the middle of a horizontal quartz tube. The substrates are placed on the downstream side of the gas flow. An argon gas is input from one end of the quartz tube and the pumping speed at the other (downstream) end is adjusted to maintain an atmosphere of 50 to 200 Pa in the tube. The source powders are heated to higher temperature (e.g. 950 ℃ for ZnO) for several hours, while the nearby substrate temperature is set to a lower suitable temperature, depending on the NW materials (e.g. ~500 ℃ for ZnO). Finally, NWs are formed on the substrates.

The In-doped and Pb-doped ZnO NWs are synthesized by the laser-assisted chemical vapor deposition (CVD) method [11]. Pure zinc powder is placed in the center of the furnace, where the temperature is elevated to 650 °C to generate zinc vapor in argon (Ar) under 1 atm pressure. Oxygen (23 ppm) diluted by Ar is kept flowing at a rate of 220 sccm. With In-doped ZnO as the example, pure indium powder is simultaneously ablated from upstream under Nd:YAG (yttrium-aluminum-garnet) laser pulses. Consequently, In-doped ZnO NWs are formed on tin-coated (5 nm) silicon substrates via the catalyst assisted vapor-liquid-solid (VLS) process [12].

2.2 Fabrication of single NW devices

Figure 2.1 shows the schematic flow chart of the fabrication for the individual NW devices. We first make micron-sized Ti/Au (10/60 nm) metal pads and coordinate marks by utilizing the standard photolithography and lift-off techniques on silicon substrates capped

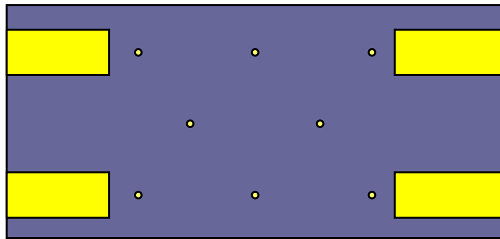

A substrate with larger metal pattern and coordinate marks is made by photo-lithography processes.

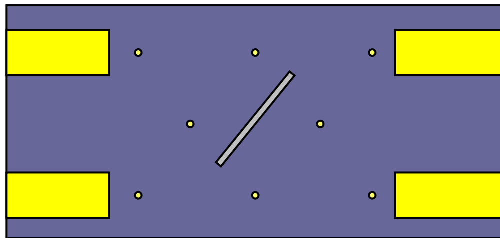

Some NWs are transferred onto the substrate. After inspection by SEM, we choose the suitable one and define its location.

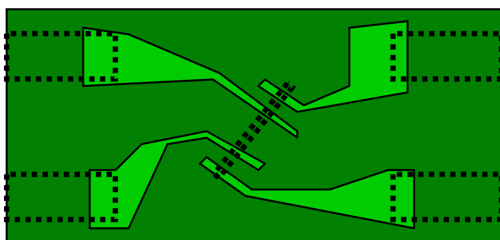

After a layer of PMMA is spin-coated on the substrate, we control the electron -beam exposure system to expose a specific area defined by a CAD software.

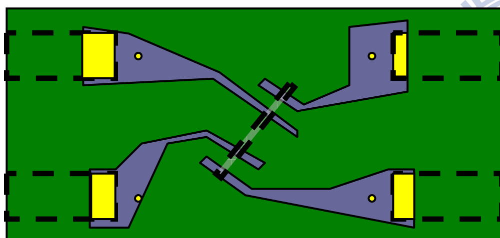

The exposed PMMA is developed and removed in a solvent (MIBK:IPA=1:3). Then, perform one-minute O2-plasma for cleaning out the remaining PMMA.

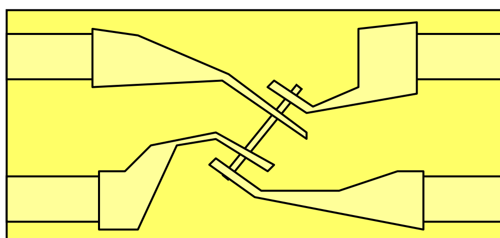

Deposit metal films (e.g. Ti/Au) with thermal or E-gun evaporator.

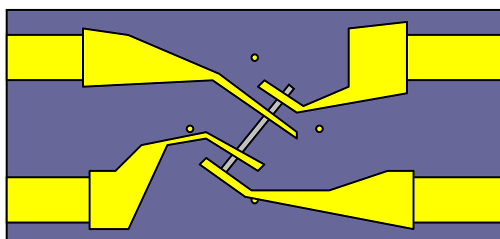

After lift-off, the submicron electrodes are connected to the NW. If necessary, post-annealing is performed at 300 ℃ for 10 to 20 minutes.

Figure 2.1: A schematic flow chart of fabricating the single NW devices.

with a 400 nm thick SiO_2 layer (We call these substrates as SiO_2/Si substrates.). NWs are then dispersed on the SiO_2/Si substrates by bringing the patterned SiO_2/Si substrates to loosely contact with the substrate where many NWs were already grown onto. After inspecting the SiO2/Si substrates by SEM, we choose the suitable NWs and define their locations. We design the specific pattern area for electron-beam exposure by a CAD software. After a layer of PMMA (specification no.: A5-950) is spin-coated on the substrate, we operate the electron -beam exposure system to expose the area we designed. The exposed PMMA is developed and removed in a solvent (MIBK:IPA=1:3). An inspection under the optical microscope is needed to make sure the pattern is right and no significant shift. Before depositing metal films (e.g. Ti/Au ~ 20/100 nm) on the substrates, it is important to perform one-minute O_2-plasma (plasma power~20 W, 0.1 Torr O_2 pressure) for cleaning out the remaining PMMA. The metallization is done by the thermal or E-gun evaporator. After lift-off with dipping the substrates in acetone, the submicron electrodes are formed and connected to the NW as shown in the left-up inset of Figure 2.2. For semiconducting NWs, e.g. undoped ZnO NWs, post-annealing is suggested to perform at 300 ℃ for 10 to 20 minutes in high vacuum to reduce the contact resistance. This process may cause the alloy effect at the interface of metal and semiconductor and make the width of Schottky barrier thinning. In our experience, lower contact resistance can earn better signal to noise ratio in the electrical measurements. For metallic NWs, e.g. ITO NWs,, the post-annealing only has slight effect, thus it's no need to perform this process.

2.3 Methods of electrical measurements

Copper leads are attached to the macro-electrodes with Ag paste, and the substrate is thermally anchored to the sample holder of the cryostat as shown in the Figure 2.2 and its right-down inset. The Figure 2.3 shows the equivalent circuits for two- and four- probe measurement. The R_i, i=1, 2, 3, are the NW resistances in different segments. The R_{ci}, i=1, 2, 3, 4, are the contact resistances within different interfaces between NW and metal electrodes. In the upper scheme, the measured resistance will be $R_{c2}+R_2+R_{c3}$ in the two-probe configuration In the lower scheme of four-probe configuration, if we fit to the condition that the input impedance of voltage meter, R_v, is much larger than the NW resistance R_2 and contact resistances R_{c2} and R_{c3}, the measured resistance will be relatively close to the R_2 which reveals the intrinsic electrical properties of the NW.

The current source and voltage meter in the Figure 2.3 can be organized in two different

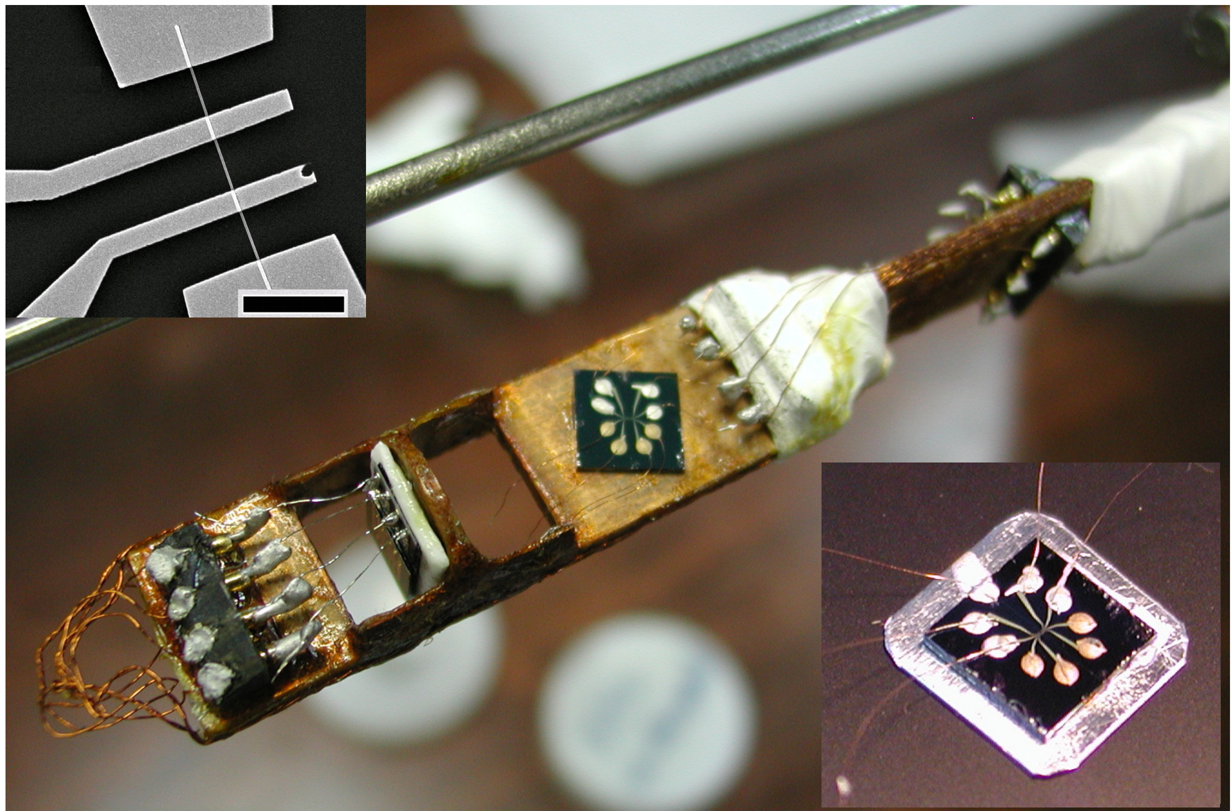

Figure 2.2: Two samples are fixed on the sample holder of ^{3}He cryostat. There are two areas for different magnetic field orientations. The left-up inset is a SEM image of a single ZnO NW device. The scale bar is 5 μm. The right-down inset is the whole view of a sample on which several copper wires are already connected. The chip size is 0.7 x 0.7 cm^2.

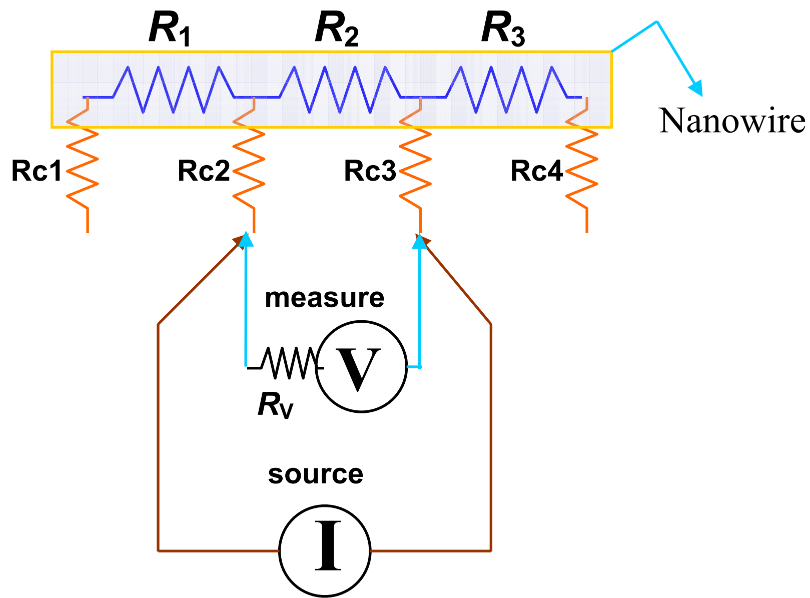

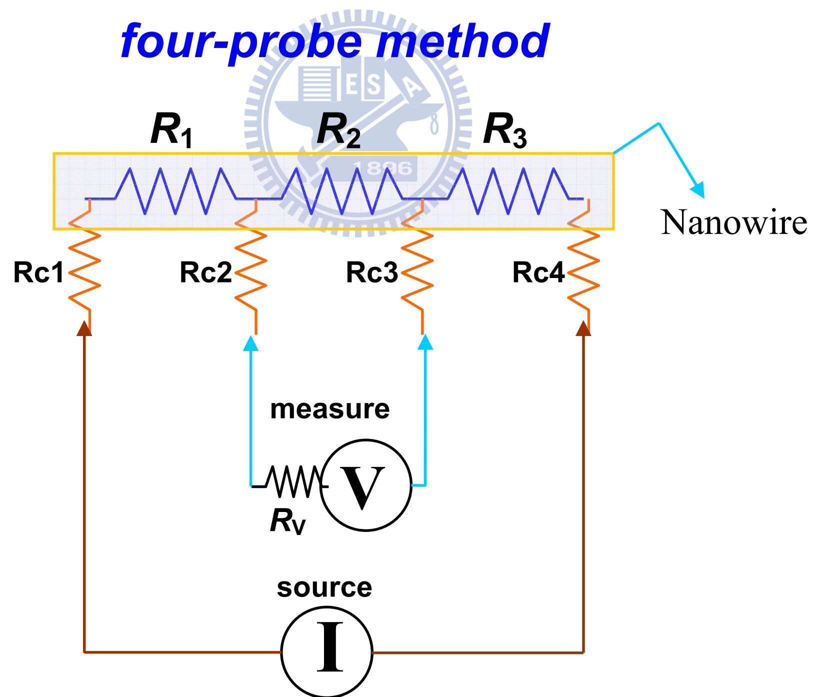

Figure 2.3: The the equivalent circuits for two- and four- probe measurement. The R_i, i=1, 2, 3, are the NW resistances in different segments. The R_{ci}, i=1, 2, 3, 4, are the contact resistances within different interfaces between NW and metal electrodes.

ways depending on the magnitude of NW resistances, R_i, and contact resistances, R_{ci}, in the NW device. First way employs the AC resistance bridge (Linear Research LR-700) to get low-noise resistance signal. The embedded 16 Hz AC Lock-Balance circuit allows for the voltage resolution down to sub-nanovolt region. This technique outperforms DC bridges by up to two orders of magnitude in the voltage sensitivity. However, because the input impedance of LR-700 is smaller (The maximum resistance range is 2 Mega-Ω.) and we still need to keep the requirement ($R_v >> R_i$, and R_{ci}) for four-probe measurement, this method often performs on the NW devices with smaller R_i, and R_{ci} (e.g. ITO NW devices). Sometimes, although the requirement for four-probe measurement is held, LR-700 shows some error messages about the phase mismatch, which may originate from the capacitance effect of sub-micron contacts. Thus the second way is needed.

The second way is the DC method, in which a DC current source and a DC voltage meter with high input impedance are used to sweep the *I-V* curves and the resistance is extracted from the linear region around zero-bias. The current source could be Keithley K-220, K-6430, or K-2635. The voltage meter could be Keithley K-617, K-6430, or K-2635, where K-6430 and K-2635 are the multi-functional SourceMeters. All the voltage meters mentioned above possess huge input impedance (~ Tera-Ω, i.e. 10^{12} Ω), hence this method could be suitable for the NW devices with larger R_i, and R_{ci} (e.g. undoped ZnO NW devices).

The NW devices are placed on a sample holder as shown in the Figure 2.2 which is situated inside a dark vacuum chamber or vacuum can. The vacuum chamber is mounted on a standard ^{4}He cryostat or an Oxford Heliox ^{3}He fridge. These two kinds of cryostats are designed for controlling temperatures in the different temperature ranges. The ^{4}He cryostat is operated in the range between 325 K and 1.3 K. The ^{3}He cryostat is operated in the range between 100 K and 0.25 K, and a Ti-Nb superconducting magnet with extreme field up to 4 Tesla is incorporated with the ^{3}He cryostat for the measurement of magnetoresistance, Hall effect, and so on.

With either AC or DC methods for the four-probe measurement, we always make sure that the resistance at a given temperature is determined from the regime around the zero bias voltage, where the $I-V$ curve was essentially *linear*. The Figure 2.4 shows an example of our measurement process which is controlled by a LabVIEW program. There are two temperature steps, named T-step1 and T-step2, which correspond to the measurements of resistances and large-range I-V curves, respectively. Typically, the T-step1 set to 1 K and the T-step2 set to 10 K. In the right window of Figure 2.4, we monitor the shape of I-V curves every 10 K to know how wide the bias range corresponds to the linear region of the I-V curve. Therefore we

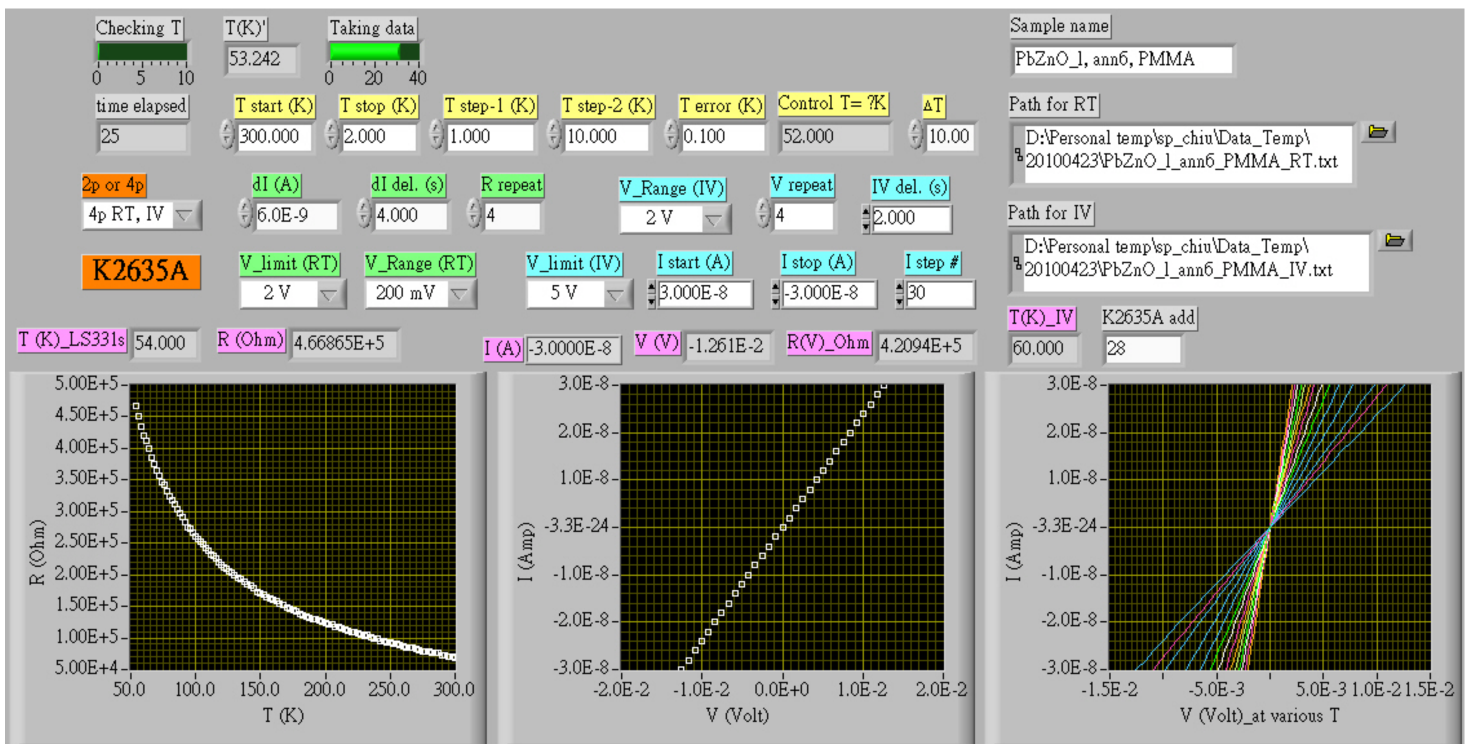

Figure 2.4: The measurement process is controlled by a LabVIEW program which is functionalized to control the temperatures and measure the resistances and *I*-*V* curves at stable temperatures.

can perform a short-range *I-V* measurement within the linear region to extract the resistance every 1 K. The resulting resistances are showed in the left window of the Figure 2.4. The electron heating effect may be significant at lowest temperatures. It happens when the thermal relaxation rate between the substrate and the sample holder is not fast enough to relax the heat, I^2R_s, generated by the bias current, I, where R_s is the sample resistance. Therefore, there is an extra temperature difference between the substrate and the sample holder. To eliminate this extra temperature difference, we should tune a suitable low bias current, otherwise we'll find that at a fixed temperature, the resistance is varied as bias current changing.

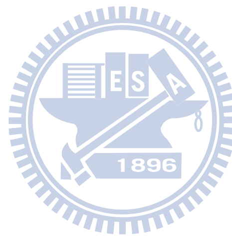

Chapter 3

Electrical transport in ITO nanowires

3.1 Introduction

In recent years, the science and technology of metal and semiconductor nanowires (NWs) have been very extensively explored [2][4]. In addition to the material and application aspects, the fundamental physical properties of NWs have been investigated. The optical, magnetic and mechanical properties of NWs have drawn much theoretical and experimental attention. On the other hand, the electrical-transport properties of *individual* NWs have not been much studied. In fact, most electrical measurements on single NWs reported to date have mainly focused on either a two-probe configuration [13][15] or (in the case of semiconductor NWs) a field-effect-transistor configuration [16][17]. Electrical-transport results obtained from *four-probe* measurements on single NWs over a wide range of temperature are still limited [18][21]. This lacking of four-probe results is probably partly due to the difficulties in fabricating good ohmic electronic contacts to individual NWs and partly due to the difficulties in handling and detecting nanoscale samples down to liquid-helium temperatures.

Among the numerous semiconducting and metallic NWs, Sn-doped In_2O_3 (indium tin oxide (ITO)) NWs have recently been studied [22][26]. Several groups have reported the growth behaviors and physical properties of ITO NWs. The interest in these nanoscale structures arises from the fact that the parent ITO material is a transparent conducting oxide. Moreover, the charge carriers in this material are established to be essentially free-electron-like. That is, the charge carriers behave like an ideal free electron gas with an effective mass of $m^* \approx 0.4\, m$ and a Fermi energy of $E_F \sim 1$ eV (whose value depends on the carrier concentration, n), where m is the free electron mass. The thermoelectric power (Seebeck coefficient) reveals a linear behavior from 300 K all the way down to liquid-helium temperatures, while the temperature behavior of resistivity is well described by the Bloch–Grüneisen law at not too low temperatures [27][29]. The carrier concentration in highly conductive ITO materials usually falls in the range from 10^{20} to 10^{21} cm^{-3} [30] and the room-temperature resistivity can be as low as ~100 $\mu\Omega$ cm, if properly prepared [31].

In view of the nanoelectronic and optoelectronic applications, it is very useful to clarify whether the ITO NWs still preserve the desirable electrical properties, such as metallic conduction and low resistivities. Thus far, there have been only a few reports on

charge-transport measurements of single ITO NWs [26][31][32]. Besides, those measurements were performed on a two-probe configuration where the contributions from contact resistances and lithographic electrode resistances could not be excluded[1]. In this work, we present the first four-probe measurements on several single ITO NWs from 300 down to 1.5 K. These results thus represent the *intrinsic* electrical properties of individual single-crystalline ITO NWs.

3.2 Experimental method

ITO NWs were synthesized on 0.5 × 0.5 cm^2 Si substrates by the standard thermal evaporation method, as has been described previously [33]. Gold nanoparticles with a diameter of ~20 nm were first dispersed on the Si substrates. Mixtures of indium (99.999% purity, Aldrich) and tin (99.9% purity, Merck) powders with a weight ratio of In:Sn = 9:1 were placed in the middle of a horizontal quartz tube. The spectrographic analysis as provided by the supplier indicated that the tin powders contained trace amounts of nonmagnetic (Bi: ≤ 0.01 at.%, Cu: ≤ 0.01 at.%, Pb: ≤ 0.05 at.%, Sb: ≤ 0.02 at.%) and magnetic (Fe: ≤ 0.02 at.%) impurities. A series of several Si substrates were placed near to the powders and were situated on the downstream side of the gas flow. An argon gas was input from one end of the quartz tube and the pumping speed at the other (downstream) end was adjusted to maintain an atmosphere of 50 Pa in the tube. The source powders were heated to 920 ℃ for 3 h, while the nearby Si substrate temperatures varied from ~900 to ~850 ℃, depending on their distance to the source powders.

X-ray diffraction (XRD, MAC Science MXP-18) and high-resolution transmission electron microscopy (TEM, JEOL JEM-2010FX) studies indicated that the NWs were single crystalline, possessing a cubic bixbyite structure, and grew along the [100] direction. Figures 3.1(a) and (b) show a low magnification TEM image and an HRTEM image, respectively, for a single ITONW. The morphology of the NWs was examined by field emission scanning electron microscopy (SEM, JEOL JSM-6330F). We found that the diameters, *d*, of the as-grown NWs were sensitive to the substrate temperature, and thus their sizes distributed widely among the substrates. The energy-dispersive x-ray spectroscopy (EDS, JOEL JEM-2010FX) and the inductively coupled plasma atomic emission spectrometry (ICP-OES, Perkin-Elmer Optima-3000DV) were utilized to determine the chemical compositions of the

[1] In the case of metal NWs with good contacts, the two lithographic (e.g. Ti/Au or Cr/Au) electrode resistances may be of the same order of magnitude as the two contact resistances.

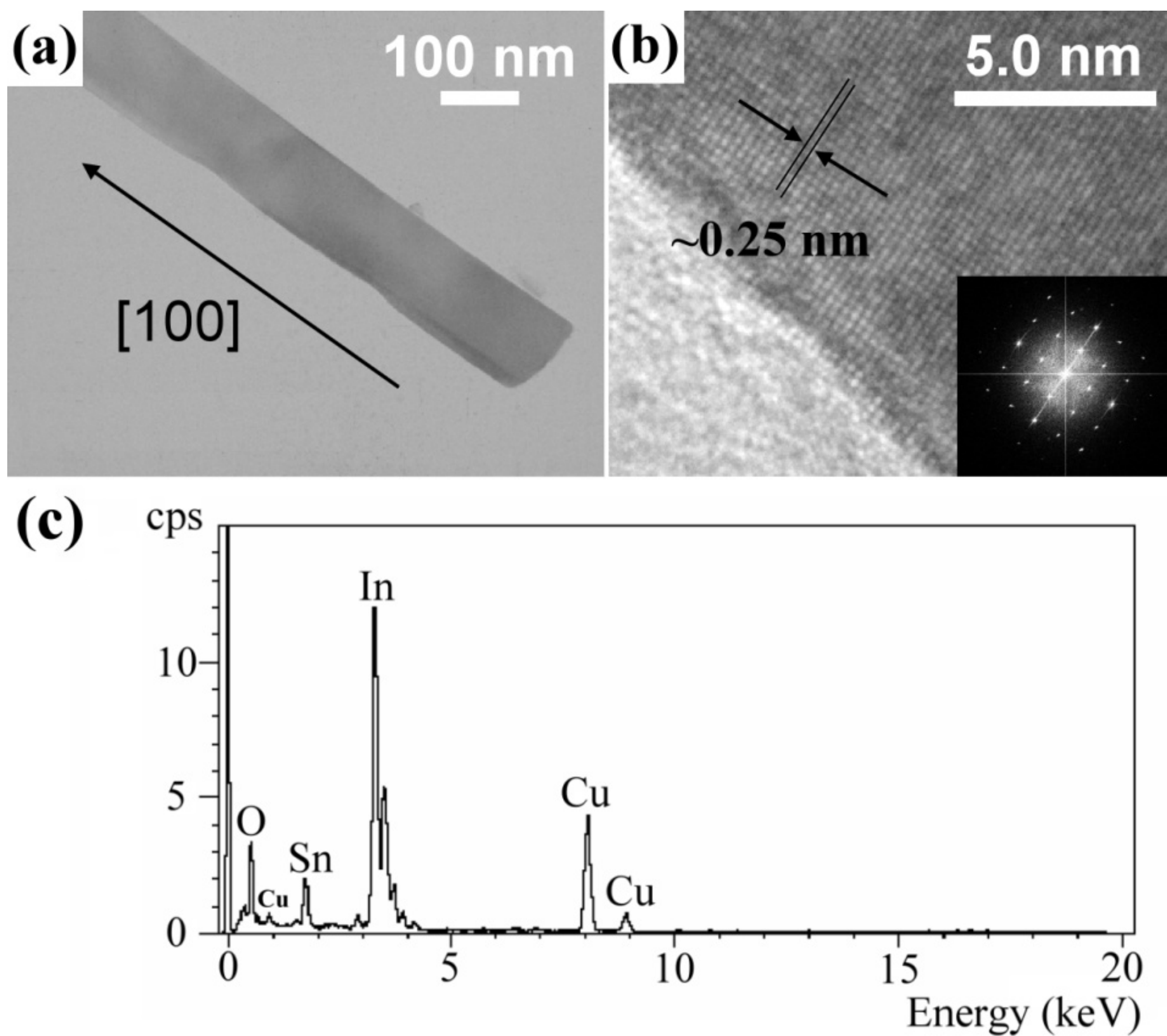

Figure 3.1: (a) A low magnification TEM image for a single ITO NW. (b) A high-resolution TEM image for the same ITO NW. The inset shows the corresponding selected-area electron diffraction pattern. (c) EDS spectrum for the ITO NWs grown on substrate A. The Cu peaks are due to the TEM Cu grids.

Table 3.1: Relevant parameters for four-probe individual ITO NW devices. Ts is the Si substrate temperature during the NW growth process. The character in parentheses following the temperature indicates the substrate name, A or B. Sn/In is the weight ratio of tin to indium. d is the NW diameter. ρ_{min} is the lowest measured resistivity of each sample. T_{min} is the temperature where ρ_{min} occurred.

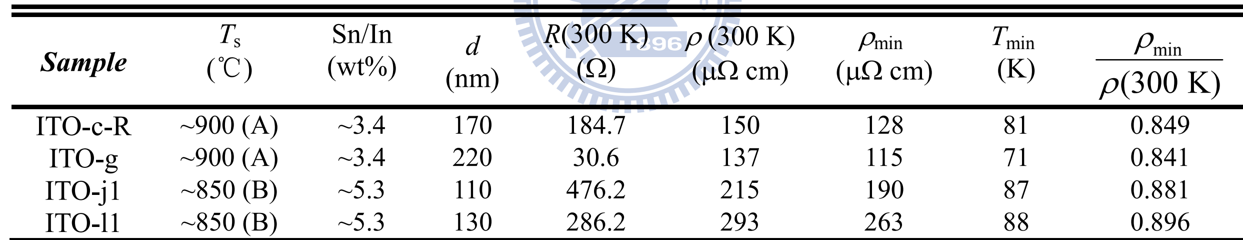

Sample	T_s (℃)	Sn/In (wt%)	d (nm)	R(300 K) (Ω)	ρ (300 K) (μΩ cm)	ρ_{min} (μΩ cm)	T_{min} (K)	$\frac{\rho_{min}}{\rho(300\ K)}$
ITO-c-R	~900 (A)	~3.4	170	184.7	150	128	81	0.849
ITO-g	~900 (A)	~3.4	220	30.6	137	115	71	0.841
ITO-j1	~850 (B)	~5.3	110	476.2	215	190	87	0.881
ITO-l1	~850 (B)	~5.3	130	286.2	293	263	88	0.896

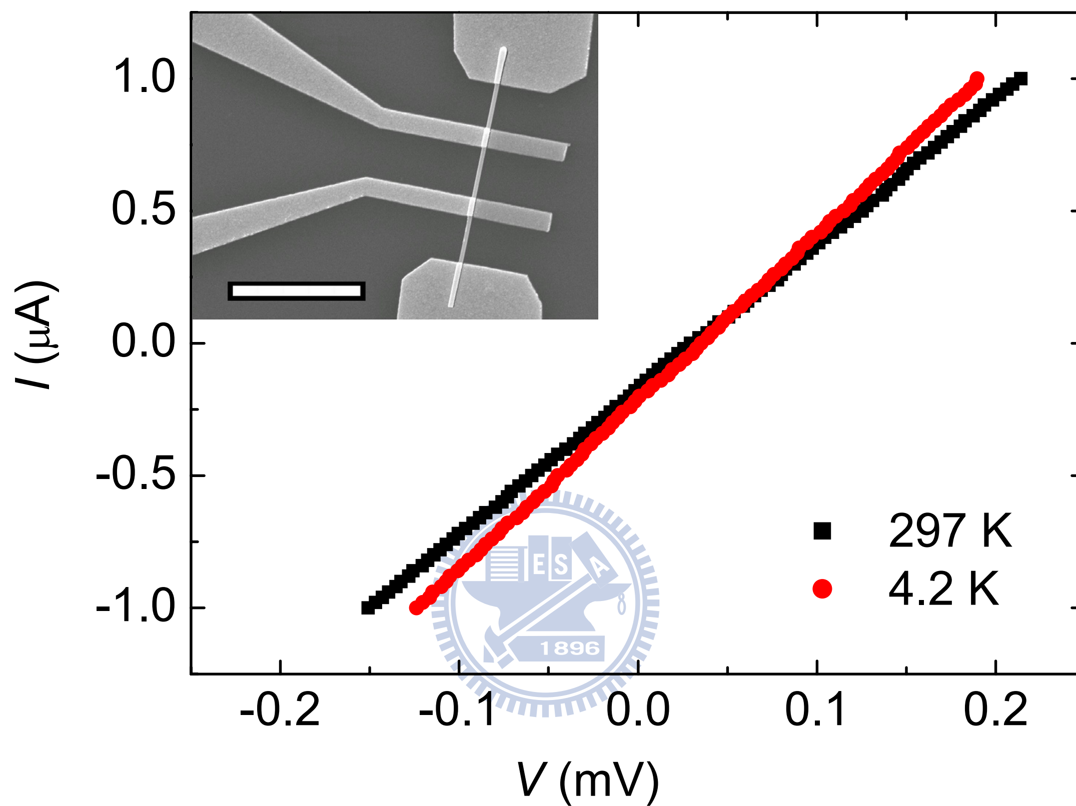

Figure 3.2: Current–voltage curves for the individual ITO-c-R NW at 297 and 4.2 K, as indicated. Notice that the *I*–*V* curves are linear. The inset shows an SEM image for this four-probe ITO NW device fabricated with electron-beam lithography. The scale bar is 5 μm.

NWs. The former method determined the chemical compositions in a single NW, because the TEM electron beam was focused to a size of ≈3.7 nm, which was much smaller than the typical diameter of our NWs. The latter method determined the average chemical compositions by introducing a collection of many NWs into a chamber where the NWs were dissolved and ionized in an argon plasma. The compositions we obtained from these two complementary methods were consistent to within about 5%. We observed that the Sn content increased notably with decreasing Si substrate temperature. In the present study, we chose two substrates (referred to as A and B) with as-grown NWs for the fabrication of four-probe individual NW devices. The substrate temperature during the NW growth process was approximately 900 ℃ (850 ℃) for substrate A (B). The weight ratio of Sn to In for the NWs was ~3.4% for substrate A and ~5.3% for substrate B. (For comparison, for those NWs grown on another Si substrate which was placed in between substrates A and B and having a substrate temperature of ~880 ◦C during the growth process, we obtained an Sn/In weight ratio of ~4.4%.) Figure 3.1(c) shows the EDS spectrum of the NWs grown on substrate A. It is clearly seen that Sn was effectively incorporated into the ITO NWs. Table 3.1 lists the values for the relevant parameters for the four NWs whose overall temperature behaviors of resistivity are studied in this work.

To fabricate four-probe individual NW devices for electrical-transport measurements, we first made micron-sized Ti/Au (10/60 nm) metal pads and coordinate marks by utilizing the standard photolithography and lift-off technique on Si substrates capped with a 400 nm thick SiO2 layer. ITO NWs were then dispersed on the SiO2/Si substrates. Individual NWs with diameters of ~100–200 nm were identified and electrically connected to the pre-patterned micron-sized Ti/Au metal pads by using the standard electron-beam lithography and lift-off technique. In order to make good ohmic contacts to the NWs, an O2 plasma was employed to clean the substrates before the Ti/Au (30/120 nm) electrodes contacting the NWs were deposited by the thermal evaporation method. The electrodes were typically a few hundreds of nanometers wide. An SEM image for a representative four-probe single ITO NW device is shown in the inset to figure 3.2.

The single NW devices were placed on a sample holder which was situated inside a dark vacuum can. The vacuum can was mounted on a standard 4He cryostat for electrical resistance measurements from 300 down to 1.5 K. The fourprobe current–voltage ($I - V$) characteristics were first checked by utilizing a Keithley K-6430 source meter as a current source and a K-182 nanovoltmeter. The $I - V$ curves were linear even up to our maximum applied current of 1 μA. Figure 3.2 shows two representative $I - V$ curves for the ITOc- R NW

at 297 and 4.2 K, respectively. An AC resistance bridge (Linear Research LR-700) was then employed for the measurement of temperature-dependent resistance, $R(T)$. It should be noted that, for all the results reported in this work, the values of $R(T)$ were determined with sufficiently small bias currents (typically,~30 nA) where the I –V characteristics were certainly linear and the electron heating effects were negligible down to our lowest measurement temperatures.

Inspection of table 3.1 indicates that the four-probe values of $\rho(300\ K)$ in the NWs taken from substrates A and B differ by roughly a factor of two. This amount of difference in resistivity should be considered satisfactory. The variation in resistivity from NW to NW may be accounted for by the variation of the Sn/In weight ratio as well as by the uncertainties in the individual NW dimensions which were needed to calculate the resistivity from the measured resistance. In fact, during the course of this study, we have also carried out *in situ* two-probe TEM–scanning tunneling microscopy (STM) measurements [34] on 17 single ITO NWs at room temperature and obtained an average resistivity of $\rho(300\ K) \approx 250 \pm 100\ \mu\Omega$ cm. We point out that this resistivity value is several orders of magnitude lower than that in the ITO NWs grown by the electrospinning process [26]. For comparison, we also notice that recent experimental studies have reported that the resistivities of ITO NWs grown under nominally similar conditions could vary widely, from ~100 $\mu\Omega$ cm to values higher than several thousands of $\mu\Omega$ cm [23][31]. Then, the overall electrical quality of our as-grown ITO NWs should be considered as being relatively uniform and fairly good, i.e. our resistivity values are approximately similar (to within a factor of ~2–3) and comparatively low.

3.3 Results and discussion

Perhaps due to the experimental difficulties in fabricating lithographic contacting electrodes, the electrical resistances of single metal and semiconductor NWs reported in the literature were often measured by employing the two-probe method. However, it is well known that only the four-probe configuration can give the intrinsic resistances of the NWs under study [33]. Figure 3.3 shows the two-probe result and the four-probe result for the ITO-c-R NW whose SEM image was depicted in figure 3.2. Here $R_{2p}(T)$ denotes the resistance measured by employing the inner two electrodes as both the current and the voltage leads, while $R_{4p}(T)$ denotes the resistance measured by employing the outer two electrodes as the current leads and the inner two electrodes as the voltage leads. Obviously, the measured two-probe result includes not only the NW resistance but also the two contact resistances as

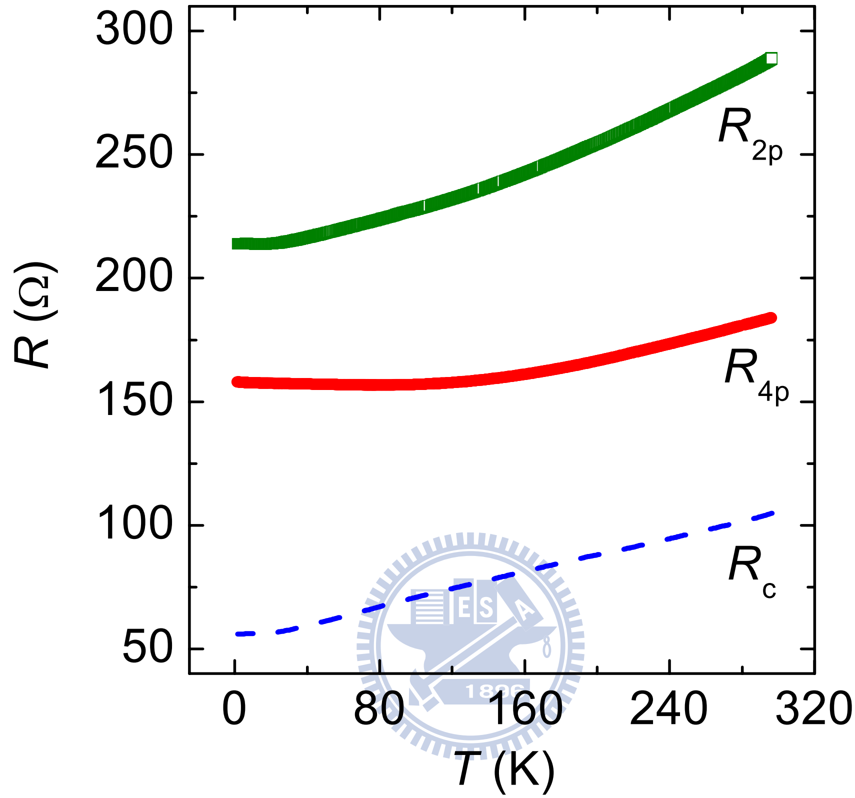

Figure 3.3: Measured two-probe, R_{2p}, and four-probe, R_{4p}, resistances as a function of temperature for the individual ITO-c-R NW devices, as indicated. The two-probe data were measured with the two inner electrodes as depicted in the inset to figure 3.2. The dashed line indicates the total contact resistance plus the lithographic electrode resistance, as given by $R_c(T) = R_{2p}(T) - R_{4p}(T)$.

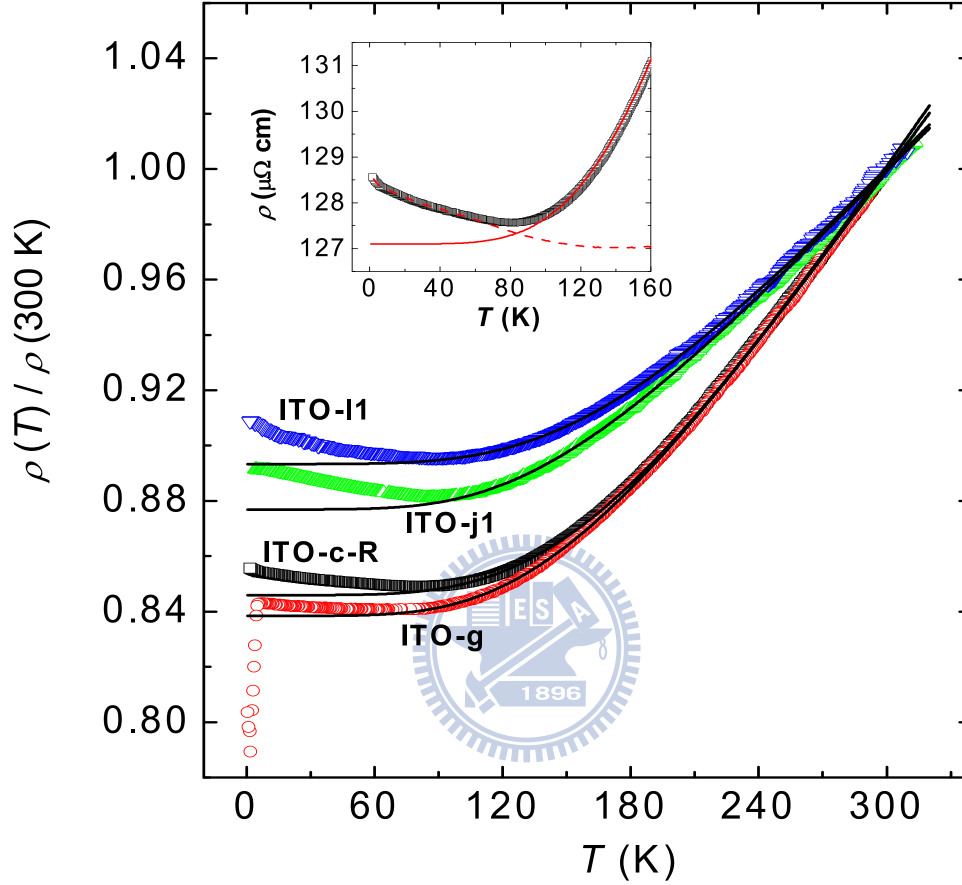

Figure 3.4: Normalized resistivities, $\rho(T)/\rho(300\ \mathrm{K})$, as a function of temperature for four individual ITO NWs, as indicated. The symbols are the experimental data and the solid curves are the theoretical predictions of equation (3.1). The inset shows the measured resistivity as described by the sum of the Bloch–Grüneisen law (solid curve) and a disorder-induced correction to ρ_0 (dashed curve) for the ITO-c-R NW.

well as the two lithographic Ti/Au electrode resistances. As a consequence, $R_{2p} > R_{4p}$ for all measurement temperatures. Moreover, the temperature behaviors of R_{2p} and R_{4p} are distinct. Thus, one should always be very cautious about drawing any conclusion from the results and analyses based on two-probe electrical-transport measurements[2].

The sum of the two contact resistances and the two lithographic electrode resistances can be quantitatively determined and is simply given by $R_c(T) \equiv R_{2p}(T) - R_{4p}(T)$ (the dashed line in figure 3.3). The smallness of the magnitude (<100 Ω) together with the metallic-like temperature behavior of R_c indicates that the two contacts are fairly good and ohmic. This observation demonstrates that low-resistance ohmic contacts can be readily achieved in nanoelectronic devices utilizing ITO NWs as interconnects. In the following, we shall concentrate on the four-probe results so as to address the intrinsic electrical resistivities of individual ITO NWs.

Figure 3.4 shows the four-probe results of the normalized resistivities, $\rho(T)/\rho(300\ \text{K})$, as a function of temperature for four individual ITO NWs. We notice that the ITO-l1 and ITO-j1 NWs are more resistive than the ITO-c-R and ITOg NWs, and hence the resistivity ratios $\rho(1.5\ \text{K})/\rho(300\ \text{K})$ are larger in the former NWs than in the latter NWs. (In the case of the ITO-g NW, we had compared the ratio $\rho(7\ \text{K})/\rho(300\ \text{K})$.) Nevertheless, in all four NWs, the resistivity ratios are close to unity, implying that the NWs must all contain large amounts of defects. That is, the residual resistivity is relatively high, as compared with the temperature dependent phonon contribution. In the ITO-g NW, an unusual resistivity drop is seen at 5 K, which may signify a possible onset of superconductivity in this particular, i.e. our least resistive, NW [35][36] (see below). Inspection of figure 3.4 suggests that our as-grown ITO NWs are metallic, namely their resistivities decrease with reducing temperature as the samples are cooled from 300 K down. Such temperature behavior of resistivity can be explained by the Bloch–Grüneisen law [37]:

$$\rho = \rho_0 + \beta_{BG} T \left(\frac{T}{\theta_D}\right)^4 \int_0^{\frac{\theta_D}{T}} \frac{x^5}{(e^x - 1)(1 - e^{-x})} dx \tag{3.1}$$

where ρ_0 is a residual resistivity, β is an electron–phonon coupling constant and θ_D is the Debye temperature. Our experimental data for all NWs are least-squares fitted to the

[2] A comparison of two-probe and four-probe electrical-transport results for semiconductor ZnO NWs has recently been discussed in [21]. Discussions of the temperature behaviors of electronic contact resistances to metal NWs have been given in [19] and [33].

Table 3.2: Least-squares fitted (ρ_0, θ_D and β) and evaluated (l and $k_F l$) values of relevant parameters for individual ITO NWs.

Sample	ρ_{min} ($\mu\Omega$ cm)	θ_D (K)	β ($\mu\Omega$ cm K^{-1})	l (nm)	$k_F l$
ITO-c-R	127	1047	0.571	10	30
ITO-g	115	958	0.492	11	33
ITO-j1	189	927	0.571	6.9	21
ITO-l1	262	1086	0.802	5.0	15

predictions of equation (3.1) (the solid curves) and the values of the fitted parameters (ρ_0, β and θ_D) are listed in table 3.2. Inspection of figure 3.4 clearly indicates that the experimental results can be well described by equation (1) at high temperatures of $T > T_{min}$, where T_{min} is defined as the temperature where the measured ρ assumes the minimum value, ρ_{min}. It is important to notice that our fitted values of β and θ_D are in good agreement with the corresponding values

Recently obtained in polycrystalline ITO films [27][29]. For the ITO materials with a room-temperature resistivity of ~200 $\mu\Omega$ cm, the Fermi energy is ≈0.9 eV [27]. Therefore, an estimate using the free electron model gives a value of the Fermi wavenumber $k_F \approx 3 \times 10^9$ m^{-1}. From the Drude resistivity $1/\rho = (ne^2\tau)/m^* = (k_F^2 e^2 l)/(3\pi^2\hbar)$, one obtains a value of the product $\rho l \approx 1.3 \times 10^{-14}$ Ω m^2, where e is the electron charge, $\hbar$ is Planck's constant divided by 2π and τ (l) is the electron elastic mean free time (path). Then, $l \approx 6.5$ nm and $k_F l \approx 20$. Notice that this value of l is much smaller than the diameter d of our NWs. Therefore, the NWs are threedimensional with regard to the Bloch–Grüneisen transport. At low temperatures of $T < T_{min}$, figure 3.4 indicates that the measured $\rho(T) > \rho_{min}$ and it slightly increases with reducing temperature. A plot of the variation of the normalized resistivity, $\rho(T)/\rho_{min}$, with $\sqrt{T}$ in figure 3.5 reveals that the low-temperature resistivity rise scales approximately with the square root of temperature in every NW. Except for the least resistive ITO-g NW, the amount of the resistivity rise is approximately 1%–1.5%. In particular, the amount of the resistivity rise basically increases with increasing ρmin, suggesting that this $\sqrt{T}$ behavior must be closely associated with some sort of disorder effect. In other words, the disorder effect induces a temperature-dependent correction to the measured resistivity at low temperatures. The presence of high levels of disorder in our NWs is already shown from the fact that the resistivity ratios $\rho_{min}/\rho(300\ K)$ are close to unity in all of our NWs, see figure 3.4 and table 3.1. The nature of the randomness most likely reflects the existence of a great number of point defects in our as-grown ITO NWs, since our HRTEM studies indicated the absence of any linear and planar defects in the samples (while point defects could not be detected from the HRTEM study)[3]. In this regard, the four-probe electrical-transport measurements can be used as a very powerful probe for the microscopic quality of the atomic structure in a given NW.

[3] A similar result has recently been obtained in metallic single-crystalline RuO_2 NWs [38]. In that case, the HRTEM study also revealed a high-quality atomic structure, but the electron elastic mean free path l inferred from the four-probe electrical-transport measurements was only of the order of ~1 nm. Such a short mean free path implies strong scattering between conduction electrons and point defects.

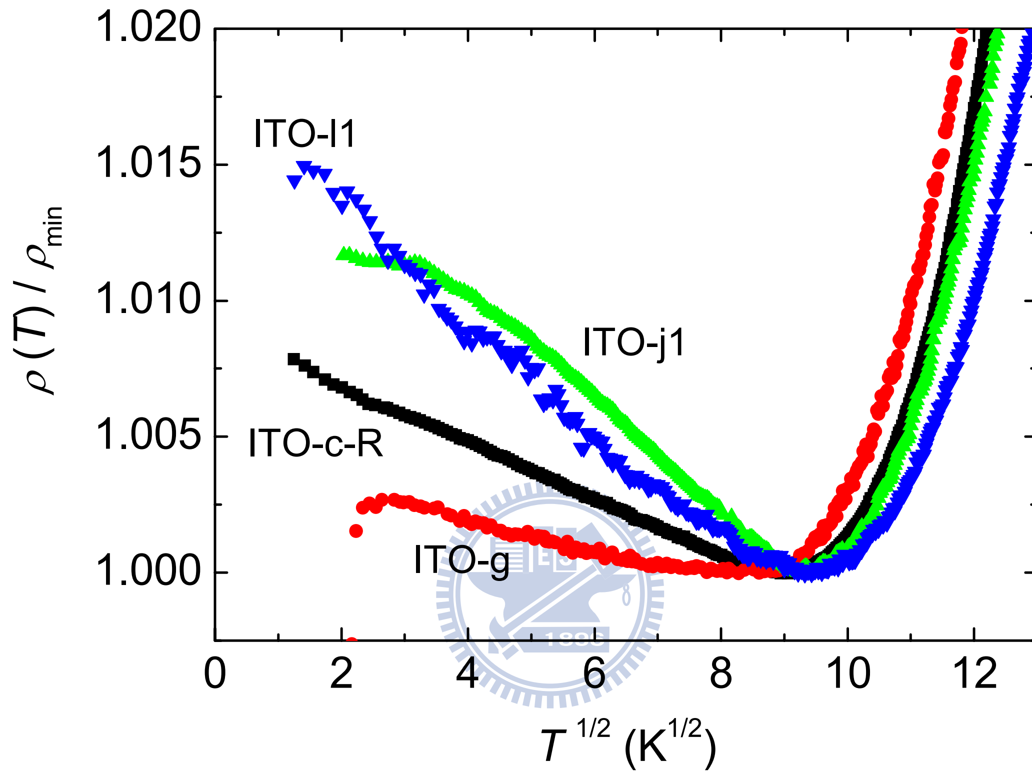

Figure 3.5: Normalized resistivities, $\rho(T)/\rho_{\min}$, as a function of temperature for four individual ITO NWs, as indicated. Notice that the resistivity rises scale approximately with $\sqrt{T}$. For the ITO-j1 NW, there is a tendency to saturation below about 10 K, while for the ITO-g NW, there is an abrupt resistivity drop at 5 K.

In the presence of *static* defects in a normal metal, one may usually expect the quantum-interference weak localization and electron–electron interaction effects to occur at low temperatures [39][40]. These two effects lead to small, but explicit, temperature-dependent corrections to ρ_0 (or $\rho_{\min}$). However, with the parameters pertinent to our samples (e.g. $k_F l \approx 20$, $D \approx 19$ cm2 s^{-1} and $\rho \approx 200$ $\mu\Omega$ cm), we expect the two effects to cause a resistivity rise less than a tenth of a per cent down to 1.5 K. In other words, the resistivity rises that we observed in figure 3.5 (especially those in the ITO-j1 and ITO-l1 NWs) are more than one order of magnitude, as would be expected from the corrections due to the three-dimensional weak-localization and electron–electron interaction effects. Therefore, the two effects can only minutely be responsible for the observed resistivity rises[4].

Another kind of disorder effect that can lead to a low-temperature correction to resistivity originates from the scattering of electrons off *dynamic* structural defects. The dynamic defects can often be modeled as two-level tunneling systems, and the electron–dynamic defect scattering can be described in terms of the *nonmagnetic* two-channel Kondo effect. In this case, the resistivity correction is given by [41][42]

$$\rho_{2CK}(T) = \frac{3n_i}{4\pi\hbar[eN(0)v_F]^2}\left[1 - 4\lambda\sqrt{\pi T}\right] \tag{3.2}$$

where n_i is the dynamic defect density, $N(0)$ is the electronic density of states per spin per channel at the Fermi level, v_F is the Fermi velocity and $\lambda \approx (T_{2CK})^{-1/2}$ is the coupling constant (T_{2CK} being the characteristic two-channel Kondo energy scale). Such a novel resistivity correction $\rho_{2CK} \propto \sqrt{T}$ has recently been realized in Co/(Cr/Ag)/Co trilayer systems [42] and perhaps also in a ThAsSe single crystal [43].

In the case of highly conductive ITO materials, it is known that the charge carriers can be very well described by a free electron- like approximation [44][45], as discussed in section 1. Therefore, the electronic density of states should take the form $N(0) \propto (m^*)^{3/2}(E_F)^{1/2}$ [46]. Since the effective electron mass $m^* \approx 0.4\, m$ and the Fermi energy $E_F < 1$ eV in ITO [27][29], the value of $N(0)$ is approximately one order of magnitude smaller than that in a typical metal

---

[4] According to [32] and our preliminary measurements, the electron dephasing length $L_\varphi(T)$ in ITO NWs is shorter than a few tens of nanometers. Therefore, our NWs are three-dimensional (i.e. $d > L_\varphi$) with respect to the weak-localization effect. (Notice, however, that the L_φ was measured in a two-probe manner in [32]. Four-probe measurements should give a more accurate value.) Taking D = 19 cm^2 s^{-1}, the electron thermal diffusion length $L_T = \sqrt{D\hbar/k_B T} \approx (120/\sqrt{T})$ nm [39]. Thus, our NWs are also three-dimensional with regard to the electron–electron interaction effect over our measurement temperature range.

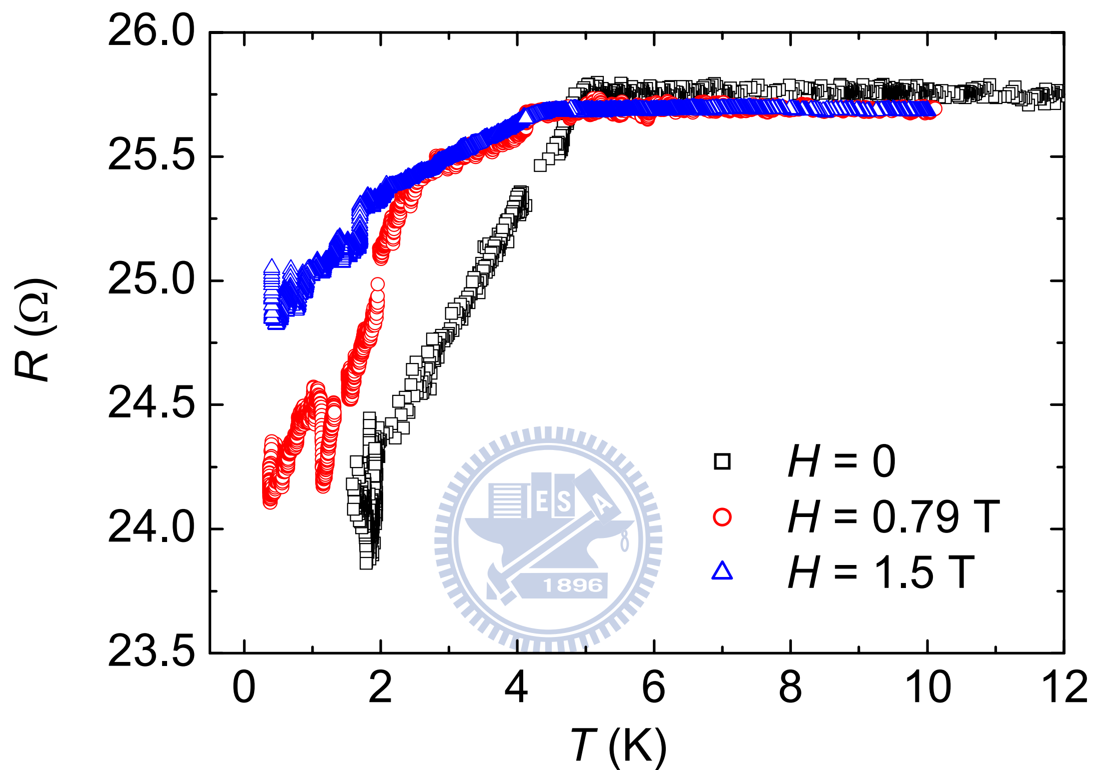

Figure 3.6: Resistance as a function of temperature for the ITO-g NW in zero magnetic field and in two magnetic fields of 0.79 and 1.5 T, as indicated. The magnetic fields were applied perpendicular to the direction of the current flow.

[36][45]. Therefore, the resistivity correction ρ_{2CK}, which scales inversely with the square of $N(0)$, can be significantly larger in the ITO materials than in normal metals. (The value of $v_F = \hbar k_F / m^*$ in ITO is not much different from that in a typical metal.) Moreover, as discussed, the as-grown ITO NWs usually contain numerous point defects, and hence the dynamic defect concentration n_i in the samples can be relatively high[5]. Consequently, it is plausible to expect the ρ_{2CK} contribution to be important in these NWs. Thus, the $\sqrt{T}$ behavior observed in figure 3.5 may be reasonably ascribed to the novel nonmagnetic two-channel Kondo effect. Further studies in this direction can help to gain an insight into the microscopic properties and dynamics of the point defects in these NWs.

In the $T \to 0$ limit one may expect a breakdown of the scaling $\rho_{2CK} \propto \sqrt{T}$ due to interaction between two-level tunneling systems and a transition to the usual Fermi-liquid behavior, $\rho \propto T^2$, should occur [42]. This might be the case found in our ITO-j1 NW below about 10 K. This issue deserves further studies.

It is worth noting that the low-temperature resistivity rises which we observed in figure 3.5 cannot be ascribed to the standard (one-channel) Kondo effect originating from dilute magnetic impurities [47]. Our reasons are given as follows. (1) To the best of our knowledge, there have been no reports for the ITO materials being a magnetic Kondo system in the literature. (2) The resistivity rises in our NWs obey a $\sqrt{T}$ law, rather than the distinct $\ln T$ law as would be expected for the paradigmatic Kondo effect [47]. (3) Moreover, if our resistivity rises were to be attributed to the magnetic Kondo effect, a Kondo temperature of a few tens of kelvin would be required (recall that our $T_{min} \approx$ 70–90 K), which seems to be unrealistically high. (4) Finally, our magnetoresistance measurements indicated an extremely small magnetoresistance (see below), implying that magnetic impurities do not play a notable role in our samples. Therefore, we conclude that the standard magnetic (one-channel) Kondo effect cannot be responsible for the low-temperature resistivity rises which we found in figure 3.5.

Figure 3.6 shows the resistance as a function of temperature in zero magnetic field and in two perpendicular magnetic fields, as indicated, for the ITO-g NW below 12 K. (This part of the measurements was carried out with an Oxford Heliox ^{3}He fridge equipped with a 2 T superconducting magnet.) The magnetic fields were applied perpendicular to the direction of the current flow. Clearly, there is a resistance drop starting at 5 K in zero magnetic field. The

[5] By taking a value of $N(0) \approx 10^{45}$–10^{46} states J^{-1} m^{-3}, a dynamic defect concentration of $n_i \sim 10^{23}$–10^{25} m^{-3} will give rise to a relative resistivity rise of $\rho_{2CK}/\rho_{min} \sim 0.015$.

resistance is partly restored in the presence of our applied magnetic fields, signifying that this resistance drop may be related to a possible onset of superconductivity in this particular, i.e. our least disordered, NW. Unfortunately, this superconducting transition is very broad and is not complete even down to our lowest measurement temperature of 0.3 K. Provided that this scenario is accepted, one plausible explanation would be that a full transition to a superconducting state has been hindered by the presence of a large amount of point defects in our as-grown ITO NWs, as discussed. Indeed, we notice that signatures of inherent superconductivity in ITO materials have previously been reported by several authors [35][36]]. Nevertheless, the situation is more complex in a disordered system, as the disorder effect can significantly suppress the superconducting transition. For instance, in a 87 nm thick ITO film, only a small (<1%) resistance drop was found between 3.5 and 1.5 K, which was understood in terms of a competition between electron localization and superconductivity [35]. In our case, the zero-field resistance dropped by ~5% when the temperature was reduced from 5 to 2 K. Our resistance drop is larger likely because our ITO-g NW has a lower ρ(300 K) value of 137 $\mu\Omega$ cm, as compared with that (590 $\mu\Omega$ cm) in the 87 nm think ITO film mentioned above. Once the temperature is raised to be above 5 K, the magnetic field effect on resistance becomes negligibly small. Between 5 and 10 K, we found a negative magnetoresistance of $[\rho(B = 1\text{ T}) - \rho(0)]/\rho(0) \approx -0.001$ (not shown). This minute magnetoresistance suggests that magnetic impurities barely played a significant role in our NWs. High-quality single-crystalline NW samples with low resistivities (for example, ρ(300 K) ~ 100 $\mu\Omega$ cm) will be very useful for addressing the superconductivity problem in ITO materials. The various behaviors that we observed in figures 3.5 and 3.6 reflect the richness and subtlety (which could be associated with the dynamic point defects) of the low-temperature electrical properties of ITO NWs. This issue deserves further theoretical and experimental investigations.

3.4 Summary

We have measured the intrinsic temperature behavior of resistivity for individual ITO NWs from 300 down to 1.5 K, employing the four-probe measurement configuration. Low resistance ohmic Ti/Au electrodes were fabricated by using the electron-beam lithography technique. The overall temperature behavior of resistivity suggests that the as-grown ITO NWs are metallic, but disordered. The metallic property is well described by the Bloch–Grüneisen law. However, electron scattering off dynamic point defects causes an

additional temperature-dependent correction to the resistivity at low temperatures. The dynamic defects are likely associated with the numerous point defects which inevitably exist in as-grown ITO NWs. This work demonstrates that the four-probe electrical-transport method can serve as a powerful probe for the microscopic quality of the atomic structure in a given nanoscale device.

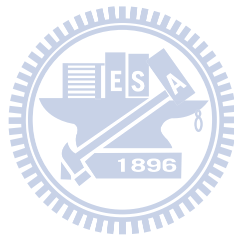

Chapter 4

Electrical transport in natively doped ZnO nanowires

4.1 Introduction

Owing to the potential applications in the emerging nanoelectronics and optoelectronics, zinc oxide (ZnO) has recently attracted intense theoretical and experimental attention [48][50]. ZnO is a wide band gap semiconductor with a direct gap of 3.4 eV at room temperature, and is a native n-type material. The n-type characteristics of electronic conduction in nominally undoped ZnO materials are believed to originate from the native defects such as structural imperfections and unintentional impurities. However, the microscopic origins for these native defects (e.g., Zn interstitials, oxygen vacancies, etc), and their corresponding impurity levels, are still under much debate [51][55]. Generally speaking, it is known that the dopant levels are sensitive to the methods of sample preparation and can roughly be categorized into shallow levels and deep levels. The shallow levels lie approximately 30– 60 meV below the conduction-band minimum, E_c, while the deep levels lie approximately 100–600 meV below E_c. To fabricate practicable nanoscale devices, such as field-effect transistors (FETs), photodetectors, and gas and chemical sensors, based on ZnO nanostructures [9][56], it is very important to understand the charge transport mechanisms first, before one may manage to control and tailor the electrical properties to meet the desired specifications. To this end, several electrical-transport measurements on single ZnO nanowires (NWs) have been reported in the literature, but those previous works were all performed with either the two-probe method [57][60] or in an FET configuration [17][61][63]. In those studies, the contact resistances, which are usually large and strongly temperature dependent, can greatly complicate the measured resistances $R(T)$ of the NW devices. As a result, the conclusions drawn from such measurements are often doubtful. For instance, it has been suggested that the variable-range hopping (VRH) conduction is the prevailing charge transport process in individual ZnO NWs [58]. (In contrast, in the present work, we shall show that the conduction mechanisms in single-crystalline ZnO NWs are due to a combination of the thermal activation and the nearest-neighbor hopping (NNH) conduction processes.) In fact, the *intrinsic* electrical-transport properties of *individual* ZnO NWs can by nomeans be resolved by employing the two-probe measurement configuration. The four-probe method over a broad range of temperature must be utilized to unambiguously uncover the intrinsic electrical resistivities, $\rho(T)$, of ZnO NWs.

In this work, we have carried out four-probe measurements over a very wide range of temperature from 300 down to 0.25 K to investigate the temperature behavior of resistivities in single ZnO NWs. Our objective is to provide an in-depth physical explanation for the electrical conduction mechanisms in this scientifically and industrially alluring semiconductor NW system. It might sound surprising to say that, even after a few decades of research efforts [49][50], together with recent resurgence of much focused attention [9], the electrical transport properties in all forms (bulks, films and NWs) of ZnO materials still remain fairly mysterious. The results of this work will help us to gain insight into the nontrivial electronic conduction mechanisms in ZnO NWs (as well as in bulks and films). A good understanding of the electrical conduction processes is a first step for the fabrication of feasible ZnO nanoelectronic and optoelectronic devices.

4.2 Experimental method

ZnO NWs were grown on quartz substrates by the standard thermal evaporation method, as has been described previously [64]. ZnO powders were placed in a quartz tube and were heated to 950 ◦C. An argon gas with a constant flow rate was input from one end of the tube to carry the evaporated ZnO to several quartz substrates which were placed in the other end of the tube and held at 500 ◦C. With the use of 100 nm Au nanoparticles as catalysts, the NWs were grown along the [0001] direction (*c* axis). X-ray diffraction and transmission electron microscopy studies indicated that the NWs were single crystalline, having a wurtzite structure, and possessed a circular cross section as displayed in Figure 4.1. Four single ZnO NWs with diameters in the range 90–200 nm and a few microns long were chosen for the present experiment. The relevant parameters for the NWs studied are listed in table 4.1.

To fabricate individual NW devices for four-probe electrical measurements, we first made micron-sized Ti/Au (10/60 nm) pads on a Si substrate which was capped with a 400 nm thick SiO2 layer. ZnO NWs were then dispersed on the SiO2-capped Si substrate. Individual ZnO NWs were identified and electrically connected to the micron-sized pads by utilizing standard electron-beam lithography and the lift-off technique. The electrodes were made of thermally evaporated Ti/Au (20/120 nm) films, as described previously [33]. A scanning electron microscopy (SEM) image of a representative four-probe NW device is shown in the inset to figure 4.2.

To improve the signal-to-noise ratio in electrical measurements, we had performed

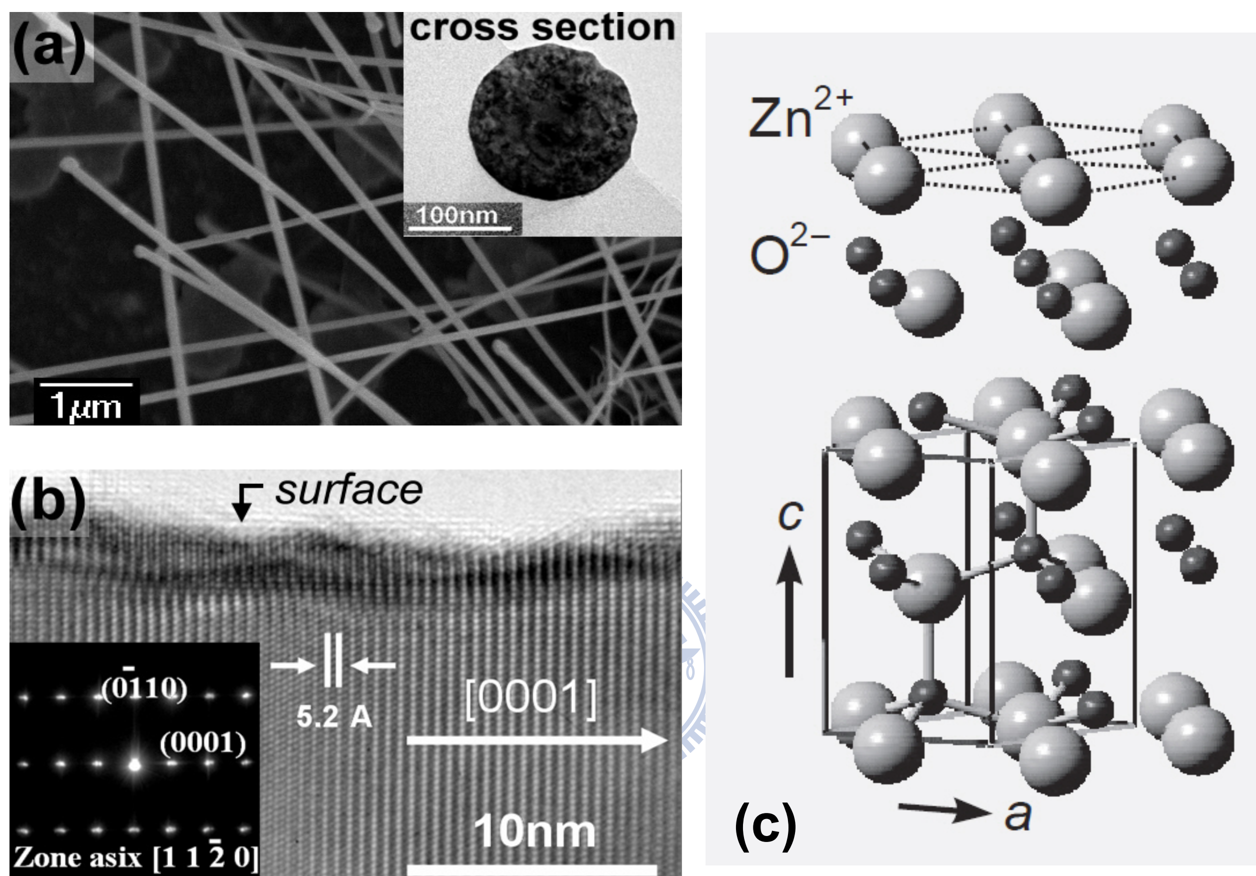

Figure 4.1: (a) An image of scanning electron microscope (SEM) of the as-grown NWs. The inset shows that the wire cross section is circular and with diameter around 100 nm. (b) A high-resolution transmission electron microscopy (TEM) image. The inset shows the corresponding selected-area electron diffraction pattern. (c) The schematic view of wurtzite crystal structure inside ZnO NWs.

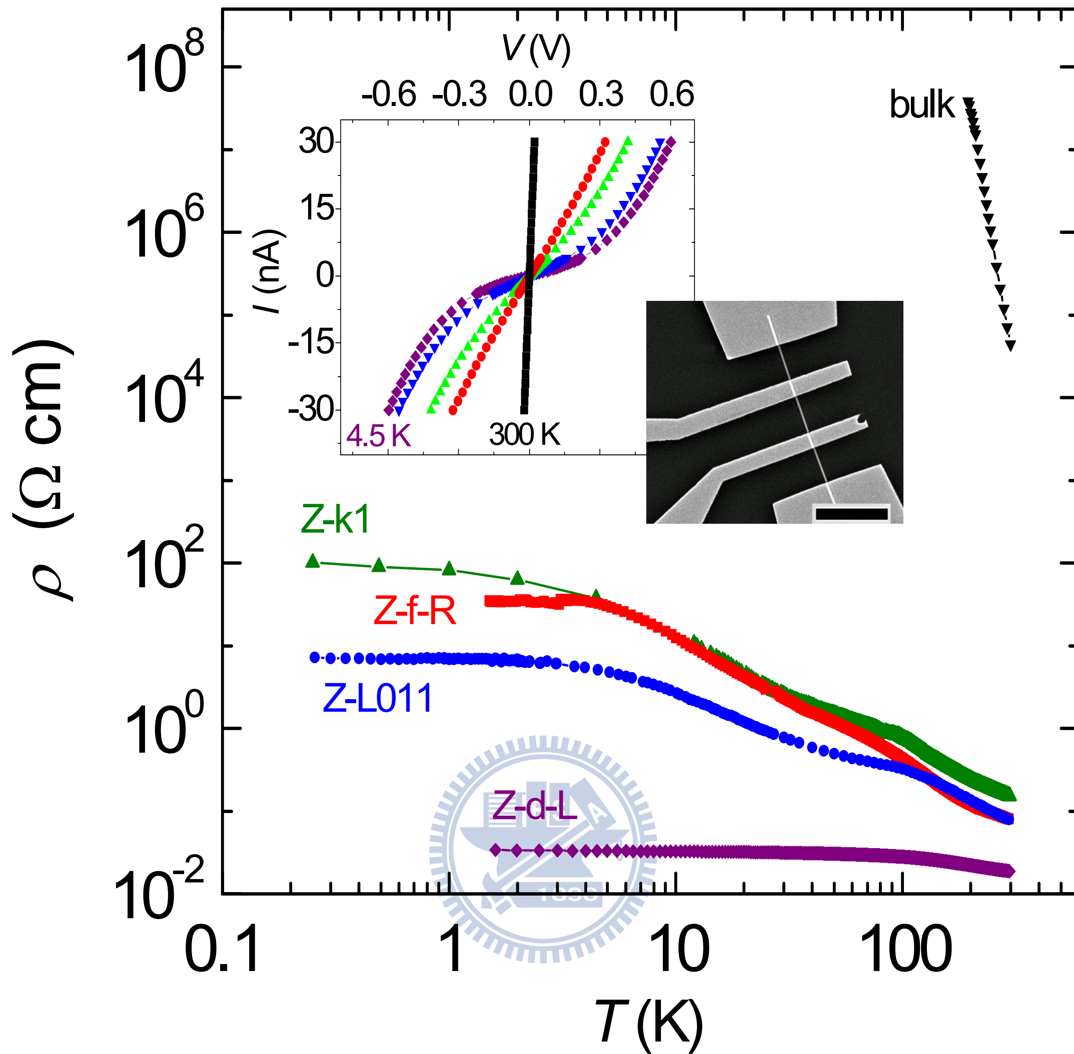

Figure 4.2: Variation of resistivity with temperature for four ZnO NWs and a bulk ZnO single crystal. The inset shows the current–voltage curves for the Z-k1 NW at 300, 30, 20, 10 and 4.5 K. Also shown is a SEM image for a four-probeNW device fabricated with electron-beam lithography. The scale bar is 5 μm. Notice that the resistivities of the natively doped NWs are several orders of magnitude lower than that of the bulk.

Table 4.1: Values of relevant parameters for four natively doped, single-crystalline ZnO NWs and a bulk single crystal. The three Z-L011, Z-f-R and Z-k1 NWs are refereed to as 'semiconducting' NWs, while the Z-d-L NW is referred to as a 'metallic-like' NW. Owing to uncertainties in the NW dimensions, the absolute values of ρ(300 K) are accurate to ≈ 10%.

Sample	d (nm)	ρ (300 K) (Ω cm)	ρ_1 (Ω cm)	E_1 (meV)	ρ_2 (Ω cm)	E_2 (meV)	ρ_3 (Ω cm)	E_3 (meV)
Bulk	—	59 800	0.028 ± 0.001	367 ±2	—	—	—	—
Z-L011	200±11	0.078	0.019 ± 0.001	44 ±1	0.29 ± 0.01	3.7 ± 0.1	1.7 ± 0.2	0.53 ± 0.04
Z-f-R	87 ± 10	0.078	0.031 ± 0.001	28 ±1	0.59 ± 0.05	4.8 ± 0.3	4.3 ± 0.1	0.94 ± 0.05
Z-k1	103 ±5	0.15	0.051 ± 0.003	34 ±1	0.71 ± 0.05	4.0 ± 0.2	9.1 ± 1.7	0.53 ± 0.07
Z-d-L	125 ± 6	0.019	—	—	—	—	—	—

post-annealing at 300 ◦C for 10–20 min in a high vacuum, which greatly reduced the contact resistances to a few k_ at room temperature. Four-probe DC measurements had been carried out, utilizing a Keithley K-220 or K-6430 as a current source and a high-impedance (TΩ) Keithley K-617 or K-6430 as a voltmeter. The NW devices were placed on a sample holder which was situated inside a dark vacuum can. The vacuum can was mounted on a standard 4He cryostat or an Oxford Heliox ^{3}He fridge. It should be noted that the resistances reported in this work were all measured by scanning the current–voltage ($I-V$) curves at various fixed temperatures between 300 and 0.25 K. The resistance at a given temperature was then determined from the regime around the zero bias voltage, where the $I-V$ curve was essentially *linear*. Notice that, since we had employed the four-probe configuration, the measured resistances (resistivities) were thus the intrinsic resistances (resistivities) of the individual NWs. For comparison, we had also measured the $\rho(T)$ of a bulk ZnO single crystal near room temperature.

4.3 Results and discussion

Figure 4.2 shows our measured resistivities $\rho(T)$ as a function of temperature for four individual NWs and a bulk ZnO single crystal. The inset shows the $I-V$ curves for the Zk1 NW at five different measurement temperatures. This figure clearly demonstrates that the resistivities increase monotonically with decreasing temperature, as would be expected for semiconductors. For comparison, we notice that the room-temperature resistivity of the bulk is 5–6 orders of magnitude higher than those of the NWs. The considerably low resistivity values of our as-grown NWs are strongly suggestive of the presence of high concentrations of native defects (dopants) in the NWs. In particular, the unintentional doping concentration is so high that the Z-d-L NW reveals metallic impurity conduction behavior [65], namely, the resistivity becomes almost temperature independent below about 70 K. For the convenience of discussion, we shall denote this Z-d-L NW as being *heavily* doped and 'metallic-like'. For the other three NWs (Z-k1, Z-f-R and Z-L011), we shall denote them as being *moderately* doped and semiconducting. We shall see below that the three semiconducting NWs lie just below, while the metallic-like NW lies just above, the Mott metal–insulator transition.

4.3.1 *Semiconducting ZnO nanowires*

In this work, we measured the resistivities over a broad range of temperature from 300 down to 0.25 K. Studies of the overall temperature behavior of resistivities will help to shed

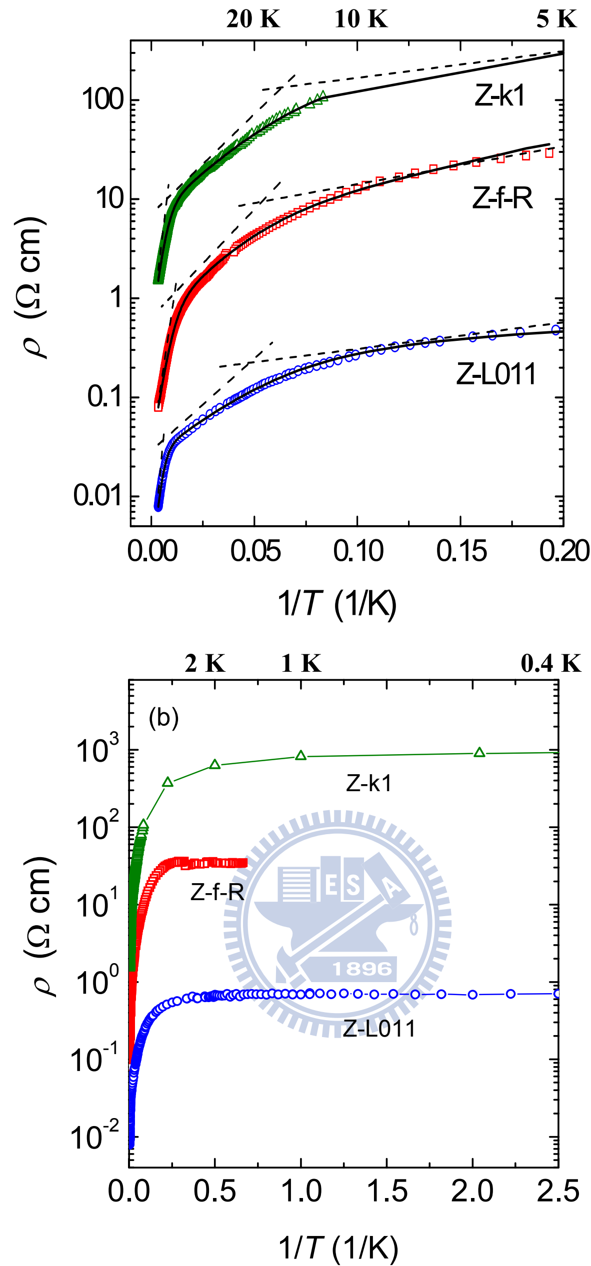

Figure 4.3: (a) Variation of resistivity with reciprocal temperature for three semiconducting ZnO NWs between 300 and 4 K. The solid curves are least-squares fits to equation (4.1). The straight dashed lines indicate the three contributions given by equation (4.1) for each NW. (b) Variation of resistivity with reciprocal temperature for the same three semiconducting ZnO NWs between 300 and 0.4 K. Notice that the resistivity essentially approaches a constant below 2–4 K in each NW. The solid curves are guides to the eye. In both (a) and (b), for clarity, the resistivity of the Z-k1 NW has been vertically shifted up by multiplying a factor of 10, while the resistivity of the Z-L011 NW has been vertically shifted down by multiplying a factor of 0.1.

light on the microscopic charge transport mechanisms in this prominent material. Figure 4.3(a) shows the variation of the resistivity with reciprocal temperature for the three semiconducting NWs between 300 and 4 K. The symbols are the experimental data and the solid curves are least-squares fits to the following equation:

$$\rho^{-1}(T) = \rho_1^{-1} e^{-E_1/k_B T} + \rho_2^{-1} e^{-E_2/k_B T} + \rho_3^{-1} e^{-E_3/k_B T} \tag{4.1}$$

where ρ_i (i = 1, 2, 3) are temperature-independent resistivity parameters, and E_i are thermal activation energies describing the electronic conduction in the high (E_1), intermediate (E_2), and low (E_3) temperature regimes. Notice that $E_1 > E_2 > E_3$ and $\rho_1 \ll \rho_2 \ll \rho_3$, as is evidenced in figure 4.3(a). Our experimental values of E_is and ρ_i s are listed in table 4.1. As for illustrations, the three straight dashed lines indicate the three contributions given by equation (4.1) for each NW. Below a few degrees kelvin, the resistivities progressively cross over to a very weakly temperature-dependent regime. Figure 4.3(b) shows a plot of the variations of resistivity with reciprocal temperature for the same three NWs from 300 K down to 0.4 K. A metallic-type regime with an essentially constant resistivity below 2–4 K is clearly found in every NW. We first discuss the temperature regime between 300 and 5 K where equation (4.1) is applicable.

The physical origin for the seemingly nontrivial temperature behavior described by equation (4.1), which contains three additive terms, can be understood in terms of the intricate material properties of nominally undoped ZnO materials. This is particularly true for ZnO NWs, where unintentional doping is often more pronounced than that in films and bulks [66]. This material property resulting complexity can partly explain why the conduction mechanisms in ZnO have remained largely unclear even after a few decades of extensive research efforts. Figure 4.4 depicts a schematic electronic density of states (DOS) diagram that could lead to the charge transport processes described by equation (4.1) [67][68]. We first explain how the material properties of ZnO NWs would give rise to the formation of a band structure like this. Then, we interpret our experimental results in figure 4.3(a) in terms of such a specific band structure. We also mention in passing that, due to the large energy gap of 3.4 eV in ZnO, the thermal excitations of carriers from the valence band to the conduction band will not occur at our measurement temperatures (~300 K). Therefore, the valence band can be totally ignored in the following discussion.

It is well accepted that as-grown ZnO NWs are often moderately (and, sometimes,

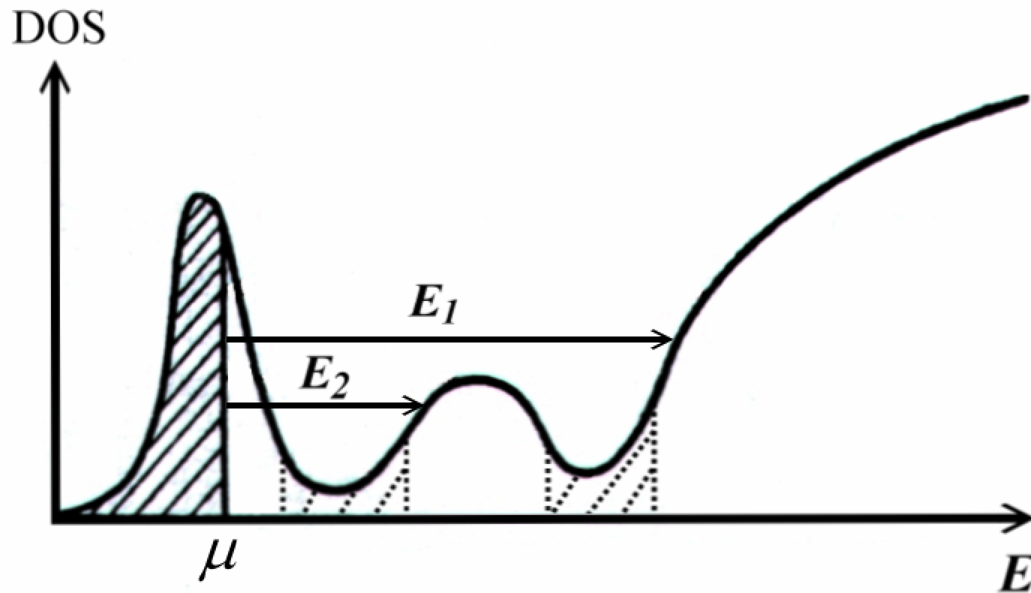

Figure 4.4: Schematic electronic density of states (DOS) diagram depicting the conduction band (E_1-conduction) and the upper D^- band (E_2-conduction) processes. The impurity band splits into two bands: the lower D band and the upper D^- band. If disorder is strong enough, the band tails will smear and overlap, leading to localized regimes with finite DOS (as hatched with dotted lines). In the case of a weak compensation, the Fermi level μ lies near the top edge of the lower D band. The presence of a small number of unoccupied donor levels which lie just above μ is not explicitly indicated. (See, for example, references [68] and [70].)

1896

highly) doped with native n-type defects [17][61][63]. According to the current understanding, the major impurity levels of isolated shallow defects in this material lie approximately 30–60 meV below E_c. However, due to the moderate-to-heavy unintentional doping, the random Coulomb fields arising from the compensating acceptors and ionized donors will cause the donor levels to disperse into an impurity band [69]. Moreover, the impurity band could further split into two bands, i.e., the lower D band and the upper D^- band [67][68][70]. The former is formed with singly charged donors while the latter is formed with neutral donors. In general, the D^- band is comparatively wider than the D band, because the singly filled neutral donor orbital is relatively larger than the singly charged donor orbital [71]. Furthermore, such large fluctuations in the Coulomb potential might also cause the tails of the two impurity bands as well as the bottom tail of the conduction band to smear into the forbidden gaps. The smearing could be so significant that the edge states from neighboring bands overlap, forming localized regimes with finite DOS. (The localized regimes are hatched with dotted lines in figure 4.4.) For moderately doped n-type ZnO NWs (which are pertinent to our three semiconducting NWs), the Fermi level, μ, lies inside the lower D band. The electronic levels below μ are occupied (denoted by the shaded regime in figure 4.4), while the levels above μ are unoccupied, at zero temperature. The presence of a small number of unoccupied levels above μ is a direct consequence of a *slight self-compensation* which *always* takes place in nominally undoped ZnO NWs [72][73]. In the case of a weak compensation, μ lies near the top edge of the D band.

The electrical conduction processes described by equation (4.1) can now be explained. Near room temperature, the electrons are thermally excited from the Fermi level μ (i.e., the donor ground state) to the conduction band where a huge amount of unoccupied, extended states with high mobilities are available. (Therefore, equation (4.1) describes the electrical conduction well below the 'exhaustion region'.) This thermal activation process is responsible for the measured E_1-conduction channel. Our measured activation energies of $E_1 \approx$ 28–44 meV in the three semiconducting NWs are in good accord with the current knowledge of the ionization energy for the major shallow donors in the ZnO materials [9][56][72]. The exact thermal ionization energies in different NWs will differ somewhat due to variations in the donor and compensator concentrations. It has been argued that these shallow donors originate from Zn interstitials, oxygen vacancies, or incidental hydrogen doping [51][52][54][55][74]. Nevertheless, a consensus has not been reached to date.

As the temperature decreases to approximately 100 K, the thermal energy k_BT (k_B is the Boltzmann constant) is no longer favorable to excite the electrons from μ to the conduction

band. Instead, the electrons may now be excited to the middle of the upper D^- band where unoccupied states are available and the carrier mobilities are relatively large, as compared with the *hopping* mobilities associated with the levels around μ. (Due to a much larger donor orbital, the wave function overlapping in the D^- band far exceeds that in the D band, giving rise to a much higher mobility.) As a result, the E_2-conduction process is experimentally realized in our semiconducting ZnO NWs at intermediate temperatures between approximately 20 and 100 K. It is important to recall that the predominant shallow donor ionization energy is sufficiently large (>/~30 meV) in the ZnO materials. Therefore, the E_1-conduction process cannot persist down to a few tens of degrees kelvin. Otherwise, the E_2-conduction regime would be squeezed and might hardly be seen in the experiment. Our measured values of E_2 are ≈4–5 meV. These extracted values are fairly reasonable, as E_2 is theoretically one half the energy gap from the Fermi level μ to the bottom (or, the lower mobility edge) of the D^- band [67]. To the best of our knowledge, the E_2-conduction mechanism has never been found in ZnO materials and any other semiconductor NWs thus far.

As the temperature further reduces to below 20 K, the thermal energy k_BT eventually becomes too small to excite the electrons from μ to the D^- band. In this case, the NNH conduction of electrons across μ becomes the dominant charge transport process. The electrons are excited from the occupied levels (neutral centers) lying slightly below μ to nearby, or the nearest-neighbor, unoccupied levels (ionized centers) lying slightly above μ. Such a phonon-assisted conduction mechanism only involves those levels falling within a narrow energy range ($\sim k_BT$) around μ. This is the E_3-, or the NNH, conduction process. As a consequence, one immediately sees that the activation energy $E3$ must assume small values ($E_3 < E_2 < E_1$). Our extracted values of E_3 are ≈0.7 ± 0.2 meV (see table 4.1). It should be stressed that NNH conduction can occur at low temperatures in this particular material, because the unintentionally doped ZnO NWs are always slightly self compensated [72][73], as discussed.

Again, the occurrence of the E_2-conduction process is a subtle issue which is closely associated with the unique and complex material properties of unintentional doped ZnO NWs. On one hand, it requires a sufficiently high concentration of dopants so that the formation of the upper D^- band, splitting from the lower D band, is substantiated. On the other hand, the degree of self-compensation in the NWs should be low such that $N_D >> N_A$, where N_D is the donor concentration and N_A is the acceptor concentration. Otherwise, in the presence of many unoccupied donor levels above μ due to a high compensation, the NNH conduction process

may persist up to sufficiently high temperatures. Thus, the inherently bounded temperature regime that could be pertinent to the E_2-conduction mechanism will be squeezed. Previously, the E_2-conduction process has only been found in very carefully doped as well as compensated semiconductors Ge [75][77], CdTe [78], GaAs [79], GaInP2 [80][81], and Ge:Sb [82].

For the three semiconducting ZnO NWs that we have studied, the values of E_i (i = 1, 2 or 3) are similar (see table 4.1). Moreover, both the crossover temperature (~100 K) from the E_1-conduction to the E_2-conduction channels and that (~20 K) from the E_2-conduction to the E_3-conduction channels are similar. These results provide a consistency check of our experimental method and our interpretation based on the specific band structure given in figure 4.4. Since these three NWs were grown simultaneously and have similar room-temperature resistivities (and hence similar donor concentrations, see below), they should possess resemblant band structures, and thus their overall temperature behaviors of the resistivity should be alike. It should be emphasized that our measured $\rho(T)$ shown in figure 4.3(a) cannot be fitted with only two conduction channels, for example, by ignoring the second term and setting $\rho_2 = \infty$in equation (4.1).

Figure 4.3(b) indicates that, in every semiconducting NW, the resistivity eventually approaches a constant below about 2–4 K. A temperature-independent resistivity implies a metalliclike behavior. This result suggests that these NWs should contain high levels of native defects and fall close to the metal–insulator transition. Owing to the presence of such a metallic-like conduction channel (which is not included in equation (4.1)), the NNH conduction term discussed above can only be observed down to around 5 K. Besides, a crossover from the NNH conduction to the VRH conduction processes at very low temperatures is not to be seen in these NWs [68].

Now we briefly comment on the previous two-probe measurements of $\rho(T)$ on individual ZnO NW devices [57][59]. In the recent experiment of Ma *et al* [58], it has been concluded that the electrical-transport mechanism is due to VRH conduction, i.e., the measured resistances are described by $R = R0 \exp(T_0/T)^{1/2}$, where R_0 is a resistance parameter, and T_0 is a characteristic temperature. The exponent 1/2 was explained as arising from the VRH conduction in the presence of Coulomb correlation effects [68]. This result is clearly in sharp contrast to our observations discussed above. In fact, we speculate that the VRH result likely reflects the measured magnitude and temperature behavior of the contact resistance(s) formed at the interface(s) between the ZnO NW and the metal electrode(s). To testify this assertion, we have recently demonstrated [64] that, in two-probe individual ZnO NW devices, the

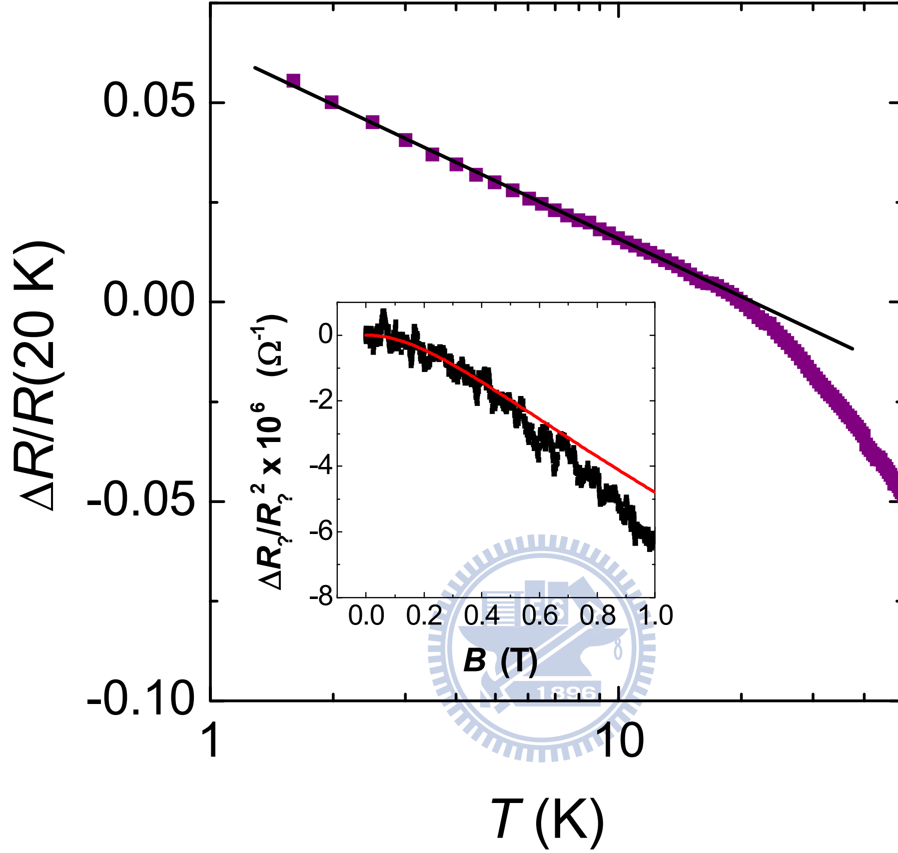

Figure 4.5: Normalized resistance, $\Delta R(T)/R(20\text{ K}) = [R(T) - R(20\text{ K})]/R(20\text{ K})$, as a function of temperature for the metallic-like Z-d-L NW, where $R(20\text{ K}) = 98.6$ kΩ. The straight solid line is a least-squares fit to the two-dimensional weak-localization and electron–electron interaction effects. The inset shows the normalized sheet magnetoresistance, $\Delta R_{\square}(B)/R_{\square}^{2}(0) = [R_{\square}(B) - R_{\square}(0)]/R_{\square}^{2}(0)$, for the same NW at 4.2 K. The solid curve is a least-squares fit to the two-dimensional weak-localization magnetoresistance theory (see text).

measured resistance can manifest either a $R \sim \exp(T_0/T)^{1/2}$ behavior characteristic of the VRH conduction, or a $R \sim \exp(E_a/T)$ behavior characteristic of the thermal activation conduction, where E_a is an activation energy. Which behavior may be observed depends crucially on the measured magnitude of the two-probe device resistance. If the two-probe device resistance is made large (e.g., R (300 K) $\geq$ several hundreds of kΩ, implying that the contact resistance dominates the measured resistance), one would often find the VRH behavior[6]. It is only when the two-probe device resistance is made sufficiently low (e.g., R (300 K) $\leq$ several tens of kΩ, implying that the contact resistance is smaller than the NW resistance), may one then find the correct attribute of the thermal activation behavior. In short, one should be very cautious about drawing any conclusion from two-probe measurements.

4.3.2 '*Metallic-like*' *ZnO nanowire and surface-related conduction*

In sharp contrast to the three semiconducting NWs shown in figures 4.3(a) and (b), the Z-d-L NW reveals 'metallic-like' conduction[7]. This is obviously due to a *heavy* doping of native defects in this particular NW. In this case, the resistivity is very low (ρ(300 K) = 0.019 Ω cm) and almost constant (≈ 0.032 Ω cm) below about 70 K (see figure 4.1). The most interesting electrical-transport properties of this NW are to be found at low temperatures. A close inspection indicates that the NW resistance increases with the *logarithm* of temperature at liquid-helium temperatures (figure 4.5). As the temperature reduces from 20 to 1 K, the normalized resistance increases by an amount $\Delta R(T)/R(20\text{ K}) = [R(1\text{ K}) - R(20\text{ K})]/R(20\text{ K}) \approx 0.04$. This magnitude and the $-\ln T$ behavior suggest that the resistance rise is due to the *two-dimensional* weak-localization and electron–electron interaction effects [85]. (A sheet resistance of $R_\square \approx 1$ k Ω will give rise to the amount of resistance rise found in figure 4.5.) That is, the electrical transport in this particular NWis *surface-related*, rather than bulk, in nature. This assertion is further supported by the observation of a small and negative

---

[6] This assertion has recently been confirmed by an independent study of a 45 nm diameter and 4 μm long two-probe ZnO NW device which had $R(300\text{ K}) \approx 3$M Ω. The VRH conduction behavior was observed between 100 and 450 K [83]. The two-probe result in figure 3 of [57], where $R(300\text{ K}) \approx 18$ M Ω, should also be better described by the VRH conduction, instead of by the thermally activated conduction, as originally proposed by the authors.

[7] Alternatively, one may say that the thermal activation energy from μ to the upper D^- band approaches zero, i.e., $E_2 \rightarrow 0$. In this case, E_2 and E_3 become indistinguishable [84].

magnetoresistance, $-\Delta R(B)/R(0) = -[R(B) - R(0)]/R(0) < 0.01$, in a perpendicular magnetic field and at 4 K. The negative magnetoresistance can be ascribed to the suppression of the two-dimensional weak-localization effect in the presence of an externally applied magnetic field [8][85]. (Notice that in magnetic fields of $\leq$ 1 Tesla, the electron–electron interaction effects cause a negligible magnetoresistance.)

The inset to figure 4.5 shows a least-squares fit of the two dimensional weak-localization magnetoresistance theory [86] (the solid curve) to the measured data (the symbols), with the characteristic electron dephasing field $H_\phi = \hbar / 4eL_\phi^2$ as the adjusting parameter, where $L_\phi = \sqrt{D\tau_\phi}$ is the electron dephasing length, D is the electron diffusion constant, and τ_ϕ is the electron dephasing time. By taking the spin–orbit scattering time $\tau_{so} >> \tau_\phi$, we obtain $L_\phi \sim 30$ nm. (The deviation of the theoretical prediction from the experimental data in the magnetic fields $B \geq 0.5$ T is expected, since the weak-localization effect is most relevant in the low-B regime.) The criterion for the two-dimensional weak-localization effect to prevail suggests that the thickness of the surface-related conducting layer, t, should satisfy the inequality $t << L_\phi$. Thus, it is plausible to conclude that t is less than a few nanometers thick. It is worth noting that the diameter d of this particular NW is 125 nm. If the diameter were much thinner (i.e., if $d < L_\phi$ and $d < L_T = \sqrt{D\hbar / k_B T}$, the electron thermal diffusion length), one might have found one-dimensional, instead of two-dimensional, weak-localization and electron–electron interaction effects [8][85][87].

Therefore, in this highly doped metallic-like NW, surface-related conduction vividly manifests itself through the two-dimensional quantum-interference transport phenomena at low temperatures. In contrast, in the three semiconducting NWs discussed above, there is no evidence in our results that could suggest any reduced-dimensional quantum-interference transport behavior. That is, in the present work, we have no experimental support to argue for a predominant surface-related conduction channel in our semiconducting NWs. This observation is very significant. It provides a powerful probe for a definitive detection of an electron accumulation layer, if any exists, in an NW. This work thus suggests that, in as-grown ZnO NWs, dominant surface-related conduction occurs only in heavily doped samples. If this is the case, the role of an electron accumulation layer in ZnO NWs might have often been overemphasized in the literature [59][88][89]. The issue requires further investigations.

For comparison, we point out that the measured magnetoresistances are positive in our

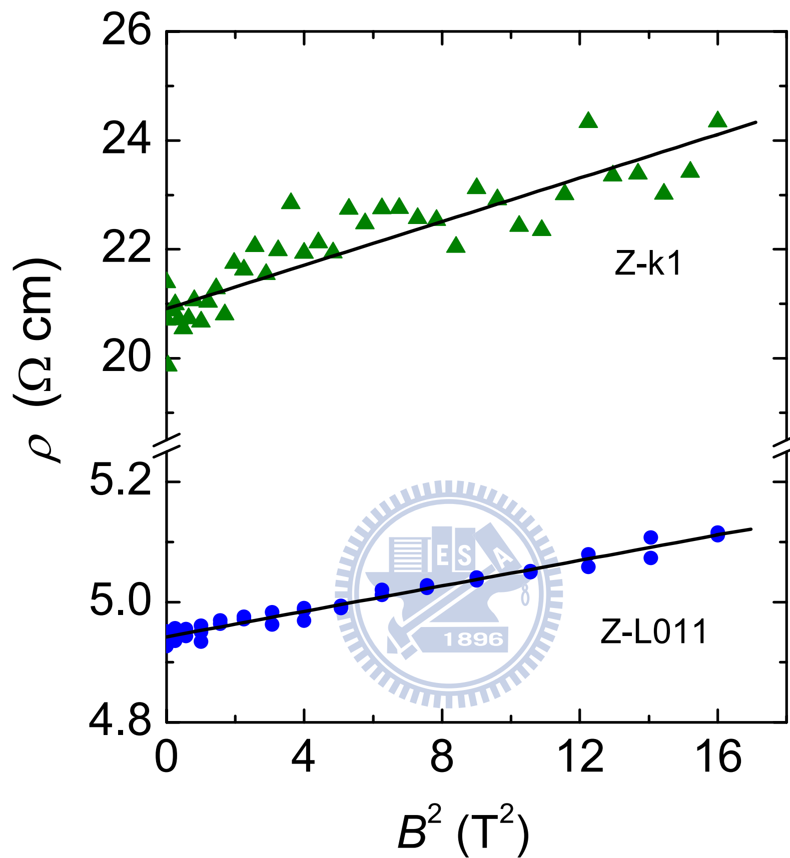

Figure 4.6: Magnetoresistivity as a function of the square of magnetic field for the Z-k1 NW at 0.255 K (triangles), and the Z-L011 NW at 4.24 K (circles). The straight solid lines are least-squares fits to the data.

semiconducting ZnO NWs at liquid-helium temperatures. Figure 4.6 shows the magnetoresistivity at 0.255 K for the Z-k1 NW (triangles) in perpendicular magnetic fields. Notice that the magnetoresistivity varies approximately with the square of magnetic field and reaches a large magnitude of $[\rho(4\ \mathrm{T}) - \rho(0)]/\rho(0) \approx 0.18$. Such magnetoresistance behavior differs significantly from the small and negative magnetoresistance behavior found in the metallic-like NW discussed above. A positive and quadratic magnetic-field dependent magnetoresistivity has also been found in the semiconducting Z-L011 NW (circles, figure 4.6) which has a low-temperature resistivity about one order of magnitude smaller than that in the Z-k1 NW. The origin and properties of the positive magnetoresistance in these semiconducting NWs deserve further studies. In short, both the resistivity and magnetoresistivity behaviors found in our semiconducting and metallic-like NWs are markedly distinct. These results provide clues to the idea that the electrical-transport properties found in the semiconducting NWs reflect bulk conduction properties while those found in the metallic-like NW largely reflect surface-related conduction properties.

4.3.3 *Estimate of carrier concentrations and the metal-insulator transition*

To understand the microscopic electronic properties in semiconductor NWs, the carrier concentration is one of the most important physical quantities to be obtained. Unfortunately, due to the small transverse dimensions of a single NW, one cannot readily perform the conventional Hall coefficient measurements to experimentally extract the carrier concentration, n, in a given sample. Fortunately, it has previously been well established that, in ZnO materials at room temperature, the carrier concentration n obeys a close correlation with the resistivity, being independent of the (film or bulk) form as well as the preparation method of the sample [90]. Therefore, we may follow this robust empirical correlation, namely, figure 4 in [90], to estimate the carrier concentrations in our NWs whose diameters are sufficiently large ($d \approx$ 90–200 nm). For our three semiconducting NWs with ρ(300 K) $\approx$ 0.1 Ω cm, we estimate the carrier concentrations to be $n \sim 6 \times 10^{17}$ cm^{-3}.[8] This value is in agreement with those values found in many nominally undoped ZnO NWs grown by various groups, where electron concentrations of the orders 10^{17}–10^{18} cm^{-3} are often reported [17][61][63]. Moreover, this value of $\sim 6 \times 10^{17}$ cm^{-3} is reasonably in line with the theoretically predicted Mott critical concentration, n_c, governing the metal–insulator transition in a doped semiconductor. For hydrogen-like donors in n-type ZnO NWs, one obtains the

[8] Accepting this n value, we obtain a mobility of ~ 100 cm^2 V^{-1} s^{-1} at 300K. This mobility value is in line with those reported in the literature [90].

effective Bohr radius $a_B \approx 1.7$ nm by taking the effective mass and the dielectric constant of ZnO into account [9][48]. From the Mott criterion $(n_c)^{1/3} a_B \sim 0.25$ for the metal–insulator transition [91], a simple calculation gives $n_c \approx 3 \times 10^{18}$ cm^{-3}.[9] Considering that many parameters in the ZnO NWs are not precisely known, we may already safely conclude that our semiconducting NWs fall below, but close to, the Mott metal–insulator transition. Moreover, as a crosscheck, recall that the E_2-conduction process can only happen for a bounded range of dopant concentration not far below n_c. Therefore, our observation of the E_2-conduction mechanism in the semiconducting NWs also provides a strong support for the above estimate of n. On the other hand, for the Zd-L NW, our room-temperature resistivity of $\rho(300\ \text{K}) \approx 0.019\ \Omega$ cm suggests a carrier concentration of $n \sim 1 \times 10^{19}$ cm^{-3}, according to the above-mentioned empirical correlation in [90]. This n value confirms that this particular NW falls slightly above the metal–insulator transition, and thus is metallic-like.

The acceptor concentrations N_A in our NWs cannot be readily determined at this stage. However, previous studies of unintentionally doped ZnO materials often found that the acceptor concentrations are one to two orders of magnitude lower than the donor concentrations N_D [51][72][93]. This result is in consistency with the requirement for the E_2-conduction process to occur in our semiconducting NWs, i.e., these samples must be weakly compensated and satisfy the condition $N_A \ll N_D$.

4.4 Summary

We have studied the intrinsic electrical conduction properties of individual, single-crystalline ZnO NWs from 300 down to 0.25 K by employing the four-probe method. The resistance at each temperature was determined from the slope of the linear $I-V$ curve around zero bias voltage. The temperature behaviors of resistivity in both the semiconducting and the metallic-like NWs have been carefully measured and the conduction mechanisms satisfactorily explained. We found the coexistence of thermal activation and nearestneighbor hopping conduction processes in the semiconducting samples, which can be understood in terms of the intricate material properties of nominally undoped ZnO NWs. In particular, these NWs are unique in the sense that they are natively moderately doped as well as slightly self-compensated. The major shallow donor levels lie below the conduction-band minimum by an amount slightly larger than the thermal energy of the room temperature (~26 meV). As a

[9] For comparison, Hutson [92] estimated a critical donor concentration of $n_c \approx 6 \times 10^{18}$ cm^{-3} in ZnO single crystals. This value is in reasonable agreement with our estimate.

consequence, as the temperature progressively reduces from 300 down to 5 K, the charge conduction processes change consecutively from conduction-band conduction to upper D^--band conduction, and then to nearest-neighbor hopping conduction. Since the conduction processes depend subtly on the specific band structure of natively doped ZnO NWs, the observation of the E_2-conduction mechanism is a unique characteristic of this particular semiconductor NW system. A predominant surface-related conduction channel manifesting two-dimensional weak-localization and electron–electron interaction effects is observed in a heavily doped, metallic-like NW. Estimates of the carrier concentrations indicate that our semiconducting NWs lie just below, while our metallic-like NW lies just above, the Mott metal–insulator transition.

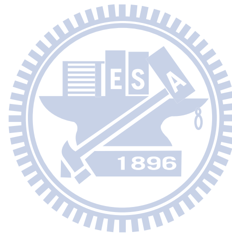

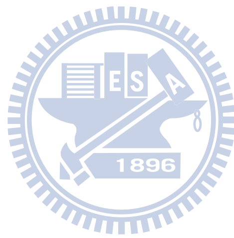

Chapter 5

Electrical transport in doped ZnO Nanowires

5.1 Introduction

In this chapter, we investigate the electrical transport properties in two kinds of doped-ZnO nanowires, one is indium-doped, and another is lead-doped. The author of recent experimental result [11] of the In:ZnO NW concludes that there is no surface-related conduction in their In:ZnO NW. It seems contrary to our previous result in a metallic-like natively doped ZnO NW [21]. Thus the issue of surface-related conduction will be discussed in the following context. The doped ZnO NWs reveal the features of the diffusive system and the degenerate Fermi gas. The quantum interference effects are expected to be significant in our samples, hence the WL effects of different dimensionalities and electron-electron interaction are utilized as powerful tools to understand the special electrical transport properties in these doped ZnO NWs.

5.2 Theoretical background

5.2.1 *Weak localization effect and the related magnetoresistance*

In the disordered conductors, the scatters, such as the defects and the impurities, cause the diffusive motion of the electrons. After many (elastic) scattering events with the scatters, the electron waves have the chance to go through close trajectories and back to the original sites. The weak localization (WL) effect results from the constructive interference between the pair of time-reversal complementary electron waves which propagate on the close trajectories. The size of the effective close trajectories is restricted by the phase coherent length, L_ϕ. The L_ϕ is the length scale between two phase-breaking (or say, inelastic) scattering events, or the length scale corresponding to the phase-randomizing processes. Therefore L_ϕ is affected by the electron-electron scattering, electron-phonon scattering, magnetic field, and so on. In a magnetic field, the magnetic flux enclosed by the close trajectories makes an additional phase difference and disturbs the constructive interference of the complementary electron waves, hence the effective L_ϕ is shrunk and the WL effect is weakened by the

magnetic field. This process generates the low-field sensitive magnetoresistance (MR). The L_ϕ is also important for determining the dimensionalities of the WL effects, such that there are different functional forms of the MRs corresponding to different dimensionalities.

The one-dimensional (1D) WL effect predicts the MRs as follows [98][99]

$$\frac{\Delta R(B)}{R(0)} = \frac{e^2}{2\pi\hbar}\frac{R}{L}\left\{3\left[\left(L_\phi^{-2}+\frac{4}{3L_{SO}^2}+\frac{1}{D\tau_B}\right)^{-1/2}-\left(L_\phi^{-2}+\frac{4}{3L_{SO}^2}\right)^{-1/2}\right] - \left[\left(L_\phi^{-2}+\frac{1}{D\tau_B}\right)^{-1/2}-L_\phi\right]\right\} \tag{5.1}$$

where R is the resistance of a quasi-1D wire of length L, L_{so} is the spin-orbit scattering length, D is the electron diffusion constant, and the time τ_B represents the dephasing ability of the magnetic field, B. τ_B depends on the direction of magnetic fields and the shape of sample [98]. For a wire of circular cross section with a radius r, in a magnetic field parallel to the wire axis, the time is $\tau_B = 2L_B^4 / Dr^2$. For a wire of rectangular cross section with a width a, in a magnetic field perpendicular to the wire axis, the time is $\tau_B = 3L_B^4 / Da^2$. Here the magnetic length, L_B is defined as $L_B = \sqrt{\hbar / eB}$. If we consider that there is an inhomogeneous current flux through the cross section of the wire (discuss for our samples in detail later), the effective area, A, for the electrical conduction would be $A \sim a^2 \sim \pi r^2$, and the a and r are no longer the dimensions of devices, but change to some effective values. The length-scale requirement for the 1D WL effect is that the L_ϕ should be longer than a or $2r$, while smaller than L.

When an electron is scattered by impurities or defects, the electron enters into the orbits of the impurity atom and its orbital motion may couple to its own spin. This coupling is known as spin-orbit coupling (or scattering). Formally the coupling looks like the interaction of two magnetic dipoles and depends on the angle between the orbital angular momentum and the spin. The length, L_{so}, characterizes the strength of spin-orbit scattering. If the spin-orbit scattering is strong such that $L_{so} << L_\phi$, it changes the interference from constructive (weak localization) to destructive (weak anti-localization), hence the low-field MR changes sign to positive variation.

The MRs due to 2D WL effect under the magnetic field perpendicular to the plane of quasi-2D systems (e.g. a thin film with length, L, and width, w) is [102][103]

$$\frac{\Delta R_{\square}(B)}{R_{\square}^2(0)}=\frac{e^2}{2\pi^2\hbar}\left\{\Psi\left(\frac{1}{2}+\frac{B_1}{B}\right)-\frac{3}{2}\Psi\left(\frac{1}{2}+\frac{B_2}{B}\right)+\frac{1}{2}\Psi\left(\frac{1}{2}+\frac{B_3}{B}\right)-\frac{1}{2}\ln\frac{B_1^2B_3}{B_2^3}\right\} \tag{5.2}$$

where $R_{\square}$ is the sheet resistance, Ψ is the digamma function. B_1, B_2, and B_3 are consist of several characteristic fields (B_e, B_{so}, B_s, and B_i) as follows

$$\begin{aligned} B_1 &= B_e + B_{so} + B_s \sim B_e \\ B_2 &= \frac{4}{3}B_{so}+\frac{2}{3}B_s + B_i \\ B_3 &= B_i + 2B_s \end{aligned} \tag{5.2a}$$

where the characteristic fields are connected with the characteristic relaxation times τ_n by the relation $B_n\tau_n = \hbar/4eD$, where the indices stand for the following scattering processes: 'e' means potential scattering (i.e. elastic scattering), '*i*' means inelastic scattering, '*so*' means spin-orbit scattering, and '*s*' means magnetic scattering. In the condition of no magnetic impurities, B_s is set to zero. The elastic mean free time is relatively small in dirty metals, therefore $B_1 \sim B_e$. If we consider the thin film is warped, i.e. not flat, the magnetic flux would be changed. In this situation, the film width, *w*, is no longer the original width of the film, but changes to an effective value. For 2D systems, because $R = R_{\square}\cdot L/w$ (or $R_{\square} = R\cdot w/L$), we can set the *w* as an adjustable parameter inside the sheet resistance, $R_{\square}$. This concept will be used when we analyze the MRs of doped ZnO NWs which may be related to their surfaces.

The MRs due to 2D WL effect under the magnetic field parallel to the plane of thin films with film thickness *t* is [106]

$$\frac{\Delta R(B_{\parallel})}{R(0)}=-\frac{e^2R_{\square}}{2\pi^2\hbar}\left\{\frac{3}{2}\ln\left(1+\frac{L_2^2}{L_{\parallel}^2}\right)-\frac{1}{2}\ln\left(1+\frac{L_3^2}{L_{\parallel}^2}\right)\right\} \tag{5.3}$$

where we define the length L_2 and L_3 in analogy with B_2 and B_3 by $L_n^2 = D\tau_n = \hbar/4eB_n$. In the Eq. (5.3), we already set the B_s to zero. The parallel field length $L_{\parallel}=\sqrt{3}\hbar/eBt$ takes different forms depending on the relative magnitude of the elastic mean free path, *l*, and the (effective) film thickness, *t*, for the quasi-2D structures. In the dirty limit (small *l*), one has

$L_{\|} = \sqrt{3}\hbar / eB_{\|}t$, while in the clean limit (large l), $L_{\|} = \sqrt{16l/3t}(\hbar / eB_{\|}t)$. The length-scale requirement for the 2D WL effect is that the L_{ϕ} should be longer than t, while smaller than the length and width of the thin film.

The MRs from three-dimensional (3D) WL effect under the condition of weakly Zeeman splitting would be [39]

$$\frac{\Delta\rho(B)}{\rho^2(0)} = -\frac{e^2}{2\pi^2\hbar}\sqrt{\frac{eB}{\hbar}}\left\{\frac{3}{2}f_3(\frac{B}{B_2}) - (\frac{1}{2}+\beta)f_3(\frac{B}{B_\phi})\right\} \tag{5.4}$$

where ρ is the resistivity, B_2 is the same as that mentioned above, β is the Maki-Thompson superconducting fluctuation contribution. If there is no superconductivity in the systems, β is set to zero. The function f_3 is an infinite series which can be approximately expressed as

$$f_3(z) \approx 2\left[\sqrt{2+\frac{1}{z}} - \sqrt{\frac{1}{z}}\right] - \left[\left(\frac{1}{2}+\frac{1}{z}\right)^{-1/2} + \left(\frac{3}{2}+\frac{1}{z}\right)^{-1/2}\right] + \frac{1}{48}\left(2.03+\frac{1}{z}\right)^{-3/2} \tag{5.4a}$$

The length-scale requirement for the 3D WL effect is that the L_{ϕ} should be shorter than the lengths of all three dimensions.

From literatures we know that the higher field behavior of MRs is less well described by the theories. There are some reasons [103]. First, in the sufficient high magnetic field the magnetic length, L_B (recall $L_B = \sqrt{\hbar / eB}$), dominates the scale of coherent length. For the low dimensional (1D and 2D) structures, if magnetic field keeps increasing to make L_B smaller than the wire width, a, or the film thickness, t, the wire or the film are no longer 1D and 2D respectively. The second reason is more intrinsic in the derivation of the theories. There are some high order terms omitted in calculation, and it cause high-field deviation spontaneously [103]. However this high-field deviation is difficult to calculate.

5.2.2 *Dephasing mechanisms*

The magnitude of the phase coherent length, L_{ϕ}, is determined by the dephasing mechanisms, such as magnetic field, electron-electron scattering, electron-phonon scattering, and other temperature-independent scatterings. The effect of magnetic field causes the low-field sensitive MRs mentioned above. The L_{ϕ} links to the phase coherent time, τ_{ϕ}, through

the relation, $L_\phi = \sqrt{D\tau_\phi}$. The reciprocal of τ_ϕ is just the dephasing rate. We often express that the τ_ϕ^{-1} consists of several dephasing rates through the relation $\tau_\phi^{-1} = \tau_0^{-1} + \tau_i^{-1}(T)$, where τ_0^{-1} is a temperature-independent scattering rate, and τ_i^{-1} is the inelastic scattering rate. The τ_0^{-1} may originate from magnetic impurities, dynamic defects, high frequency noise, and so on [8]. The low-temperature saturation of τ_ϕ^{-1} is the consequence of the existence of τ_0^{-1}. The τ_i^{-1} consists of electron-electron (e-e) and electron-phonon (e-ph) scattering rates, τ_{ee}^{-1} and τ_{ep}^{-1} respectively. We'll briefly introduce these two scattering as follows.

Electron-electron scattering

The e-e scatterings can be divided into two kinds of processes which involve with small and large energy transfers respectively. The e-e scattering rate with small energy transfer is denoted by τ_N^{-1} which results from the effect of electromagnetic fluctuation, or says, the Nyquist relaxation process. The e-e scattering rate with large energy transfer is denoted by $\tau_{i,ee}^{-1}$ which can be viewed with the physical picture of particle collision. Therefore the energy relaxation is mainly served by this process. Both processes have the contribution of phase relaxation, hence $\tau_{ee}^{-1} = \tau_{i,ee}^{-1} + \tau_N^{-1}$. Altshuler et al have found that in disordered conductors the e-e scattering rates would be [39]

$$\tau_N^{-1} \sim \left(\frac{T}{D^{d/2} \nu_d \hbar^2} \right)^{2/(4-d)}, \ d = 1 \text{ or } 2 \tag{5.5}$$

$$\tau_{i,ee}^{-1} \sim \left(\frac{k_B T}{\hbar D} \right)^{d/2} \frac{1}{\nu_d \hbar}, \ d = 1, 2, \text{ or } 3 \tag{5.6}$$

where d is dimensionality, and ν_d is the density of states for the corresponding dimensionality. Comparing with Eq. (5.5) and (5.6), they found that in low dimensional systems, the phase relaxation rate is dominated by τ_N^{-1}, while in three dimensional systems, the phase relaxation rate is dominated by $\tau_{i,ee}^{-1}$. It should be noted that the characteristic length for $\tau_{i,ee}^{-1}$ is the thermal diffusion length, L_T, while the characteristic length for τ_N^{-1} is the Nyquist length, L_N ($L_N = \sqrt{D\tau_N}$).

Electron-phonon scattering

The e-ph scattering rate is often expressed as $\tau_{ep}{}^{-1} = A_{ep}T^{p}$, where A_{ep} is a coefficient related to electron-phonon coupling strength. The temperature exponent p varies in different theoretical models. Experimentally, p~2 is often encountered in three-dimensional disordered conductors. Sergeev and Mitin [111] consider the impurities can vibrate in phase with the host lattice or be static. The former condition yields $\tau_{ep}{}^{-1} \sim T^{4}l$, while the later condition yields $\tau_{ep}{}^{-1} \sim T^{2}/l$, where l is the elastic mean free path for electrons.

5.2.3 *Electron-electron interaction*

The WL effect only involves one electron whose time-reversal complementary waves mutually interfere. It's not many-body effect and does not change the density of states (DOS) of the degenerate Fermi gas. If considering the interference among electrons, the heavy elastic scattering in the diffusive systems causes the changes of screening effect and the shape of DOS near the Fermi level, $N(E_F)$. The dip structures known as zero-bias anomaly in the experiments of tunneling junctions [94], reflects the shape of altered DOS. The change of DOS at Fermi level, $\Delta N(E_F)$, also reflects on the unusual behavior of low-temperature conductivities (or resistivities), which is just called the effect of electron-electron interaction (EEI). The $\Delta N(E_F)$ is a function of temperature, therefore the low-temperature conductivity follows the same dependence of temperature. The conductivity correction due to the EEI is [39][95]

$$\Delta\sigma(T) = \frac{e^2}{4\pi^2\hbar}\left(\frac{4}{d} - \frac{3}{2}\tilde{F}\right)\left(\frac{k_B T}{\hbar D}\right)^{d/2-1} \times \begin{cases} -4.91, & d = 1 \\ \ln\left(\frac{k_B T\tau}{\hbar}\right), & d = 2 \\ 0.915, & d = 3 \end{cases} \tag{5.7}$$

where σ is the conductivity, the first term is from exchange process and the second term is from Hartree process, $\tilde{F}$ is the coupling constant of Hartree processes, and d is the dimensionality. The thermal diffusion length, L_T, is embedded in the $(k_B T/\hbar D)^{d/2-1}$ term. For d=3, we have $\Delta\sigma \propto (k_B T/\hbar D)^{1/2} \propto \sqrt{T}$, for d=2, we have $\Delta\sigma \propto \ln T$, and for d=1, we have $\Delta\sigma \propto 1/\sqrt{T}$. The different temperature behavior for different dimensionalities can give us some hints about the dimensions of our samples.

5.3 Indium-doped ZnO (In:ZnO) nanowures

5.3.1 *Sample information*

The In:ZnO nanowires are synthesized by the laser-assisted chemical vapor deposition (CVD) method [11]. In the Figure 5.1(a), the image of scanning electron microscope (SEM) shows that the In:ZnO nanowires with diameters ranging roughly from 40 to 100 nm are formed on tin-coated silicon substrates. In the Figure 5.1(b), high resolution transmission electron microscopy (HRTEM) and selected-area electron diffraction pattern (in the inset) reveal that the indium atoms are well incorporated into the wurtzite crystal lattice and the single crystalline structure with the (0001) growth direction is maintained. Although the HRTEM image shows good arrangement of atoms, some defects (maybe due to the mismatch of the atomic radii between In and Zn) are still present and affect the electrical transport substantially at liquid helium temperatures. The energy dispersive X-ray (EDX) spectrum (as displayed in Figure 5.1(c)) shows that the indium to zinc atomic ratio is around 3%. We have made several single-nanowire devices in contact with four electrodes. The careful measurement of magneto-transport and thorough analysis were performed on two of the devices, labeled IZOa and IZOb. Some parameters of the In:ZnO nanowire devices are listed in Table 5.1(a) and Table 5.1(b).

The room temperature resistivities of IZOa and IZOb are $1.24\text{x}10^{-2}$ and $6.36\text{x}10^{-3}$ Ω cm, respectively, roughly one order of magnitude lower than those of nominally undoped-ZnO nanowires [21]. We plot the resistivity versus temperature for undoped and doped ZnO nanowires in the Figure 5.2(a), which shows that the whole temperature behavior of doped-ZnO nanowires are very different from those of undoped-ZnO nanowires and seem to possess weakly temperature dependence as displayed in Figure 5.2(b). For the sample IZOb, its resistivity decreased like a metal from room temperature to 180 K, then turned to a monotonically ascending trend from 180 K to the lowest temperature. This dirty-metal-like behavior reveals that the impurity band and conduction band are overlapped and the Fermi level moves into an energy regime with continuous extended states to form a degenerate Fermi gas. Analogous band structure and temperature behavior of resistivity also happen in tin-doped indium oxide (ITO) [97]. The sample IZOa (also PZOe) possesses a little higher resistivity than IZOb and shows a slowly monotonic increasing as temperature decreasing from room temperature to liquid helium temperatures (shown in Figure 5.2(b)). Combining this feature with its own carrier concentration (n~$6.8\text{x}10^{18}$ cm^{-3} versus the critical carrier

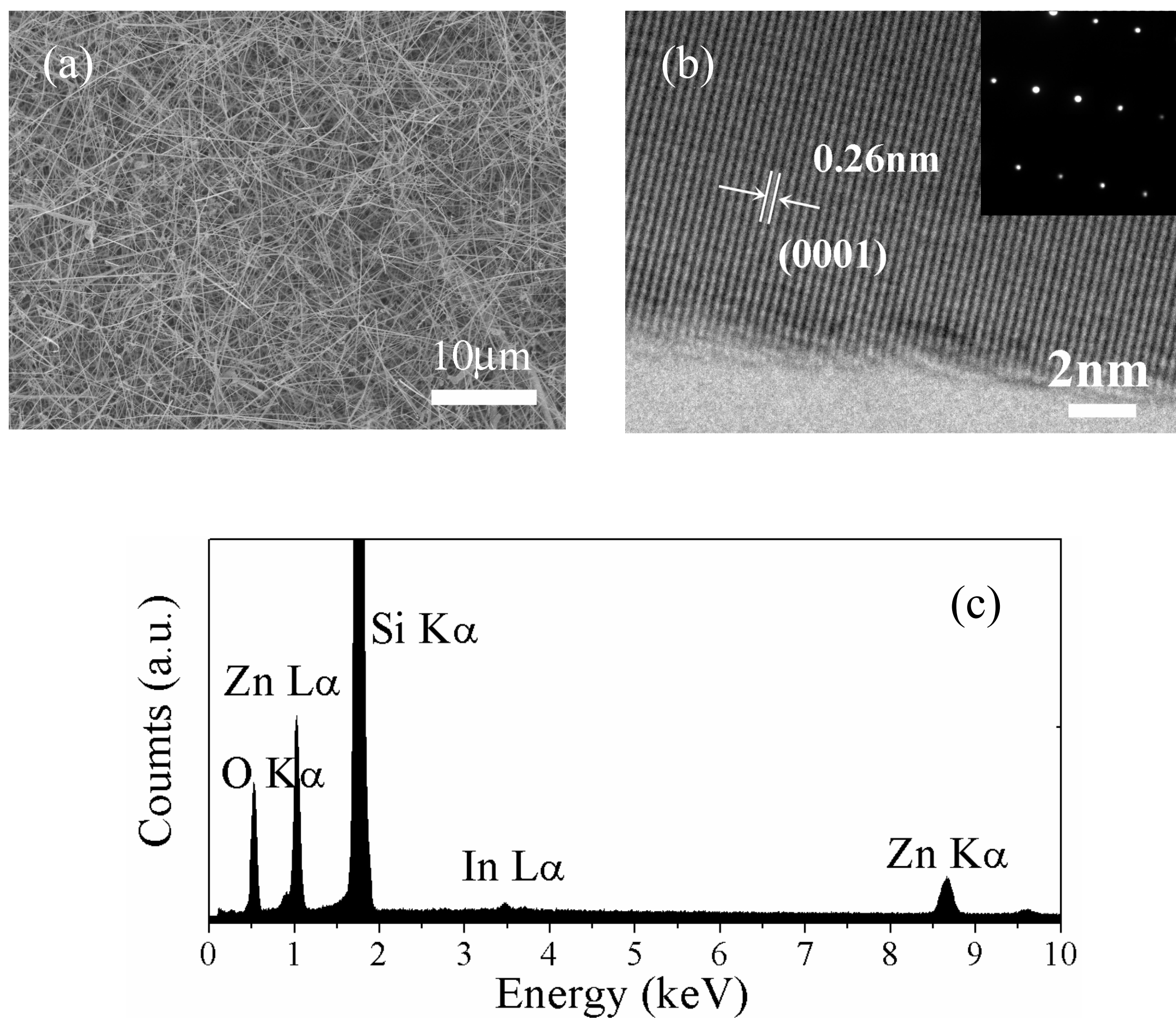

Figure 5.1: (a) A SEM image of the as-grown In:ZnO nanowires on the silicon substrate. (b) A high-resolution TEM image for a single nanowire. The inset shows the corresponding selected-area electron diffraction pattern. (c) EDX spectrum of In:ZnO nanowires. The indium to zinc atomic ratio is around 3%.

Table 5.1(a): Parameters for the doped-ZnO nanowire devices. *dia.* is the nanowire diameter, L is the nanowire length between the two voltage electrodes in the four-probe configuration, R (300 K) is the resistance at 300 K, ρ(300 K) and ρ(10 K) are the resistivities at 300 K and 10 K, respectively, n is the carrier concentration estimated from ρ(10 K), l is the electron mean free path, and D is the electron diffusion constant. The values of l and D are calculated from ρ(10 K) and n.

Sample	*dia.* (nm)	L (μm)	R (300 K) (kΩ)	ρ(300 K) (Ω cm)	ρ(10 K) (Ω cm)	n (cm^{-3})	l (nm)	D (m^2/s)
IZOa	92	1.9	35.5	$1.24x10^{-2}$	$1.49x10^{-2}$	$6.8x10^{18}$	2.4	$2.23x10^{-4}$
IZOb	68	3.8	66.6	$6.36x10^{-3}$	$6.74x10^{-3}$	$1.7x10^{19}$	2.8	$3.62x10^{-4}$
PZOe	80	2.4	55.6	$1.16x10^{-2}$	$1.45x10^{-2}$	$7.1x10^{18}$	2.6	$2.26x10^{-4}$

Table 5.1(b): Parameters for the doped-ZnO nanowire devices. l (τ) is the electron mean free path (time), k_F is the Fermi wavenumber, v_F is the Fermi velocity, E_F is the Fermi energy, λ_F is the Fermi wavelength, $k_F l$ is the value by multiplying k_F and l, and L_T is the thermal diffusion length which defined as $L_T = \sqrt{D\hbar / k_B T}$.

Sample	l (nm)	τ (sec)	k_F (m^{-1})	v_F (m/sec)	E_F (eV)	λ_F (nm)	$k_F l$	L_T (10 K) (nm)
IZOa	2.4	$8.4x10^{-15}$	$5.9x10^{8}$	$2.8x10^{5}$	0.055	10.7	1.4	13.1
IZOb	2.8	$7.3x10^{-15}$	$8.0x10^{8}$	$3.9x10^{5}$	0.1	7.8	2.3	16.6
PZOe	2.6	$8.3x10^{-15}$	$6.0x10^{8}$	$2.9x10^{5}$	0.056	10.6	1.4	13.2

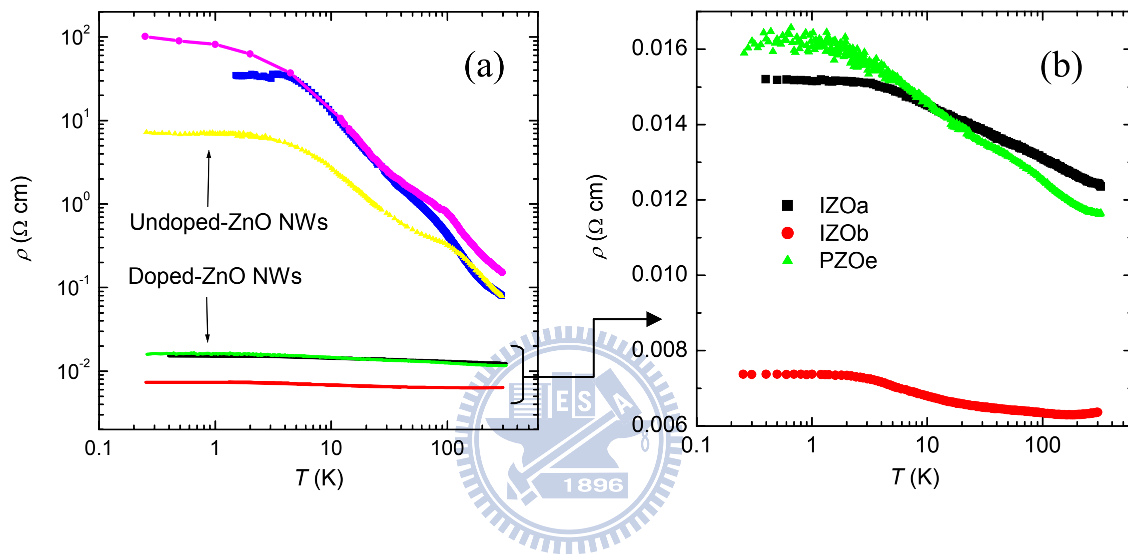

Figure 5.2: (a) Compare the temperature behaviors of the resistivity of undoped-ZnO nanowires and doped-ZnO nanowires. The upper three curves belong to the undoped-ZnO nanowires. The lower three curves belong to doped-ZnO nanowires. (b) Zoom in to show the three curves of doped-ZnO nanowires in detail. IZOa and IZOb are the samples of In-doped ZnO nanowires. PZOe is the sample of Pb-doped ZnO nanowires.

concentration, $n_c \sim 3\text{x}10^{18}$ cm^{-3}, for metal-insulator transition in ZnO [21]) implies that this sample is close to the metal-insulator transition but still in the metal side.

The relation between resistivity and carrier concentration of doped and undoped ZnO was discussed in literature and abundant data were collected to build an empirical form [90]. According to this empirical form, we can evaluate the carrier concentration from the resistivity. The estimated carrier concentrations of three samples are listed in Table 5.1(a). To know how reliable of this estimation, we can compare it with the carrier concentration measured by back-gate method [11]. An In:ZnO nanowire, its resistivity was $2.7\text{x}10^{-3}$ Ω cm at 4 K, possessed carrier concentration of $1.2\text{x}10^{20}$ cm^{-3} determined by back-gate method [11]. From the empirical form [90], the resistivity, $2.7\text{x}10^{-3}$ Ω cm, corresponds to the carrier concentration ~$8\text{x}10^{19}$ cm^{-3} which is a little smaller but consistent with the result of back-gate method, and only few influence if we use these two n's to calculate other parameters.

Utilizing the free electron model, some characteristic parameters for our samples are calculated as follows. The Fermi wavenumber is $k_F = (3\pi^2 n)^{1/3}$. The Fermi velocity is $v_F = \hbar k_F / m^*$, here m^*=0.24 m_0 is the electron effective mass of ZnO [96]. For IZOa, $v_F \sim$ $2.8\text{x}10^5$ m/sec and for IZOb, $v_F \sim 3.9\text{x}10^5$ m/sec. Thus the Fermi energies of IZOa and IZOb are 0.055 and 0.1 eV, respectively. Both of them are much larger than the thermal energy at 10 K, leading to the behavior of degenerate Fermi gas. The elastic mean free path of electrons is $l = 3\pi^2 \hbar / (k_F^2 e^2 \rho_0)$, here ρ_0 is the residual resistivity at low temperature. We substitute ρ_0 with ρ(10 K) to estimate l. The relative short l (l < 3 nm) comparing with the wire diameters suggests us that our samples should be three-dimensional diffusive system. Thus the diffusion constant D is calculated with $D=v_F l/d$, here d is dimensionality and d=3. The thermal diffusion lengths, L_T, characterizing the electron-electron interaction, are calculated with $L_T = \sqrt{D\hbar / k_B T}$. The $k_F l$ in the order of unity means that the elastic mean free path, l, and Fermi wavelength, λ_F, are of the same order of magnitude and the quantum interference effects, such as weak localization, electron-electron interaction, and universal conductance fluctuation, will be significant in our samples.

5.3.2 *Magnetoresistance and weak localization effect*

The magnetoresistances (MR) of IZOa and IZOb are presented in Figure 5.3 and Figure 5.4. We have done the measurement in the magnetic fields perpendicular and parallel to the wire axis at the temperatures ranging from 0.26 K to 70 K. In these figures, because of poorer

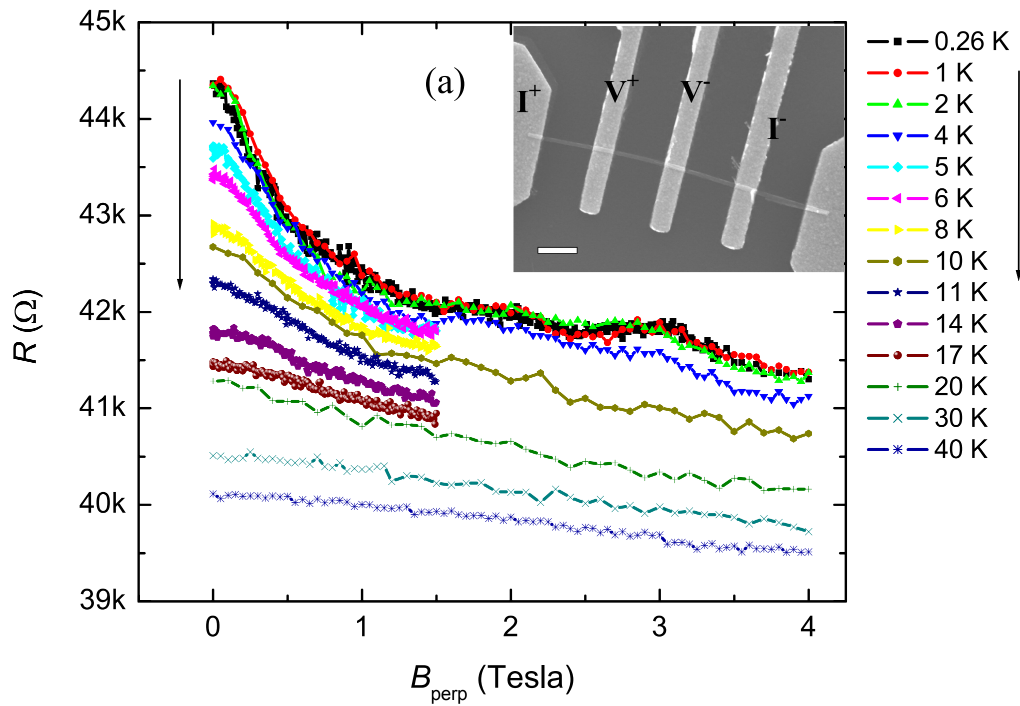

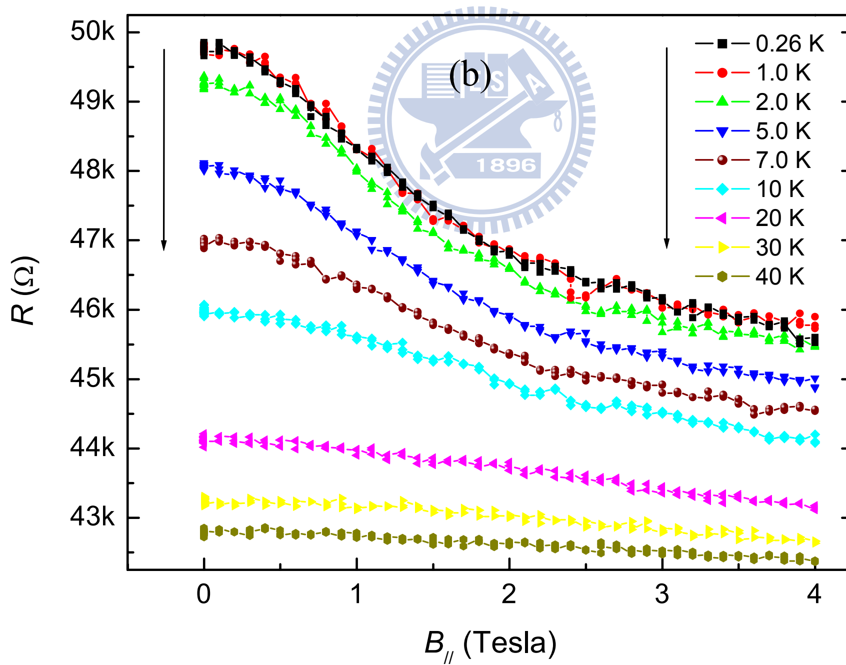

Figure 5.3: For sample IZOa. (a) Magnetoresistances as a function of perpendicular magnetic field at different temperatures. The inset shows an SEM image of IZOa nanowire device. We perform four-probe measurement through the four electrodes marked by I^+, V^+, V^-, I^-. The scale bar is 1 μm. (b) Magnetoresistances as a function of *parallel* magnetic field at different temperatures.

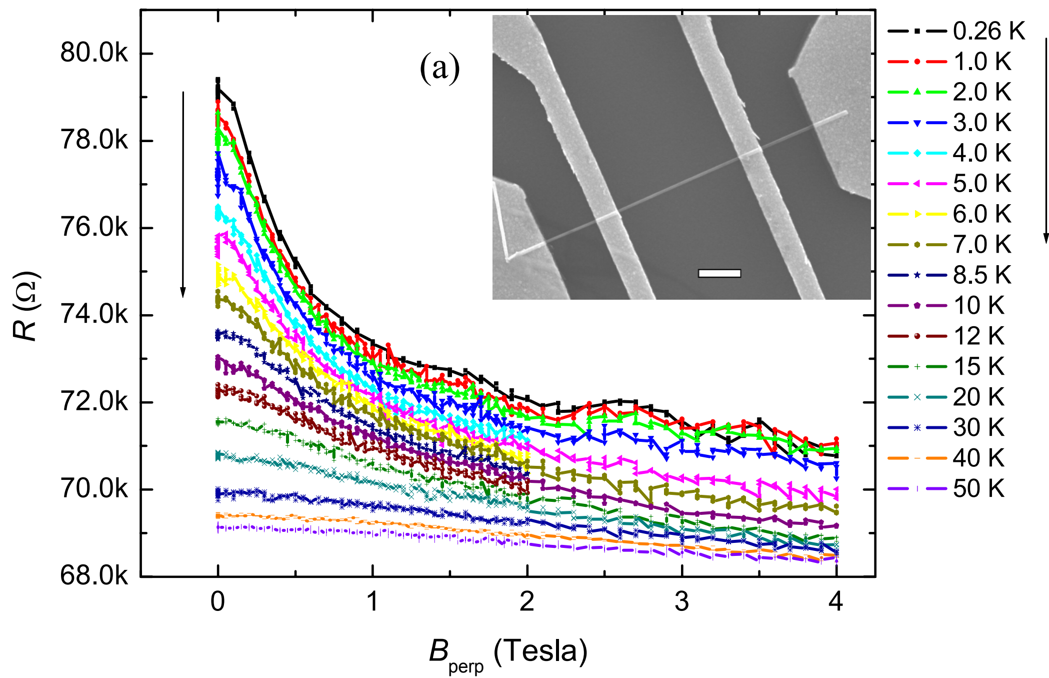

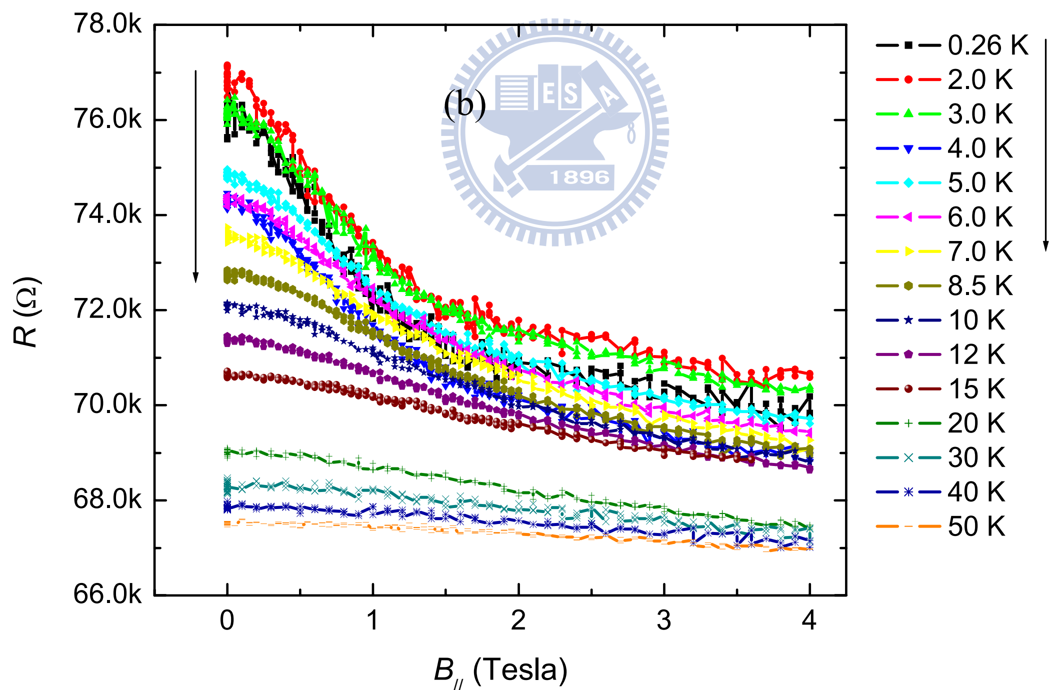

Figure 5.4: For sample IZOb. (a) Magnetoresistances as a function of perpendicular magnetic field at different temperatures. The inset shows an SEM image of IZOb nanowire device. The scale bar is 1 μm. (b) Magnetoresistances as a function of *parallel* magnetic field at different temperatures.

signal to noise ratio at higher temperatures, and for clearly displaying the data, we omit some of the data at high temperatures (e.g. 50 K, 60 K, and 70 K). The scanning electron microscopy (SEM) images of these two samples are shown in the insets of Figure 5.3(a) and Figure 5.4(a). The Figures reveal that the variations of the MRs are always negative, implying a weaker spin-orbit scattering rate relative to the inelastic scattering rate even down to 0.26 K.

For sample IZOa, MR of perpendicular magnetic field at lower temperatures between 0.26 K and 8 K are least-squares fitted to the one-dimensional weak-localization theoretical prediction, i.e., Eq. (5.1) with $\tau_B = 3L_B^4 / Da^2$. Figure 5.5(a) shows the normalized magnetoresistance, $\Delta R(B)/R(0)$ = $[R(B)$ - $R(0)]/R(0)$, and the fitted curves at several temperatures between 0.26 K and 8 K. There are three parameters for curve fitting, L_ϕ, L_{so}, and a. The spin-orbit scattering length, L_{so}, and the effective wire width, a, are both independent of temperature. In the first run of curve fitting, all three parameters are set to free to fit the MR data at different temperatures. We can obtain the averaged values of L_{so}=133 nm and a=72 nm from the results of different temperatures. (Later, in the section 5.3.4 we'll discuss why the effective wire width, a=72 nm, would be shorter than the wire diameter.) Then we fix L_{so} and a to the averaged values and leave the phase coherent length, L_ϕ, as the only free parameter and run curve fitting again. The extracted L_ϕ's are the square symbols in the Figure 5.9(a). The L_ϕ at 0.26 K is 54 nm. Although the low-field part of the data seems to be well described by the Eq. (5.1), the L_ϕ's are unreasonably shorter than the effective wire width, a (72 nm for IZOa), and also the wire diameter (92 nm for IZOa). Thus the length-scale requirement for *one-dimensional* WL effect (that is, L_ϕ should be *longer* than the wire diameter or the effective wire width, a) can not be fulfilled. Under this situation, we think that maybe it is more reasonable to apply three-dimensional WL theory on the IZOa in our temperature range of measurement.

Due to the weaker spin-orbit scattering rate and negligible Zeeman splitting in our In:ZnO nanowires, we apply Eq. (5.4) to perform least-squares curve fitting on the MR data of IZOa. Figure 5.5(b) shows the normalized MRs and fitted curves at several temperatures between 8 K and 50 K. For clearer presentation of the data, we move the result of 8 K to the inset of Figure 5.5(b). From this figure, it shows that as temperature goes up, the fitted curves can describe the data better and better. The extracted L_ϕ's are the triangle symbol in the Figure 5.8(a). The L_ϕ at 6 K is 180 nm and the L_ϕ at 10 K is 91 nm. We can find that as temperature below 10 K, the fitted curves coincide the data in relatively smaller range of magnetic field, the resulting L_ϕ's are irrationally high and the length-scale requirement for *three-dimensional*

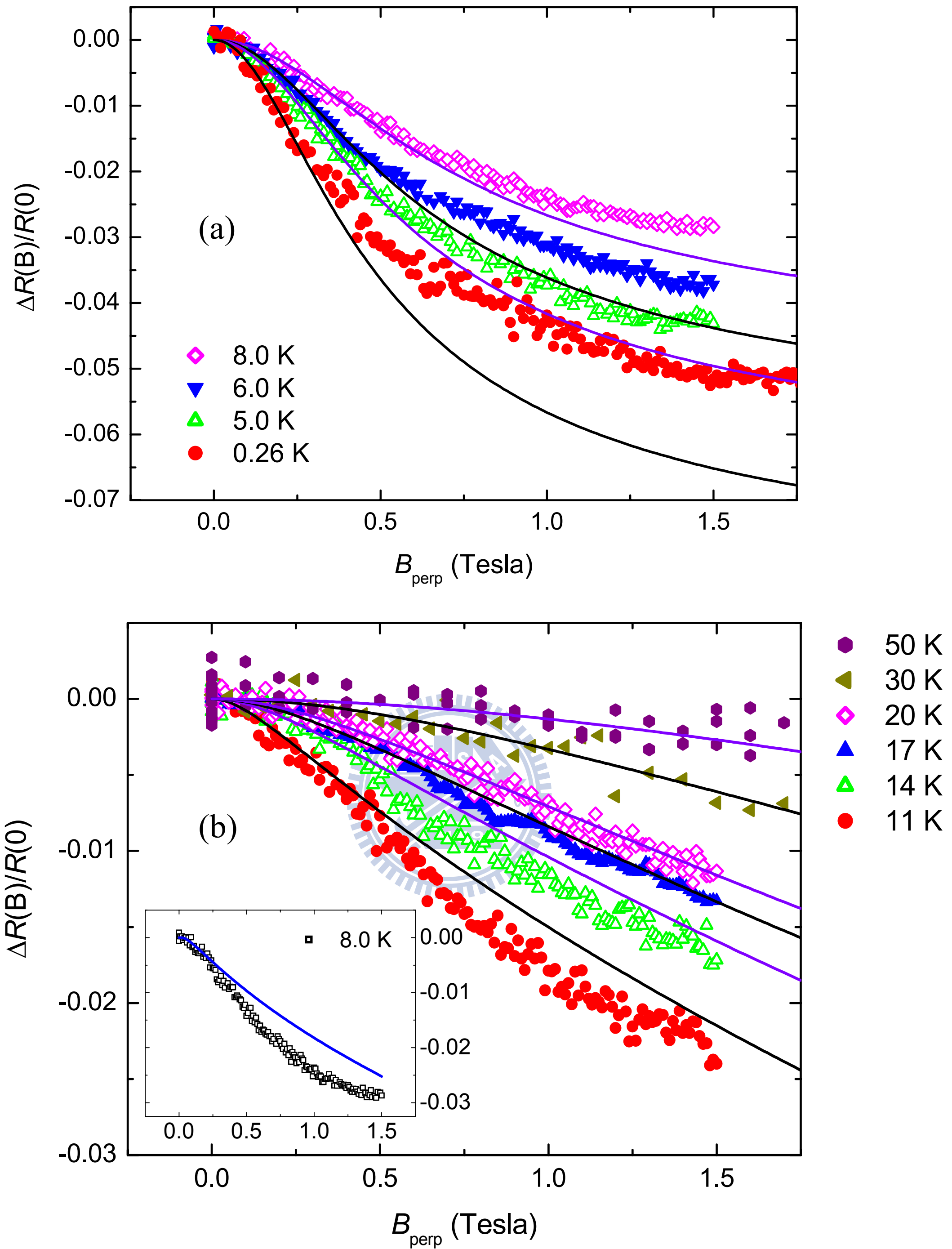

Figure 5.5: For sample IZOa. The symbols are the MR data in the perpendicular magnetic field. (a) The solid curves are the theoretical curves predicted by the 1D WL effect (Eq. (5.1)). (b) The solid curves are the theoretical curves predicted by the 3D WL effect (Eq. (5.4)). For clearer view, the result of 8 K is moved to the inset.

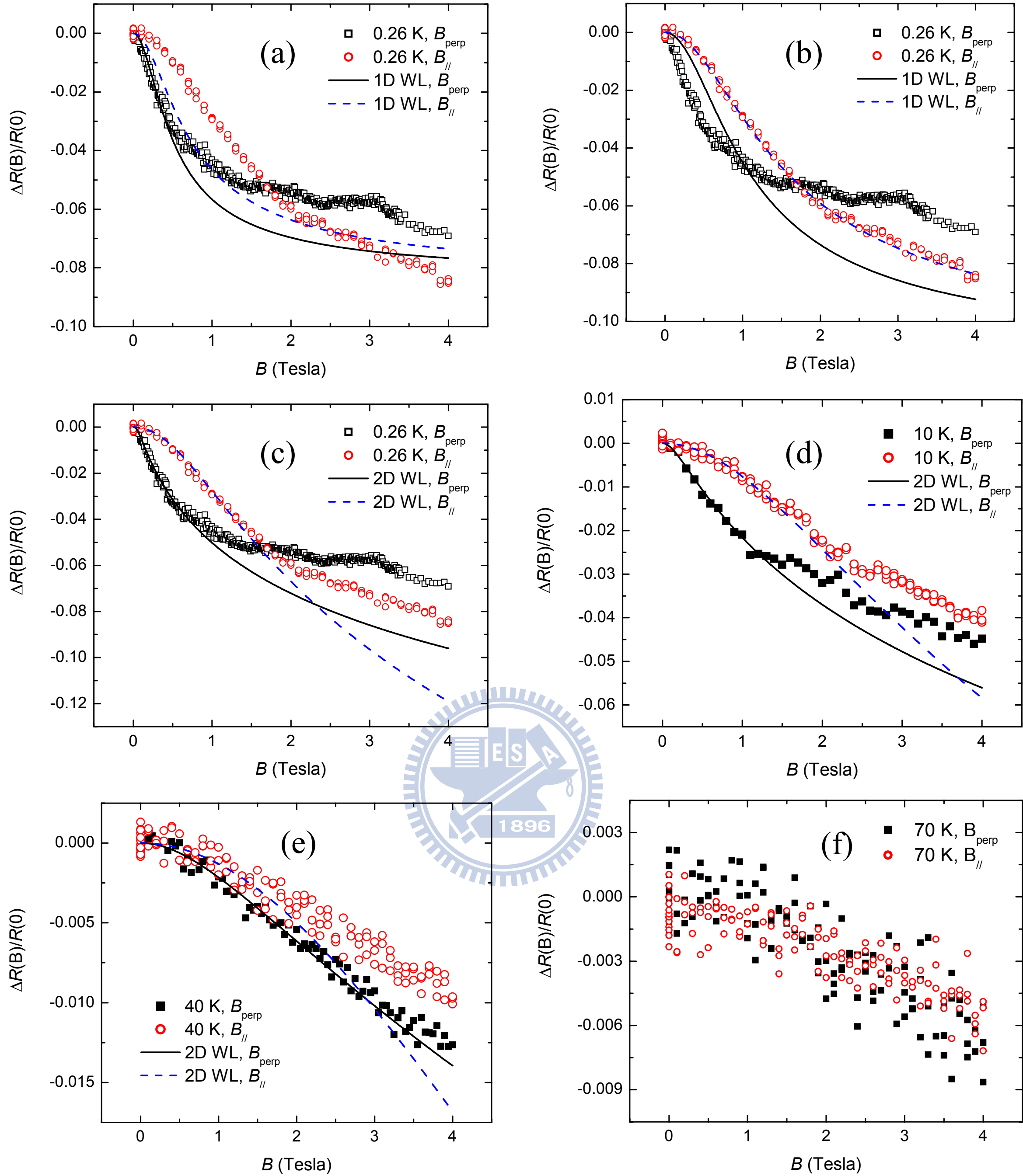

Figure 5.6: For sample IZOa. Figures (a), (b), (c), (d), (e), and (f) correspond to temperatures 0.26 K, 0.26 K, 0.26 K, 10 K, 40 K, and 70 K, respectively. Square symbols are the MRs of perpendicular magnetic field. Circle symbols are the MRs of parallel magnetic field. Solid and dashed curves are the theoretical curves predicted by the WL effects in the perpendicular and parallel magnetic fields, respectively.

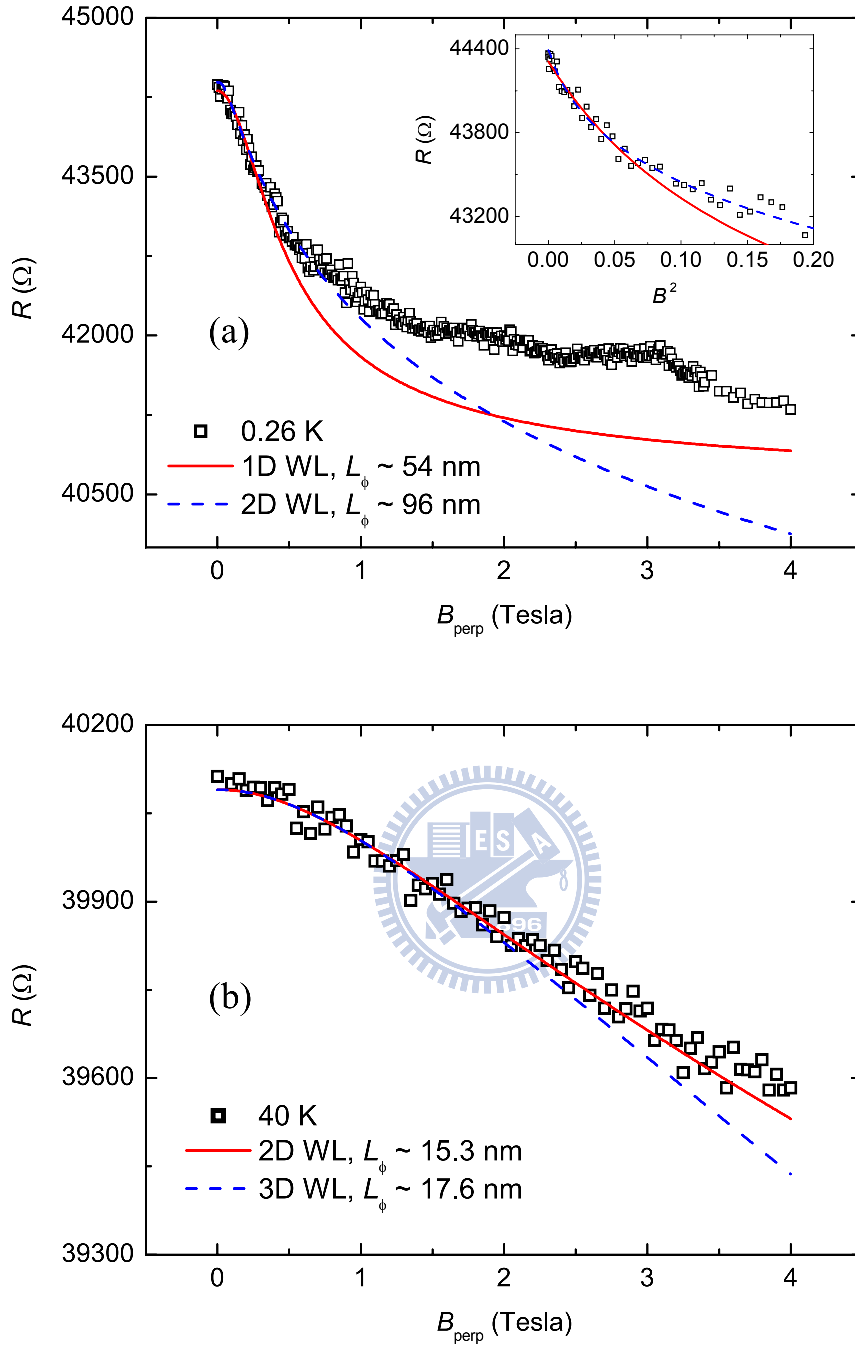

Figure 5.7: For sample IZOa. (a) The symbols are the MR data of 0.26 K. Solid curve is the theoretical curve by Eq. (5.1). Dashed curve is the theoretical curve by Eq. (5.2). Inset is the plot under B^2 x-axis. (b) The symbols are the MR data of 40 K. Solid curve is the theoretical curve by Eq. (5.2). Dashed curve is the theoretical curve by Eq. (5.4).

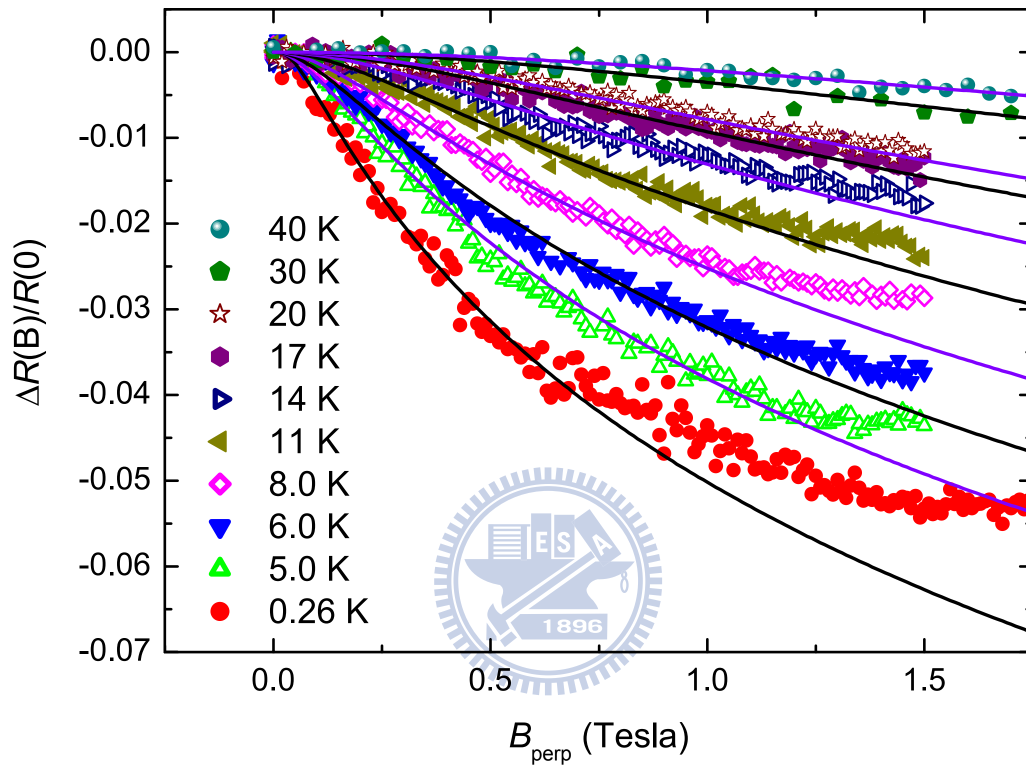

Figure 5.8: For sample IZOa, the symbols are the MR data of perpendicular magnetic field. Solid curves are the theoretical curves predicted by the 2D WL effect (Eq. (5.2)).

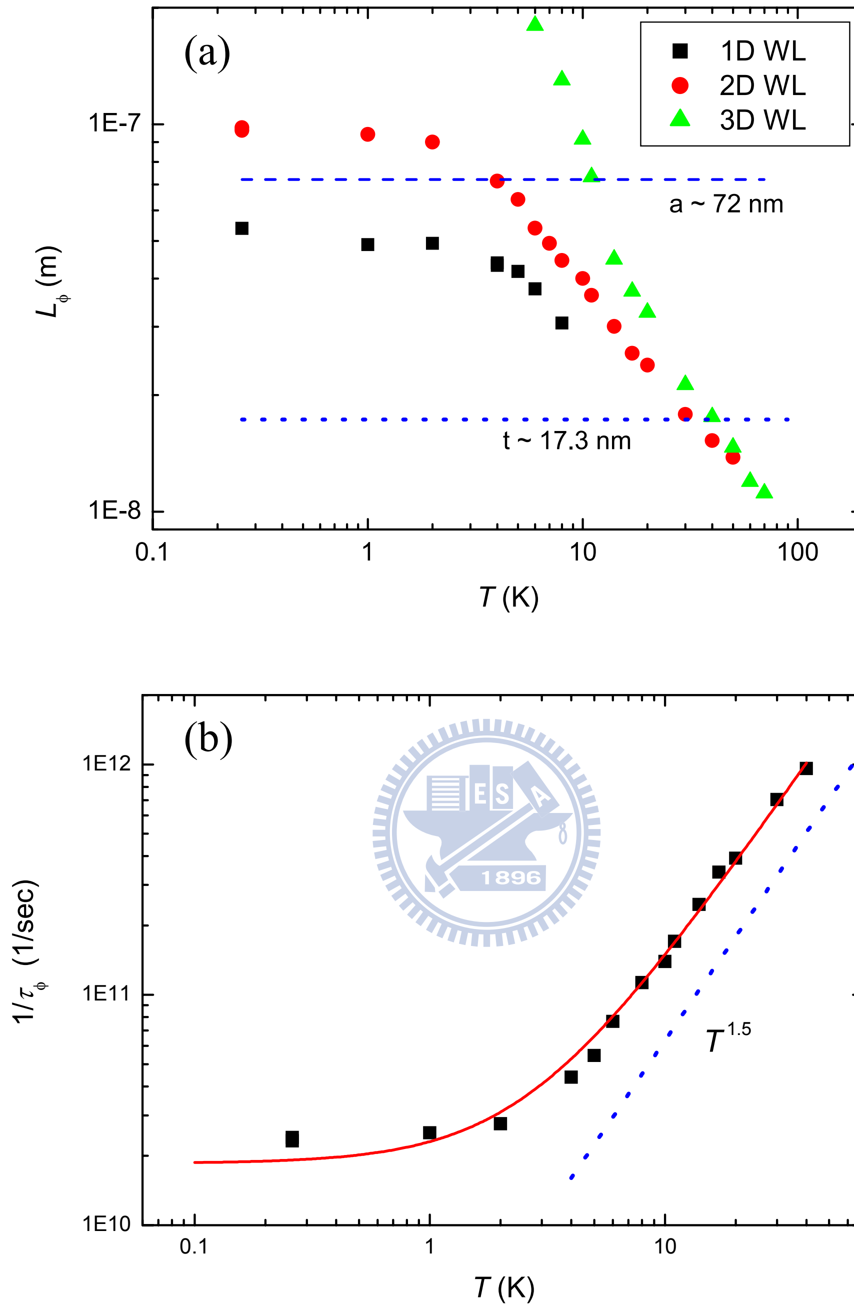

Figure 5.9: For sample IZOa. (a) The extracted phase coherent lengths, L_ϕ's, as a function of temperature. Dashed and dotted lines mark the effective wire width, *a*, and effective film thickness, *t*. (b) Dephasing rates transferred from selected L_ϕ's as a function of temperature. The solid curve is theoretical curve by Eq. (5.8a).

Table 5.2: Parameters from the curve fitting of MRs. L_ϕ is the phase coherent length, L_{so} is the spin-orbit scattering length, *a* is the effective wire width for 1D WL effect in perpendicular magnetic field, *w* is the effective film width for 2D WL effect in perpendicular magnetic field, and *t* is the effective film thickness for 2D WL effect in parallel magnetic field.

Sample	L_ϕ(1 K) (nm)	L_ϕ(10 K) (nm)	L_{so} (nm)	*a* (nm)	*w* (nm)	*t* (nm)
IZOa	94	40	133	72	131	17.3
IZOb	106	44	140	52	127	15.5
PZOe	68	20.5	86	55	160	< 10

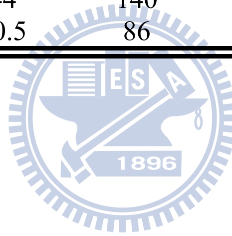

WL effect (that is, L_ϕ should be *shorter* than the wire diameter or the effective wire width, a) is violated. Thus we can expect that at further lower temperatures, the 3D WL theory has no chance to be the suitable candidate to explain the MRs. In this dilemma, the MRs of *parallel* magnetic field gave us a clue to resolve this problem.

In the Figure 5.6, we plot the MRs of perpendicular and parallel magnetic fields together at 0.26 K, 10 K, 40 K, and 70 K. At 70 K (Figure 5.6(f)), the MRs of perpendicular and parallel magnetic fields are almost coincided together. It implies that the phase coherent length, L_ϕ, is short enough to satisfy the length-scale requirement for *three-dimensional* WL effect and thus the direction of magnetic field has few effect in this condition. In the Figure 5.6(a), MR of 0.26 K in the perpendicular magnetic field is least-squares fitted to the Eq. (5.1) with $\tau_B = 3L_B^4 / Da^2$ and the solid curve corresponds to an optimal set of fitting parameters, L_ϕ=54 nm, L_{so}=133 nm, and a=72 nm. We substitute the same set of parameters into the Eq. (5.1) but with $\tau_B = 2L_B^4 / Dr^2$ for the condition of *parallel* magnetic field. Here, a and r are transformed to each other through the relation $a^2 \sim \pi r^2 \sim A$. Then, another dashed curve is generated to simulate the MR in the parallel magnetic field. We find that even in low-field region, the one-dimensional WL theory can not simultaneously well describe the MRs of perpendicular and parallel magnetic fields for the sample IZOa (However, for the sample IZOb, there is a different result. We'll discuss later.). We can reverse the sequence of analysis, that is, to do curve-fitting on the MR of parallel magnetic field first and then generate the theoretical curves of parallel and perpendicular magnetic fields. The result is presented in Figure 5.6(b) and shows similar problem in Figure 5.6(a). The feature that a *cross* of the MRs of parallel and perpendicular magnetic fields happens around 1.75 Tesla is impossible under the framework of *one-dimensional* WL theory. However, if we use *two-dimensional* WL theory, it's possible to describe this phenomenon. In the Figure 5.6(c), the MR of perpendicular magnetic field is least-squares fitted to the Eq. (5.2), the two-dimensional WL theory for the MR in the perpendicular magnetic field. An optimal set of fitting parameters, L_ϕ=96 nm, L_{so}=133 nm, and w=131 nm, is obtained and corresponds to the solid curve in the Figure 5.6(c). We substitute the same set of parameters into Eq. (5.3), the two-dimensional WL theory for the MR in the *parallel* magnetic field, to perform the curve-fitting on the MR of *parallel* magnetic field. There is an additional fitting parameter in Eq. (5.3), the effective film thickness, t. t=17.3 nm is the optimal value and corresponds to the dashed curve in the Figure 5.6(c). Under the framework of *two-dimensional* WL theory, we find that in the low-field region, both the MRs of parallel and perpendicular magnetic fields could be well

described. Similar results of 10 K and 40 K are also showed in Figure 5.6 (d) and (e).

In the Figure 5.7(a), the low-field data (0 to 0.25 Tesla) is utilized to perform curve fitting with 1D and 2D WL theories and theoretical curves are generated up to 4 Tesla (solid curve for 1D WL; dashed curve for 2D WL). In relatively low field region, both theoretical curves have a similar asymptote form, $\Delta R \sim B^2$, (as shown in the inset of Figure 5.7(a)) and then turn to another asymptote form, $\Delta R \sim B^{1/2}$ in the high field region. However, the WL theories of different dimensionalities give different behaviors which govern how the MR curves transfer from B^2 form to $B^{1/2}$ form. In the case of Figure 5.7(a), obviously, 2D WL theory is more suitable than 1D WL theory. In the Figure 5.7(b), both the 2D and 3D WL theories can well describe the MR of 40 K and similar values of L_ϕ (L_ϕ=15.3 nm for 2D WL and L_ϕ=17.6 nm for 3D WL) are extracted. It's indicated that the 2D-3D dimensional crossover for the weak localization effect happens around this temperature (40 K). As temperature rises to 70 K, the transition of 2D-to-3D WL effect is almost finished and MRs reveal tiny anisotropy in different orientations of magnetic field (Figure 5.6(f)).

For IZOa, we have performed the least-squares curve fitting on the MR data of perpendicular magnetic field under the framework of two-dimensional WL theory (Eq. (5.2)). The relative fitting parameters (L_ϕ, L_{so}, and w) are listed in the Table 5.2. In the Figure 5.8, the symbols are experimental data and the curve-fitting results are plotted as solid curves. We can find that at almost all of our measurement temperatures, the normalized MRs could be well described by the theoretical curves. The L_ϕ's between 0.26K and 50 K are extracted and plotted as the circle symbols in the Figure 5.9(a). As the temperature decreases from 70 K to 0.26 K, L_ϕ increases from 11 nm to 96 nm. The L_ϕ of IZOa possesses a low temperature saturation which starts around 3 K. This behavior is similar to the resistivity at low temperatures. At 40 K, the L_ϕ's of 2D WL effect (circle symbols) and the L_ϕ's of 3D WL effect (triangle symbols) are starting to coincide together, revealing the 2D-3D dimensional crossover of the WL effect. Before quantitatively analyzing the temperature behavior of L_ϕ in IZOa, we would like to extract the L_ϕ's in IZOb first, and then we'll discuss the temperature behaviors of L_ϕ's in IZOa and IZOb together in the next section.

To extract the L_ϕ's of IZOb, we perform the similar analysis, i.e., the MRs of perpendicular magnetic field are least-squares fitted to the WL theories of different dimensionalities (Eq. (5.1), Eq. (5.2), and Eq. (5.4)). The related fitting parameters (L_ϕ, L_{so}, a, and w) are listed in the Table 5.2. The curve-fitting results are presented in the Figure 5.10. The Figure 5.10(a), (b), and (c) correspond to the analyses with the 1D, 3D, and 2D WL

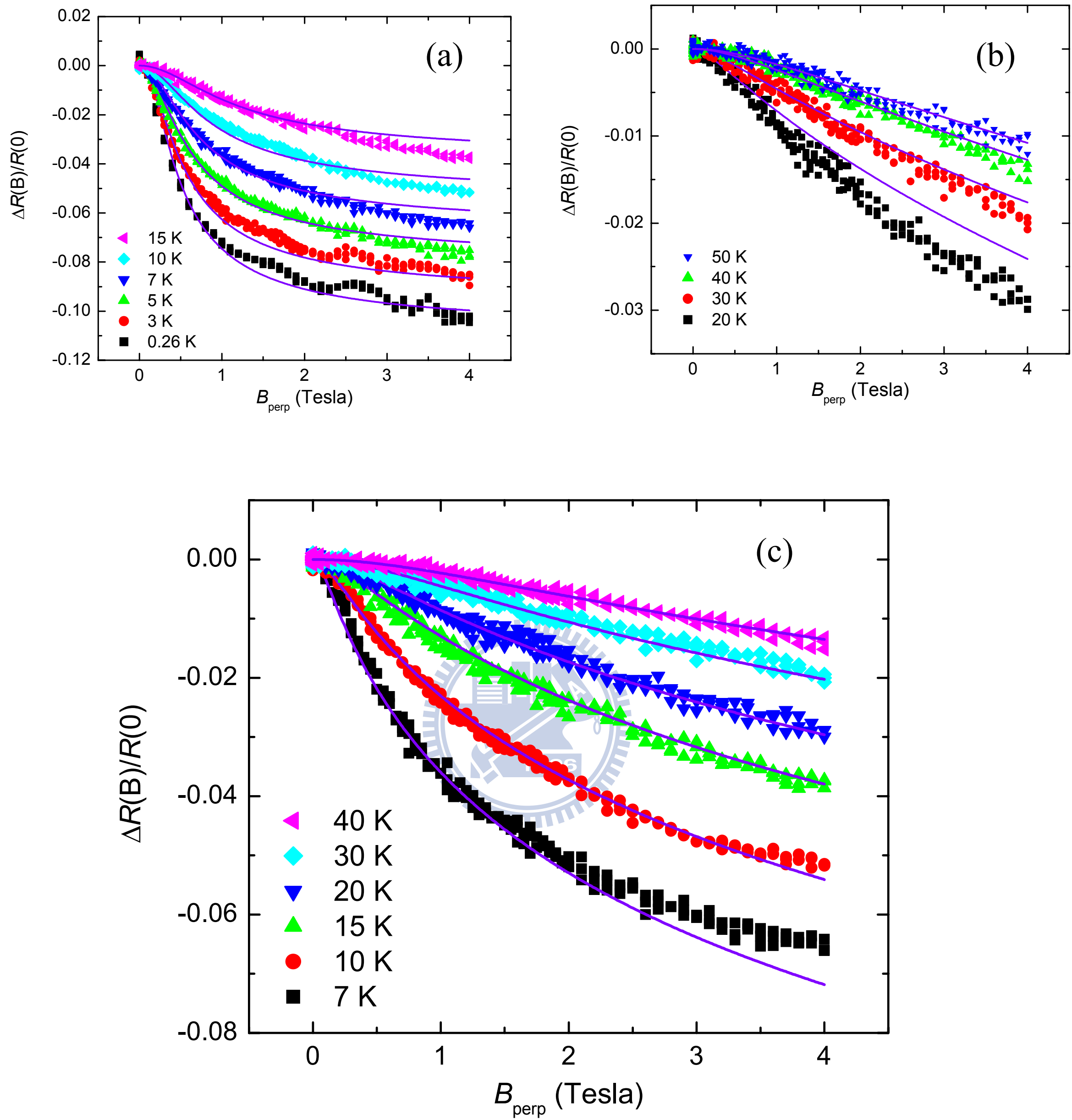

Figure 5.10: For sample IZOb. The symbols are the MR data in the perpendicular magnetic field. (a) The solid curves are the theoretical curves predicted by the 1D WL effect (Eq. (5.1)). (b) The solid curves are the theoretical curves predicted by the 3D WL effect (Eq. (5.4)). (c) Solid curves are the theoretical curves predicted by the 2D WL effect (Eq. (5.2)).

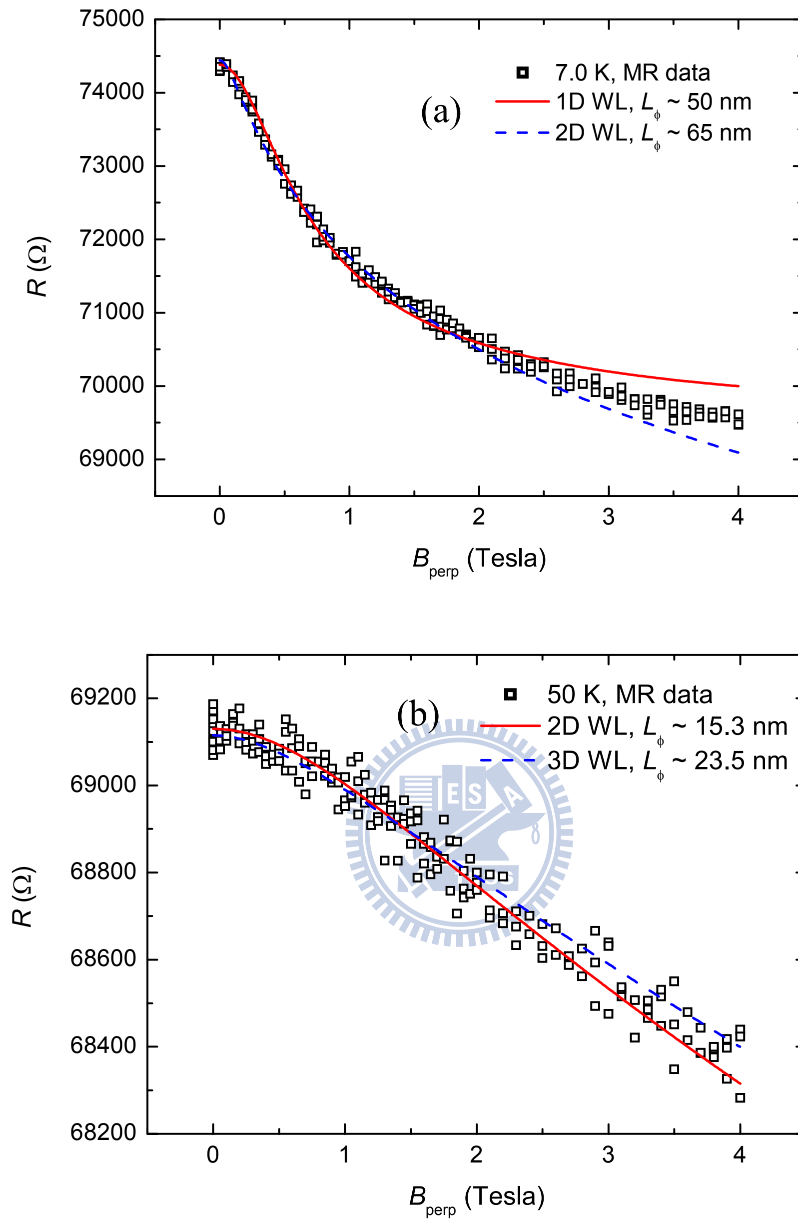

Figure 5.11: For sample IZOb. (a) The symbols are the MR data of 7 K. Solid curve is the theoretical curve by Eq. (5.1). Dashed curve is the theoretical curve by Eq. (5.2). (b) The symbols are the MR data of 50 K. Solid curve is the theoretical curve by Eq. (5.2). Dashed curve is the theoretical curve by Eq. (5.4).

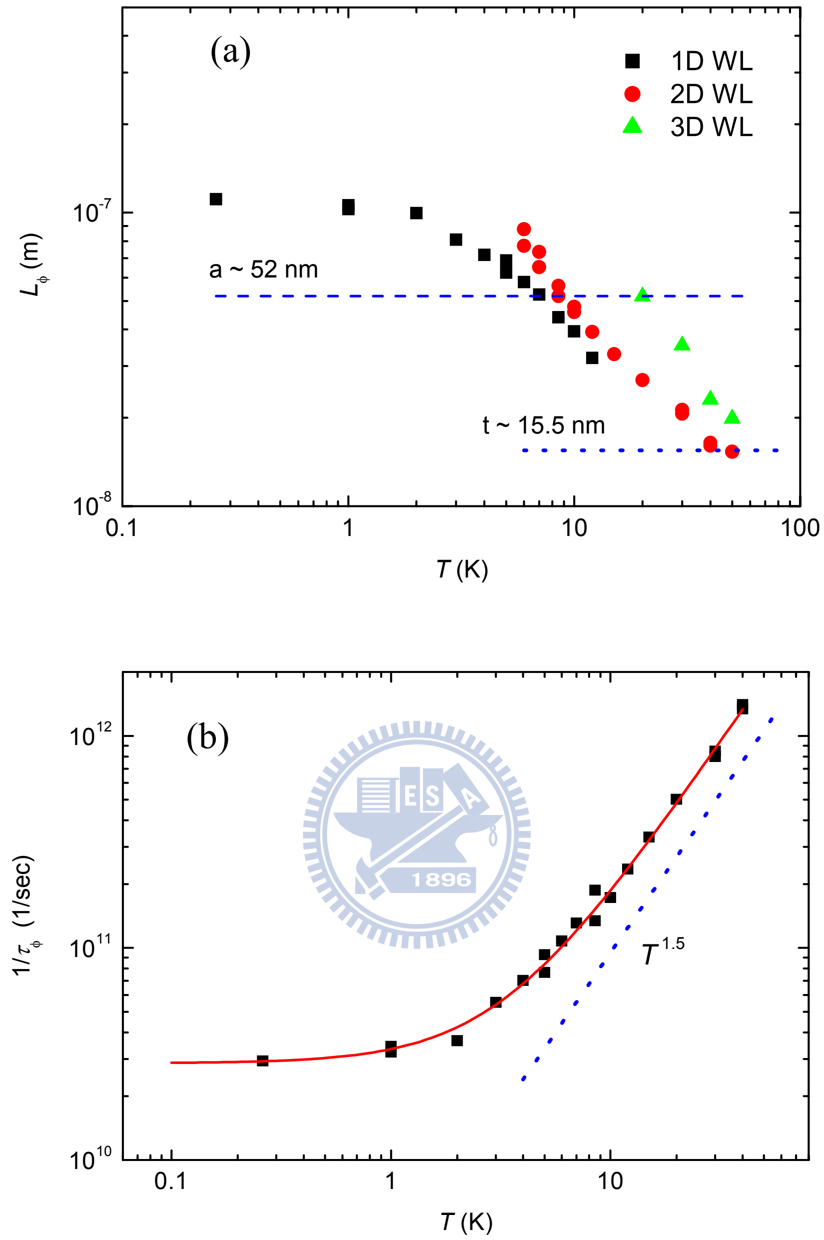

Figure 5.12: For sample IZOb. (a) The extracted phase coherent lengths, L_ϕ's, as a function of temperature. Dashed and dotted lines mark the effective wire width, *a*, and effective film thickness, *t*. (b) Dephasing rates transferred from selected L_ϕ's as a function of temperature. The solid curve is theoretical curve by Eq. (5.8a).

theories, respectively. In these figures, we find that the WL theories of different dimensionalities present different applicable temperature ranges for this sample. It can be roughly defined as that, 1D WL theory is applicable between 0.26 K and 10 K, 2D WL theory is applicable between 7 K and 50 K, and above 40 K, 3D WL theory is applicable. At temperatures of dimensional crossover for the WL effect, e.g. 7 K and 50 K (Figure 5.11(a) and (b), respectively), the theoretical curves of WL effects with different dimensionalities are plotted together. At 7 K, both 1D and 2D WL theories can well describe the data in the magnetic field range below 1 Tesla and the extracted L_ϕ's are around 50 nm. At 50 K, both 2D and 3D WL theories can well describe the data in the magnetic field range below 1.5 Tesla and the extracted L_ϕ's are around 15 nm. It implies that the 1D-2D dimensional crossover and 2D-3D dimensional crossover of WL effect happen around 7 K and 50 K respectively. Figure 5.12(a) shows the extracted L_ϕ's corresponding to the WL effects of different dimensionalities. It indicates that L_ϕ increases from 15 nm to 111 nm as the temperature decreases from 50 K to 0.26 K. Similar to the IZOa, there is a saturation of L_ϕ starting around 2 K. In the temperature region of dimensional crossover of WL effect, the values of L_ϕ due to the WL effects of different dimensionalities are approaching to each other. The L_ϕ reveals the whole process of 1D-2D dimensional crossover of WL effect around 8.5 K, and implies the onset of 2D-3D dimensional crossover of WL effect at 50 K. (Recalling IZOa, we can see the whole process of 2D-3D dimensional crossover of WL effect around 50 K.) The effective wire width, a, for quasi-1D structure is extracted to be 52 nm and is plotted as a dashed horizontal line lying across the temperature region of 1D-2D dimensional crossover of WL effect in the Figure 5.12(a). Thus this length scale can act as a characteristic length for the 1D-2D dimensional crossover of WL effect. If the L_ϕ is enough longer than a, the sample shows pure 1D WL effect, while if the L_ϕ is shorter than a and in some suitable range, i.e. $t < L_\phi < w$, the sample shows 2D WL effect.

5.3.3 *Dephasing rate*

Utilizing the relation $L_\phi = \sqrt{D\tau_\phi}$, the dephasing rate τ_ϕ^{-1} can be obtained from coherent length, L_ϕ. Figure 5.9(b) and Figure 5.12(b) show the τ_ϕ^{-1} as a function of temperature for IZOa and IZOb, respectively. The τ_ϕ^{-1}'s of IZOa are evaluated from the L_ϕ's of 2D WL effect between 0.26 K and 40 K. The τ_ϕ^{-1}'s of IZOb are evaluated from the L_ϕ's of 1D WL effect between 0.26 K and 8.5 K and the L_ϕ's of 2D WL effect between 8.5 K and 40 K. In a weakly

disordered conductor, the electron dephasing rate is given by [8]

$$\frac{1}{\tau_\phi(T)} = \frac{1}{\tau_0} + \frac{1}{\tau_{ee}(T)} + \frac{1}{\tau_{ep}(T)} = \frac{1}{\tau_0} + A_{ee}T^n + A_{ep}T^p \tag{5.8}$$

$$\frac{1}{\tau_\phi(T)} = \frac{1}{\tau_0} + \frac{1}{\tau_{ee}(T)} + \frac{1}{\tau_{ep}(T)} = \frac{1}{\tau_0} + AT^p \tag{5.8a}$$

where τ_0 is a constant, whose origins are a subject of elaborate investigations [99][110]. The electron-electron (e-e) scattering rate, τ_{ee}^{-1}, in low dimensional disordered conductors is known to dominate τ_ϕ^{-1} in a sufficiently wide temperature interval [8]. We use the standard expression: $\tau_{ee}^{-1}=A_{ee}T^n$, where n=2/3 and 1 for e-e scattering involving small energy transfer in the one- and two-dimensional samples respectively [99][101], and n=3/2 for e-e scattering involving large energy transfer in the three-dimensional samples. The electron-phonon (e-ph) scattering rate, τ_{ep}^{-1}, will become more important at high measurement temperatures. We express τ_{ep}^{-1} in a general form, $\tau_{ep}^{-1}=A_{ep}T^p$, where the value of exponent p depends on several mechanisms, such as the type of defects [111][112], the dimensionality of electronic system [105], phonon dimensionality [113]-[116], and so on. In the three-dimensional disordered conductors, the cases of p=2 were frequently encountered [8]. As shown in the Figure 5.9(b) and Figure 5.12(b), τ_ϕ^{-1}'s are well fitted by Eq. (5.8) with four adjustable parameters, τ_0, A_{ee}, A_{ep}, and p. It's worthy to note that either setting n=2/3 or n=1, the extracted values of A_{ee} are always negligible small. If considering n=3/2 for e-e scattering with large energy transfer, the second and third terms of Eq. (5.8) will possess similar temperature exponents (~1.5) and then the Eq. (5.8) will collapse to two terms as the Eq. (5.8a). There is the probability that the τ_{ee}^{-1} and τ_{ep}^{-1} have similar temperature behavior. Thus the reliable physical information which can be revealed from our dephasing rate would be τ_0^{-1} , A and p. We list the τ_0, A, and p in the Table 5.3. Both of IZOa and IZOb possess similar p value (p~1.5) and their τ_ϕ^{-1} obey the temperature dependence of $\tau_\phi^{-1}\sim T^{1.5}$ up to 40 K. The $T^{1.5}$-law is expected in the three-dimensional electron-electron scattering with large energy transfer [39][101], which is characterized by thermal diffusion length, L_T. However the $T^{1.5}$-law in our samples persists to the rather high temperature, such that it can not be contributed only by electron-electron scattering. Another mechanism responsible for the $T^{1.5}$-law might be the effect of reducing phonon dimensionality [113]-[116]. The observation of p~1.4 in the thin Sb films [113]] is in

Table 5.3. Parameters from the curve fitting. τ_0, A, and p are the parameters related to the dephasing rate τ_ϕ^{-1} in Eq. (5.8a). $\tilde{F}$ is the coupling constant of Hartree processes defined in Eq. (5.5).

Sample	τ_0 (ps)	A (K^{-p} s^{-1})	p	$\tilde{F}$
IZOa	53.9	4.5×10^9	1.41 +/- 0.05	0.42
IZOb	35	4.77×10^9	1.45 +/- 0.07	0.51, 0.61
PZOe	54.5	2.77×10^{10}	1.23 +/- 0.03	0.75

line with the result (p~2.4) of thick Sb films [114], if the thermal phonons are effectively two dimensional in thin films but three dimensional in thick films. The thin copper wires [116] evaporated on suspended silicon nitride membranes with thickness ranging from 30 to 750 nm were observed the onset of the effects of two-dimensional (2D) phonon system which changes the temperature dependence of electron-phonon scattering rate (reducing p from 6,7 [105] to 4.5, or 5.). Now we should go back to a basic question that why we can observe *two-dimensional* WL effect in our In:ZnO nanowires devices in order to proceed further discussion about the phonon dimensionality and e-ph scattering rate.

5.3.4 *Inner structure of nanowires*

In the section 5.3.2, we have discussed the MRs of parallel and perpendicular magnetic fields, introduced 2D WL effect to explain the data in the Figure 5.6, and extracted a thickness parameter, t. In the Figure 5.13(a), we perform least-squares curve fitting on the normalized MRs of parallel magnetic field to extract t at different temperatures. The experimental data (symbols) of sample IZOa is well described by the theoretical curves based on Eq. (5.3). The extracted t's are plotted in the Figure 5.13(b) as a function of temperature. According the previous analysis, we have known that IZOa possesses a 2D-3D dimensional crossover of WL effect around 40 K. Thus we avoid the t's covered by the crossover and then have an averaged t=17.3 nm. This value of t is consistent with the 2D-3D dimensional crossover of WL effect around 40 K. At 40 K, the extracted L_ϕ's are 15.3 nm from 2D WL theory and 17.3 nm from 3D WL effect (Figure 5.7(b)). Therefore as temperature rising from 40 K, L_ϕ will be smaller than t gradually and the transition of 2D to 3D WL effects happens. In the inset of Figure 5.13(b), there is a suggested scheme of inner structure of nanowires, called core-shell-like structure. The t is the effective film thickness of the shell and it also corresponds to the parameter t of the 2D WL theory in the parallel magnetic field. As we know, ZnO is a promising material for gas sensing because when the surface-volume ratio is high enough, the electrical properties are easily affected by ambient gases. The mechanism is believed to be related to the states of surface dangling bonds and the surface defects, e.g. oxygen vacancies. Therefore we suggest a core-shell-like structure to incorporate with the 2D WL effect. There are two scenarios about the core-shell-like structure. First, the core is almost no contribution for electrical conduction like an insulator, such that all of the electrical transport properties are originated from the shell. Second, the core is a conductor with good lattice arrangement, i.e., few disorderness, but the shell is more disordered than the core. Both of them contribute to

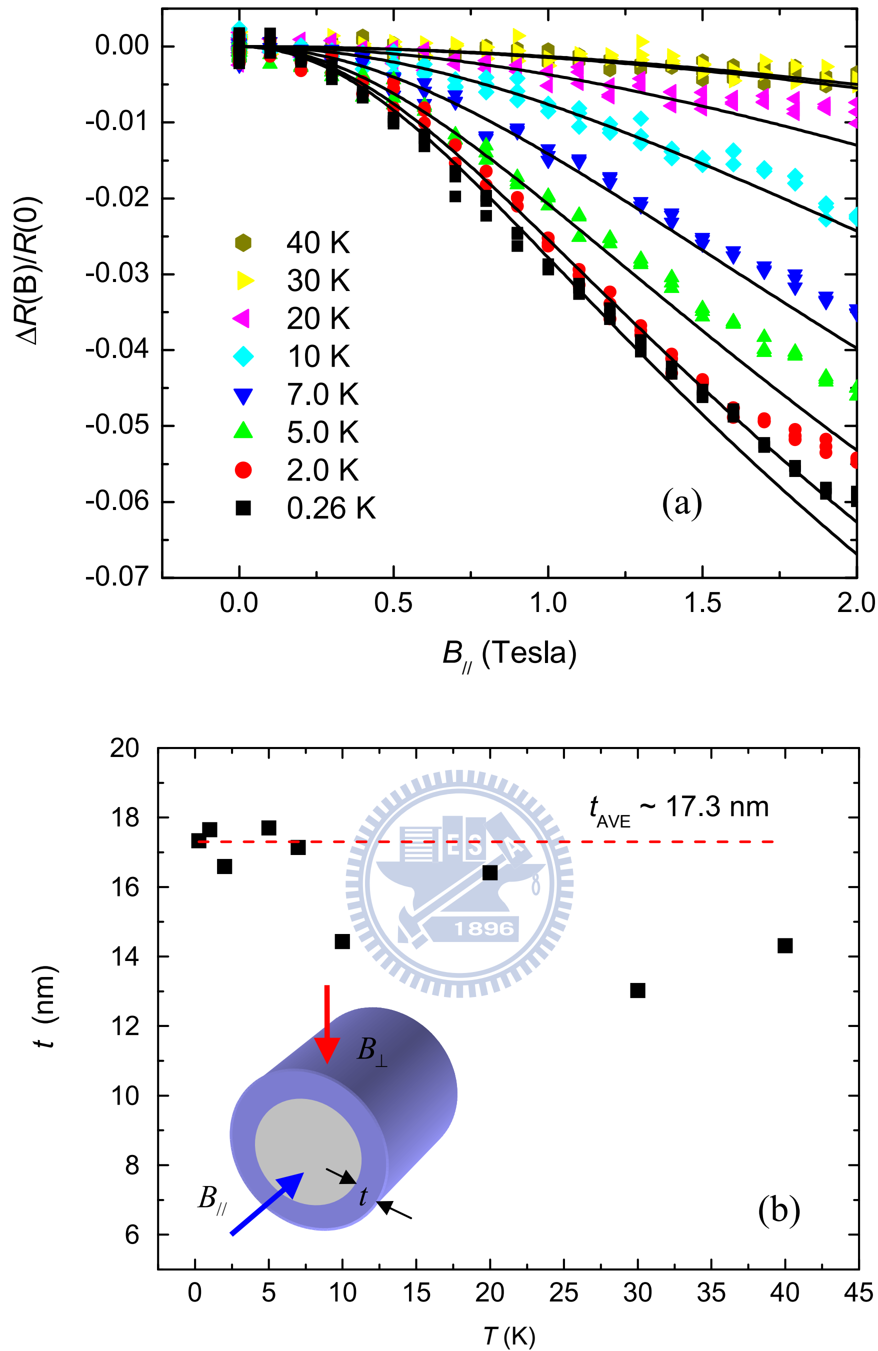

Figure 5.13: For sample IZOa. (a) The symbols are the MR data in the parallel magnetic field. The solid curves are the theoretical curves predicted by the 2D WL effect (Eq. (5.3)). (b) The extracted effective film thicknesses as a function of temperature. The average value is 17.3 nm. The inset is a scheme of core-shell-like structure inside the nanowires.

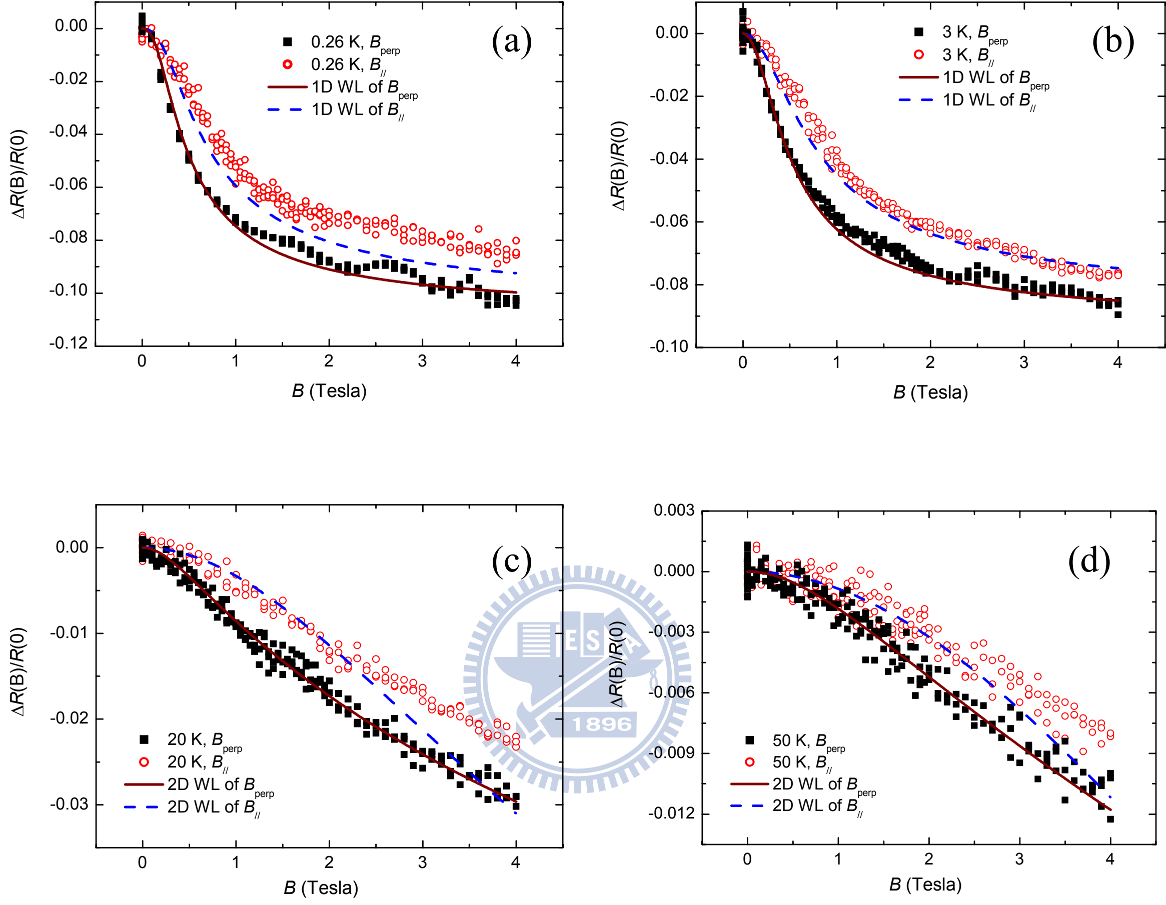

Figure 5.14: For sample IZOb. Figures (a), (b), (c), and (d) correspond to temperatures 0.26 K, 3.0 K, 20 K, and 50 K, respectively. Square symbols are the MRs of perpendicular magnetic field. Circle symbols are the MRs of parallel magnetic field. Solid and dashed curves are the theoretical curves predicted by the WL effects in the parallel and perpendicular magnetic fields, respectively.

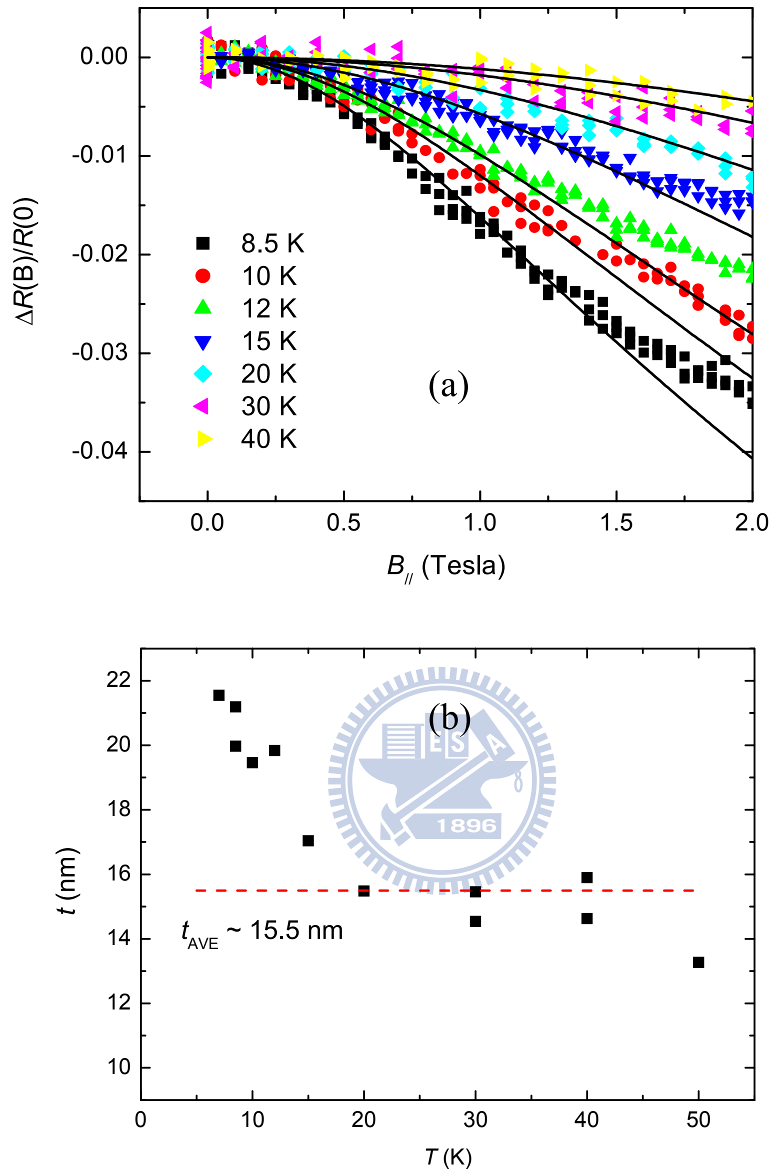

Figure 5.15: For sample IZOb. (a) The symbols are the MR data in the parallel magnetic field. The solid curves are the theoretical curves predicted by the 2D WL effect (Eq. (5.3)). (b) The extracted effective film thicknesses as a function of temperature. The average value is 15.5 nm.

the electrical conduction, however the most effect of disorder-induced quantum corrections, e.g. WL effect and electron-electron interaction, still comes from the shell. In our opinion, the second scenario is more realistic.

Whatever the scenario we choose, the core-shell-like structure acts as a cylindrical conductor. The cylindrical conductor in the field parallel to its axis has an oscillation signature [107] of MR, known as the Altshuler-Aronov-Spivak (AAS) effect [109]. In our MR data, there is no obvious oscillation sited on the based curves resulted from WL effects. However it's reasonable for the *thick* shell structures. We can imagine the thick shell is composed of many thin concentric shells with different radii r's. Each thin shell can generate an AAS oscillation of magnetic–field period of $\Delta B=(h/2e)/\pi r^2$. If we use the r of outmost shell (r = 46 nm), ΔB is about 0.16 Tesla. If we use a shortest r = 46 - 17 = 29 nm, ΔB is about 0.4 Tesla. Because of many different magnetic–field periods, the oscillation is averaged out. The extreme condition is that when the shell thickness approaching to the radius of the wire, the core-shell structure collapses to a simple rod and the AAS oscillation is removed totally.

For sample IZOb, we also have finished the analysis of MRs of parallel magnetic field (Figure 5.15(a)) and plotted the extracted shell thickness t in the Figure 5.15(b). The averaged value of t is 15.5 nm. This value is also consistent with the L_ϕ at 50 K (Figure 5.11(b)) and marks the occurrence of 2D-3D dimensional crossover of WL effect. We plot the t's as the horizontal dotted lines in the Figure 5.9(a) and Figure 5.12(a) to be the characteristic lengths for 2D-3D dimensional crossover of WL effect. Recalling the MRs of IZOa, we know that even at lowest temperature, the 1D WL theory can not well describe the MRs of parallel and perpendicular magnetic fields. In the IZOb, there is a little difference. In the Figure 5.14, normalized MRs of parallel and perpendicular magnetic fields and the theoretical curves are displayed. At 0.26 K and 3.0 K, the 1D WL theory can well describe the experimental data. At 20 K and 50 K, the 2D WL theory can well explain the experimental data. Why IZOb can reveals 1D WL effect at lowest temperature, but IZOa can not? Comparing their effective wire widths, a, for quasi-1D structures (a=72 nm for IZOa, a=52 nm for IZOb), the L_ϕ is easier to exceed the shorter a in the IZOb and result in 1D WL effect. It's worthy to mention that the effective wire width a characterizes the effective cross section area ($\sim a^2$) for the quantum interference effect, and thus a^2 should be a similar order of magnitude as the cross section area of the shell. We can calculate as follows. For IZOa, the cross section area of the shell would roughly be ($\pi \times dia. \times t$) ~ $\pi \times$ 92 nm $\times$ 17.3 nm ~ (70.7 nm)^2. For IZOb, the cross section area of the shell is roughly ~ $\pi \times$ 68 nm $\times$ 15.5 nm ~ (57.5 nm)^2. The results

are well agreed to the value of a's in both samples. Therefore the core-shell-like structure and the dimensional crossovers of WL effect resulted from this structure can be well incorporated to explain our experimental MR data. For the nanowires with sufficiently small diameters, the core-shell-like structure will collapse to a simple rod structure such that quantum interference effects show pure one-dimensional prosperities in wide range of temperature [11].

The exponent p of $L_\phi(T)$ in our samples is about 1.5. We mentioned before that it maybe results from the reducing of phonon dimensionality. The phonon wavelength is $\lambda_T=2\pi/q$, where $q = k_B T / \hbar u$ is the wavenumber of thermal phonon, u is the sound velocity. New technique of electron diffraction showed that in ZnO nanowires the speed of sound along the c axis is 6200 m/s [117]. The estimated value of λ_T at 10 K is around 30 nm which exceeds the shell thicknesses. So, it's possible to have confinement effect for the phonons. However, the properties of the boundary between core and shell are unclear, so that the confinement effect still needs more investigation to verify.

5.3.5 *Dimensional crossover of electron-electron interaction*

In this section, we'll discuss how the core-shell-like structure inside In:ZnO nanowires affects the temperature behavior of low-temperature resistivity governed by electron-electron (e-e) interaction. The e-e interaction in three-dimensional disordered metals often dominate the low-temperature behavior of the resistivity. However, in the low dimensional systems, both WL effect and e-e interaction have comparable contribution to the low-temperature resistivity. Therefore if we want to investigate the temperature behavior resulting from e-e interaction, it's usually to apply a sufficiently high magnetic field to remove WL effect and then measure the resistivities at different temperatures. Because the characteristic magnetic field which can affect the e-e interaction is in the order of $\hbar / 4eD\tau$, for the diffusive systems with relatively short mean free time, τ, this characteristic magnetic field would be a huge field (several tens Tesla in our samples). It means that the e-e interaction will maintain in a moderate high magnetic field, but WL effect won't. Thus we measured the resistivities at temperatures between 0.26 K and 40 K in two conditions, that is, without magnetic field and with 4-Tesla magnetic field perpendicular to the wire axes. In the Figure 5.16(a), the resistivities of IZOa are plotted versus $T^{1/2}$ scale in the x-axis. Obviously, 0-Tesla curve and 4-Tesla data possess different temperature behaviors. The 4-Tesla data shows a linear region between 5 K and 40 K. The $T^{1/2}$ behavior manifests that the e-e interaction is three dimensional. We utilize Eq. (5.7) with dimensionality d=3 to extract the coupling constant of

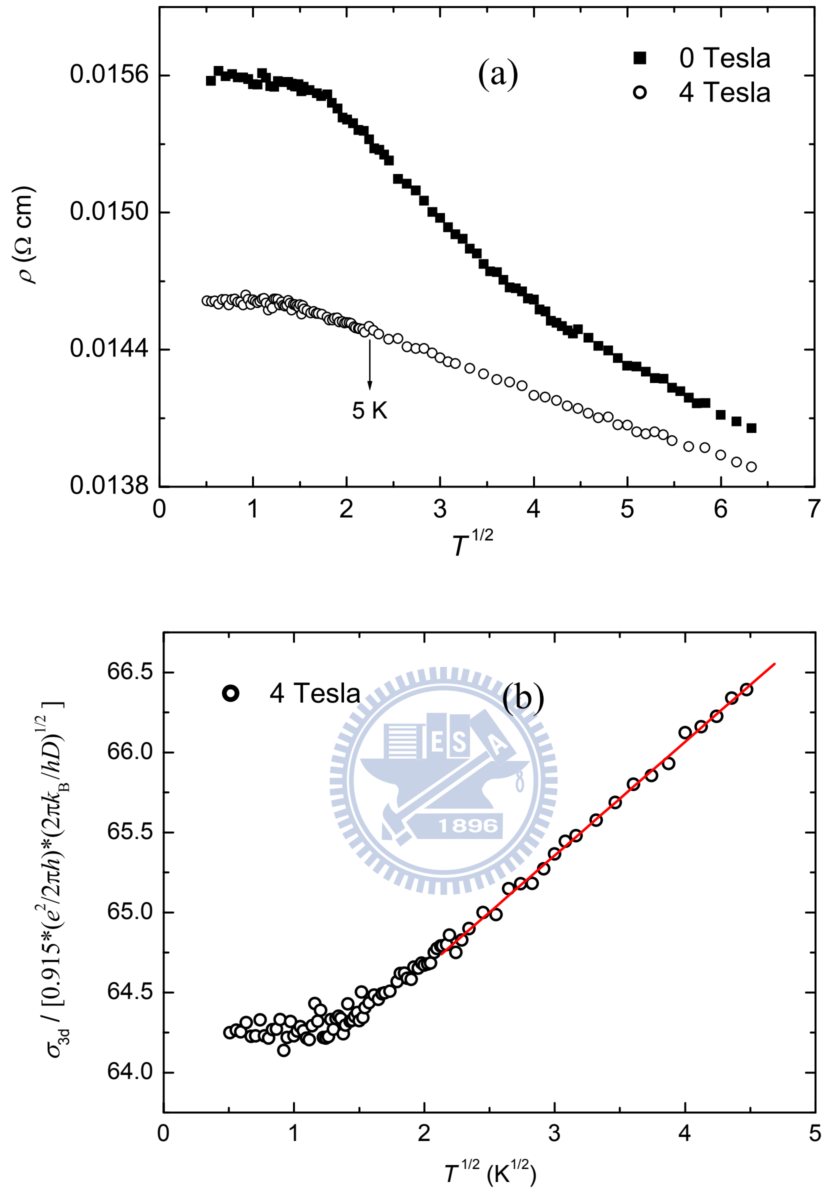

Figure 5.16: For sample IZOa. (a) The resistivities as functions of temperature in the 0-Tesla and 4-Tesla magnetic fields are plotted with $T^{1/2}$ x-axis. (b) The modified conductivities based on the Eq. (5.7) are plotted with $T^{1/2}$ x-axis.

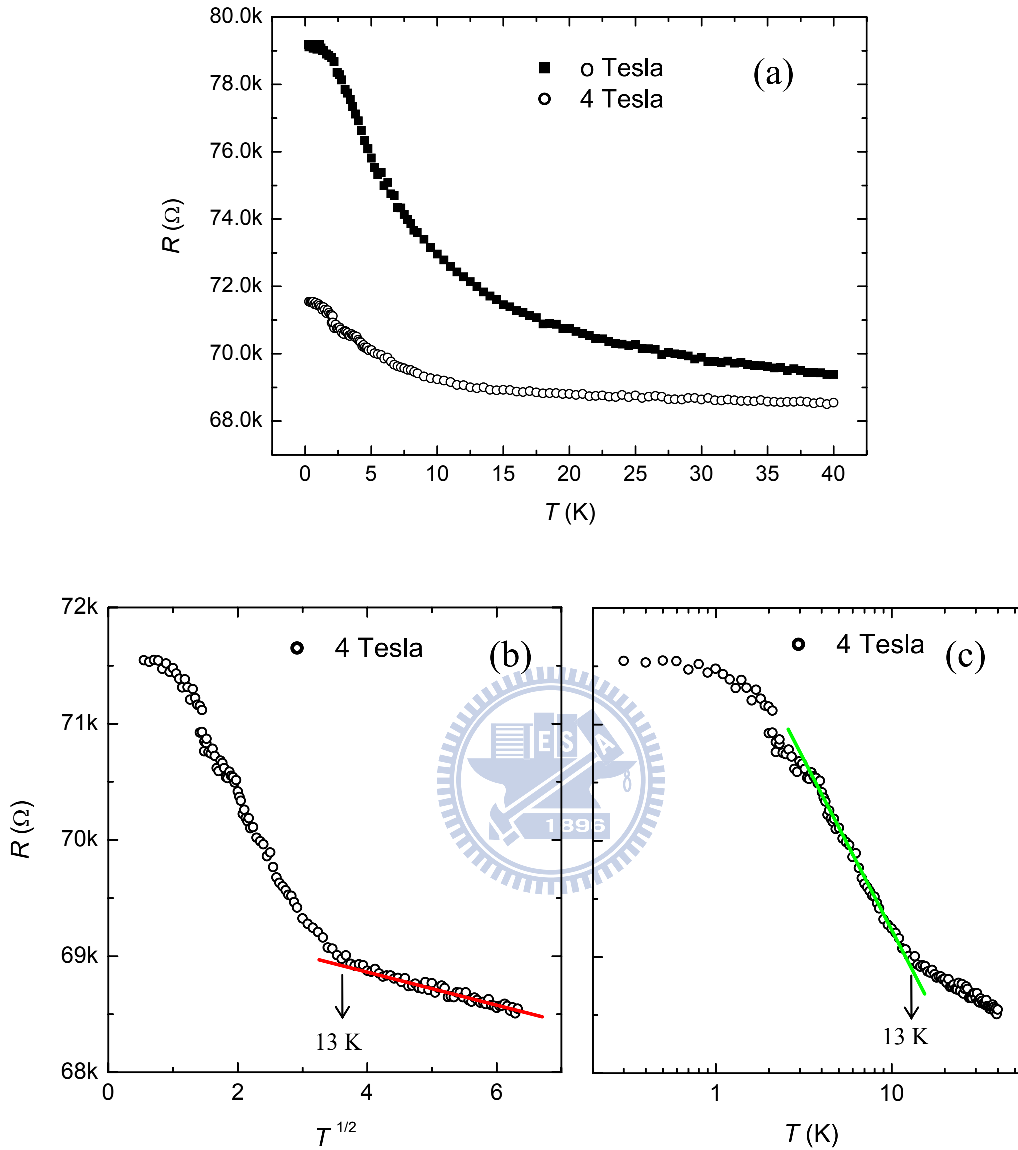

Figure 5.17: For sample IZOb. (a) The resistivities as functions of temperature in the 0-Tesla and 4-Tesla magnetic fields. (b) The resistivities in the 4-Tesla magnetic field are plotted with $T^{1/2}$ x-axis. Solid curve is the theoretical curve predicted by Eq. (5.7). (c) The resistivities in the 4-Tesla magnetic field are plotted with logarithmic x-axis. Solid curve is the theoretical curve predicted by Eq. (5.7).

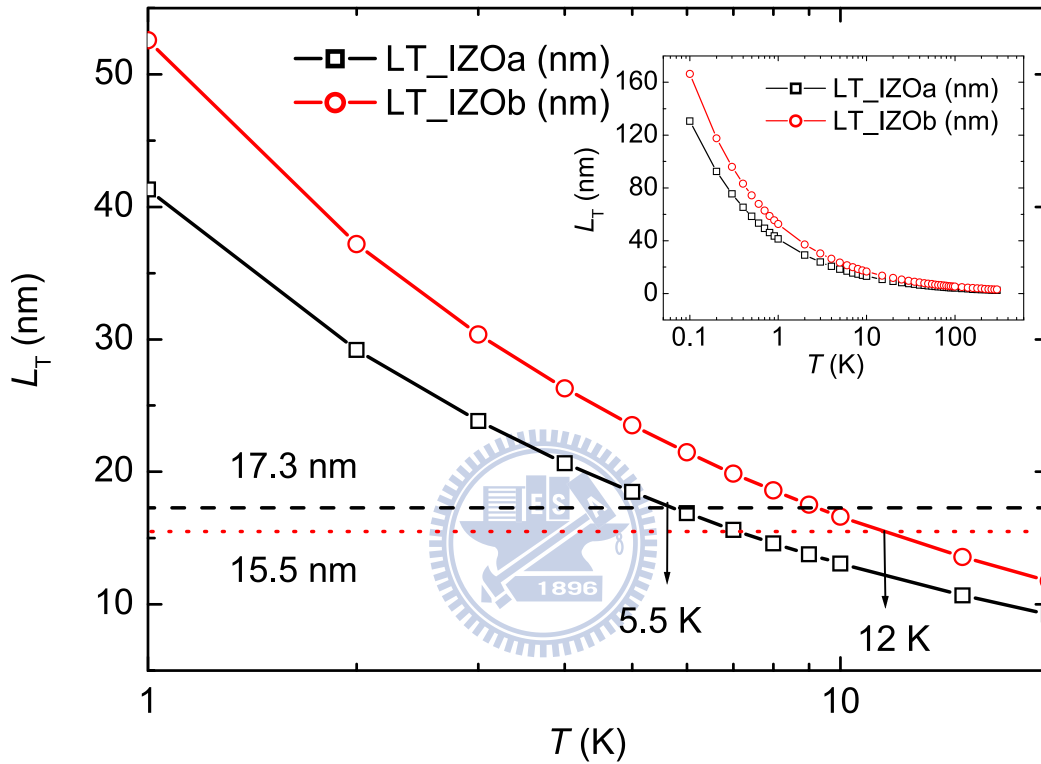

Figure 5.18: The symbols are the theoretical predicted values of thermal diffusion length, L_T, for sample IZOa and IZOb. Tha dashed and dotted lines correspond to effective film thicknesses of IZOa and IZOb. Data of wider temperature range is shown in the inset.

Hartree processes, $\tilde{F}$. In the Figure 5.16(b), the slope of the theoretical straight line is just $4/3-3\tilde{F}/2$, which gives $\tilde{F}$=0.42. We list the value of $\tilde{F}$ in the Table 5.3.

We performed similar measurement on IZOb and plotted the result in the Figure 5.17(a). It reveals that the resistivity correction from the WL effect is stronger than that from e-e interaction because the difference between the resistivities of 0 Tesla and 4 Tesla is larger than the variation of the resistivity in the 4-Tesla field. We change the scales of x-axis and re-plot the 4-Tesla data to the Figure 5.17(b) and 5.17(c). The linear region which shows $T^{1/2}$ -law between 16 and 40 K in the Figure 5.17(b) is least-squares fitted to the 3D e-e interaction theory. The extracted $\tilde{F}$ is 0.61. In the Figure 5.17(c), a different linear region between 3.6 and 12 K shows the temperature dependence of ln$T$ manifesting the signature of 2D e-e interaction. We perform curve fitting on this region by Eq. (5.7) with dimensionality d=2. The extracted $\tilde{F}$ is 0.51, similar to the value extracted from $T^{1/2}$ region. Now we meet another kind of dimensional crossover subject to the e-e interaction, occurring around 13 K. To understand how it happens, we need to recall the thermal diffusion length, L_T.

The characteristic length for e-e interaction is the thermal diffusion length, L_T. To determine the dimensionality of e-e interaction, we need to compare the L_T with the sample dimensions. L_T is defined as $L_T = \sqrt{D\hbar / k_B T}$. Diffusion constant D is assumed to be weakly temperature-dependent at low temperatures. We employ D(10 K) to estimate the L_T. The Figure 5.18 shows L_T as a function of temperature. The inset displays the L_T in wider range of temperature. The curves of L_T behave a monotonic ascending trend as temperature decreasing and cross to the two horizontal lines representing the shell thicknesses of IZOa and IZOb. The cross for IZOb reveals that the L_T is the same as shell thickness t=15.5 nm at 12 K, which is very close to the temperature, 13 K, specifying the dimensional crossover of the e-e interaction. This information is significant to the dimensional crossover of e-e interaction. According to the temperature behavior of L_T, as temperature higher than 12K, L_T would be smaller than the shell thickness and force the e-e interaction to change its dimensionality to three. As temperature lower than 12 K, L_T is longer than t, but shorter than the wire length, L, and the effective film width, w, for the quasi-two dimensional structure. Therefore the e-e interaction is two dimensional.

For IZOa, the cross marks that the L_T is the same as the shell thickness t=17.3 nm at 5.5 K, which is relatively close to the temperature, 5 K, characterizing the onset of $T^{1/2}$ -law. It's natural to happen that as temperature higher than 5.5 K, L_T is shorter than t such that the 3D e-e interaction ($\Delta\rho\sim T^{1/2}$) appears in wide range of temperature. While temperature below 5.5

K, the saturation of resistivity masks the behavior of 2D e-e interaction. Through the discussion above, the existence of core-shell-like structure can be verified by the temperature behaviors of the e-e interaction.

The low temperature resistivities of In:ZnO nanowires reveal the $T^{1/2}$ –law of 3D e-e interaction in the higher temperature region. This feature is a clue of the existence of 3D e-e scattering with large energy transfer. Therefore the temperature exponent (p~1.5) of τ_ϕ^{-1} is consistent with this feature.

5.4 Lead-doped ZnO (Pb:ZnO) nanowires

5.4.1 *Sample information*

The Pb:ZnO nanowires are synthesized by the same method as the In:ZnO nanowires. As shown in the SEM image (Figure 5.19(a)), Pb:ZnO nanowires are grown on silicon substrates. In Figure 5.19(b), the HRTEM image reveals a fairly good lattice arrangement and the single crystalline structure inside the wires. The energy dispersive X-ray (EDX) spectrum (as displayed in Figure 5.19(c)) shows that the lead to zinc atomic ratio is around 0.62%. Several single-nanowire devices in contact with four electrodes were made. The measurement of electrical transport properties and plenty of analysis were performed on a device, labeled PZOe. The parameters of the sample are listed in Table 5.1(a) and Table 5.1(b).

As shown in the Figure 5.2(b), the room temperature resistivities and the whole temperature behavior of PZOe are similar to those of IZOa. From the Table 5.1(a), (b), both of them possess very close physical parameters. Thus similar quantum transport properties would be expected in PZOe. However we'll show that PZOe possesses several distinct properties at low temperatures.

5.4.2 *Magnetoresistance and dephasing rate*

We measured the resistance with low-frequency AC resistance bridge (LR700) while magnetic field is applied perpendicular to the wire axis at the temperatures ranging from 0.26 K to 40 K. The magnetoresistances (MRs) of PZOe are presented in Figure 5.20. The SEM image of the sample is shown in the inset. As it's indicated in this figure, the MRs are almost negative variation and contain noise-like and step-like fluctuations. To have clearer view of the fluctuations, we measured the time-dependent resistances at different temperatures which

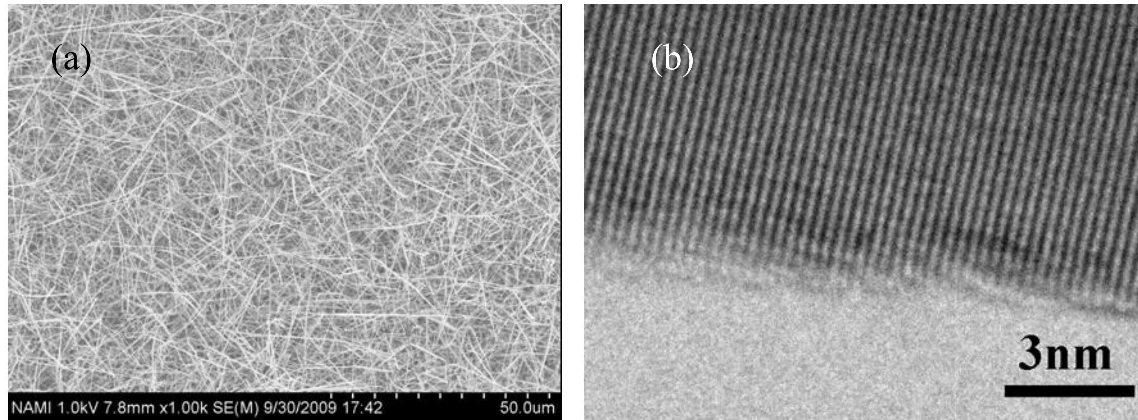

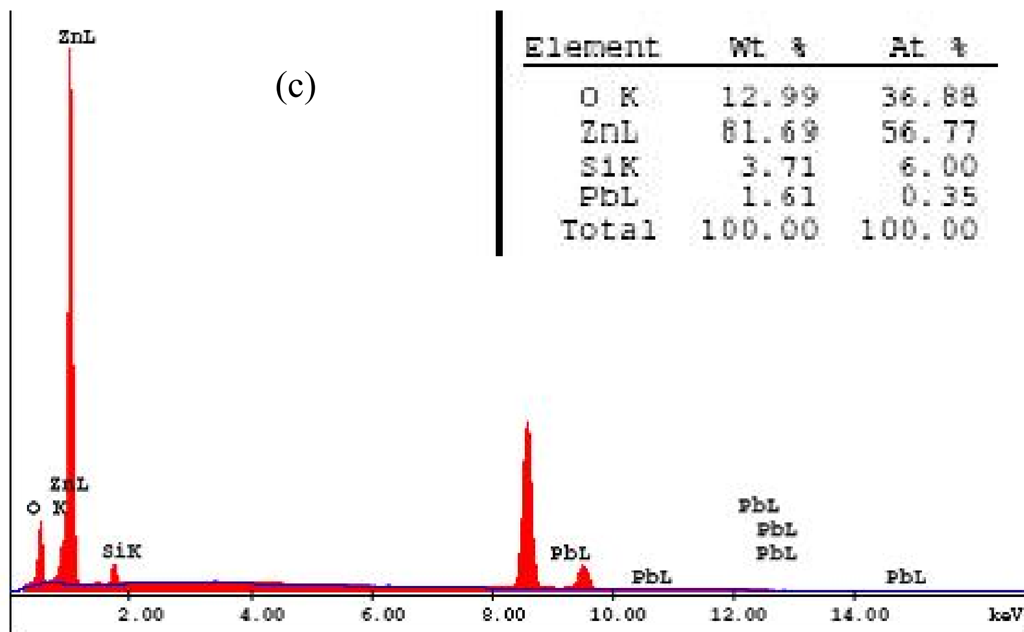

Figure 5.19: For sample PZOe, (a) A SEM image of the as-grown Pb:ZnO nanowires on the silicon substrate. (b) A high-resolution TEM image for a single nanowire. (c) EDX spectrum of Pb:ZnO nanowires. The lead to zinc atomic ratio is around 0.62%.

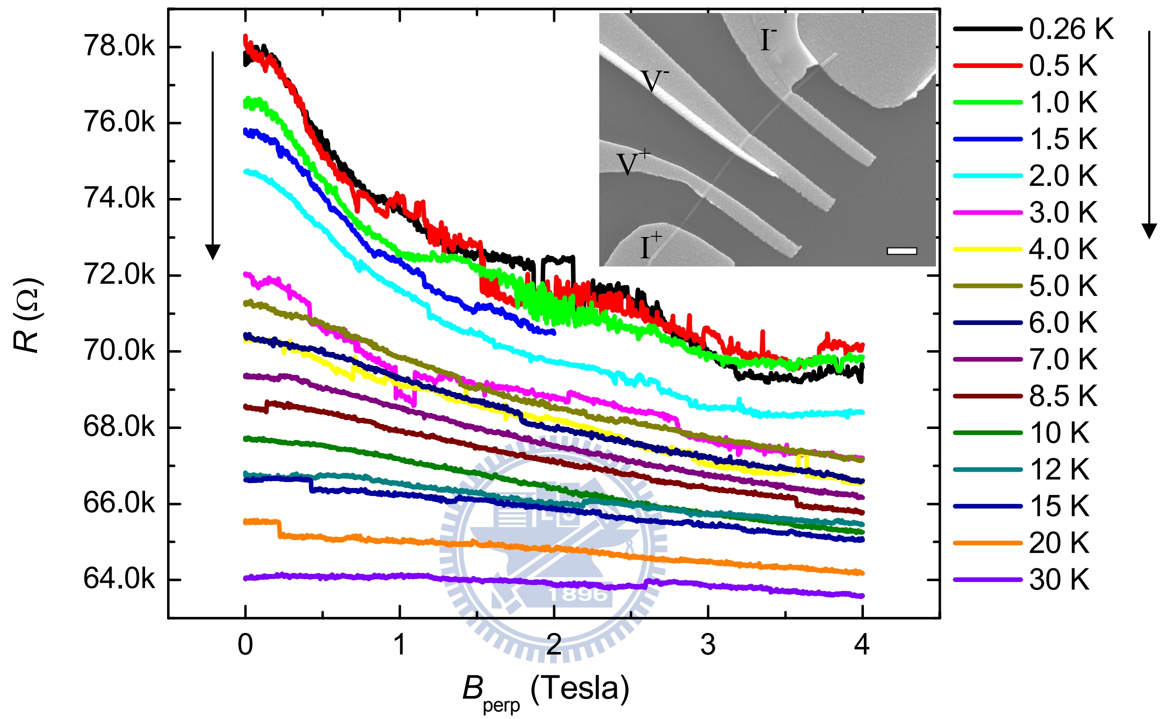

Figure 5.20: For sample PZOe, magnetoresistances as a function of perpendicular magnetic field at different temperatures. The inset shows an SEM image of the nanowire device. We perform four-probe measurement through the four electrodes marked by I^+, V^+, V^-, I^-. The scale bar is 1 μm.

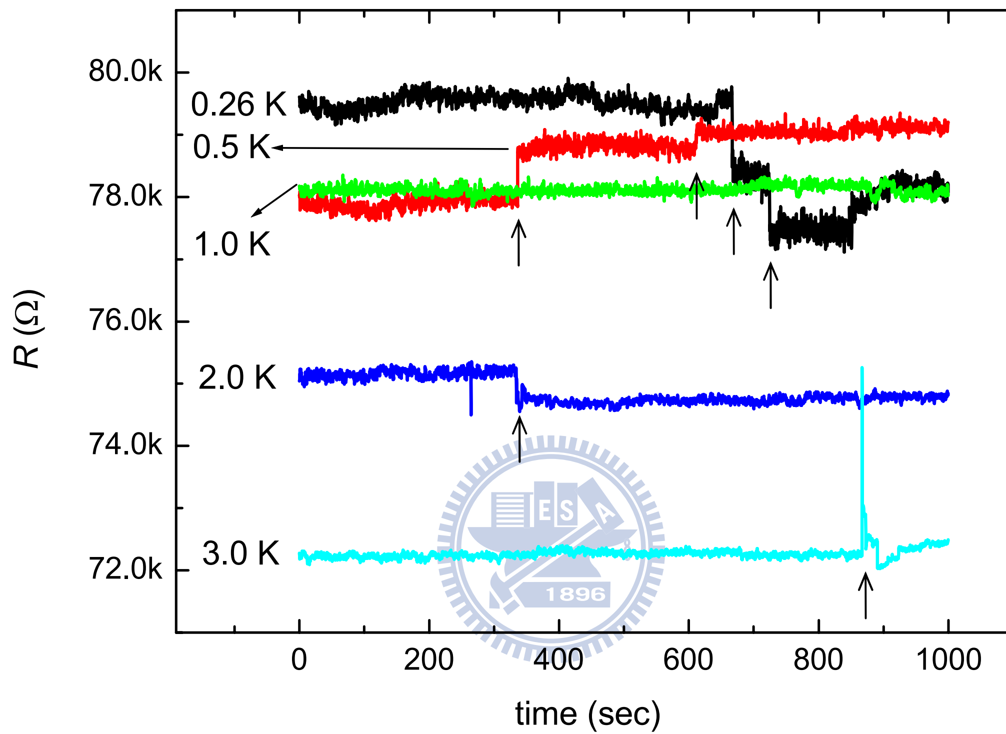

Figure 5.21: For sample PZOe, the time-dependent resistances at different temperatures.

are shown in the Figure 5.21. Two kinds of fluctuations can be distinguished in this figure. First kind is the fast-oscillated noise-like fluctuations, which oscillating amplitudes are increasing as temperature decreasing. This kind of fluctuation fits to the feature of universal conductance fluctuation (UCF) which is also characterized by the phase coherent length, L_ϕ. Second kind is the step-like fluctuations marked by arrows, which switch on a relatively slow time scale. It may be related to the motion of defects which is discussed in the framework of local interference (LI) model. Both of UCF and LI models are based on the fact that the interference *patterns* of electron waves scattered by defects depend on the detail arrangement of the defects [100].

The step-like fluctuations often disturb the MRs. In some cases, for performing better curve fitting of MRs, we shift the experimental data to eliminate the steps in MRs. In the Figure 5.22, we apply the 1D, 2D, and 3D weak localization (WL) theories on different temperature ranges to analyze the MRs. In the Figure 5.22(a), MRs between 0.26 K and 2 K are well fitted to the 1D WL theory (Eq. (5.1)). The inset shows the low-field data and fitted curve at 0.26 K. There is a slight positive variation between 0 and 0.15 Tesla, which characterizes that the phase relaxation process is dominated by spin-orbit scattering in this region, hence the weak anti-localization happens. Except 0.26 K, at other temperatures, there is no similar signature. Therefore, the spin-orbit scattering rate, τ_{so}^{-1}, is not strong such that it easy to be exceed by the inelastic scattering rate as temperature rising. The extracted L_ϕ(0.26 K) is 87 nm and the extracted spin-orbit scattering length, L_{so} is 86 nm. Comparing with the L_{so} of IZOa (~133 nm), the stronger spin-orbit scattering of PZOe should be attributed to that the atomic number of Pb is higher than that of In.

In the Figure 5.22(b), the MRs between 8.5 and 40 K are analyzed by 3D WL theory. The higher the temperatures, the better the theoretical descriptions. In the Figure 5.22(c), the MRs between 1 K and 30 K are least-squares fitted to the 2D WL theory. Most of the data can be described very well. In the inset, the theoretical curves of 1D and 2D WL effects are plotted together with the MR data at 2 K. Both of the theories can describe the low field data well, and it implies that 2 K is in the temperature region of 1D-2D dimensional crossover of WL effect. The related parameters of curve fitting are listed in the Table 5.2.

The extracted L_ϕ's are plotted as a function of temperature in the Figure 5.23(a). It indicates that L_ϕ increases from 10 nm to 87 nm as the temperature decreasing from 30 K to 0.26 K. The horizontal dashed line marks the effective wire width, a=55 nm. It crosses the L_ϕ data at 1.5 K, behaving as the characteristic length for the 1D-2D dimensional crossover of

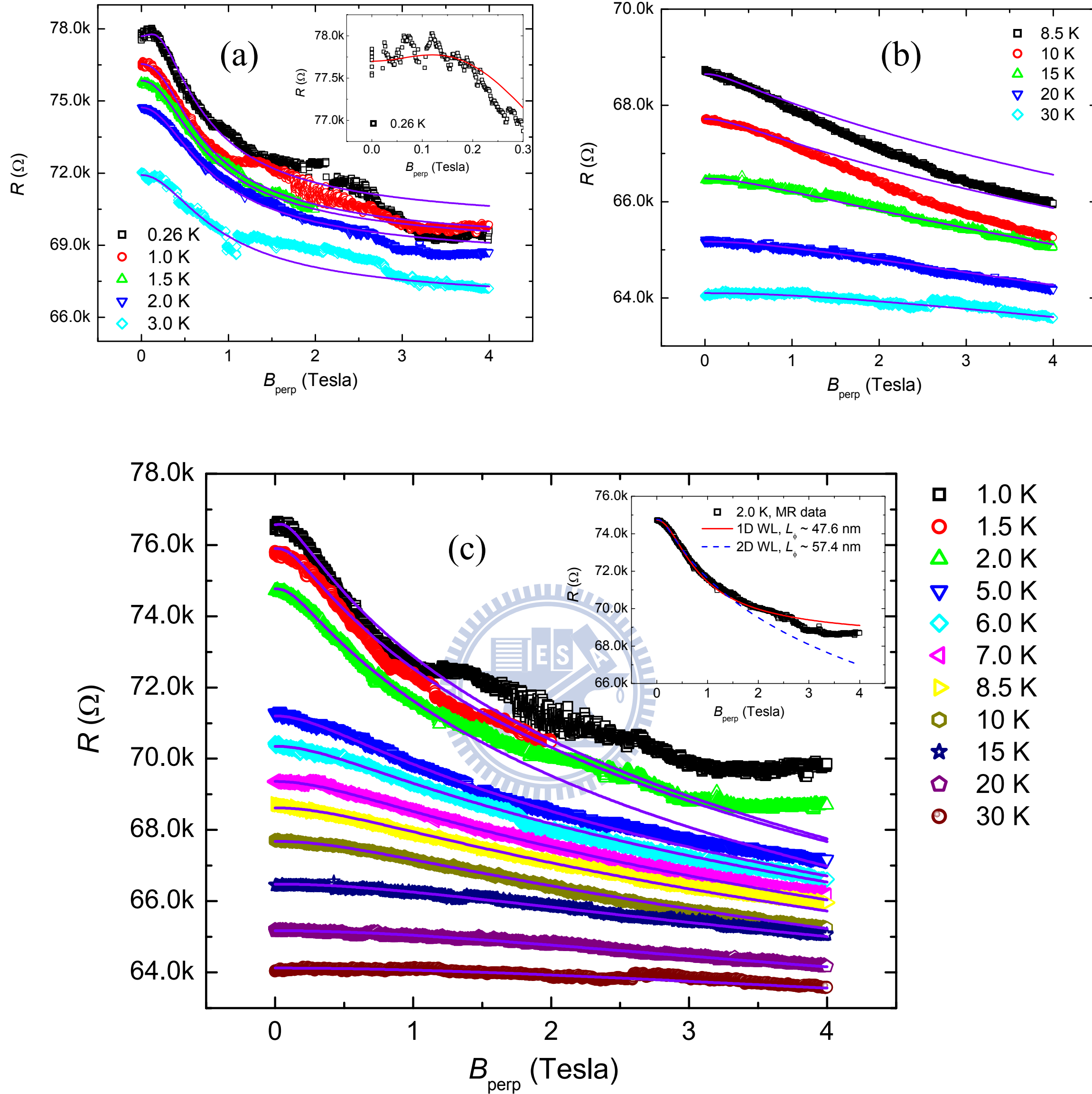

Figure 5.22: For sample PZOe. The symbols are the MR data in the perpendicular magnetic field. (a) The solid curves are the theoretical curves predicted by the 1D WL effect (Eq. (5.1)). (b) The solid curves are the theoretical curves predicted by the 3D WL effect (Eq. (5.4)). (c) Solid curves are the theoretical curves predicted by the 2D WL effect (Eq. (5.2)) The inset shows the data of 20 K and the theoretical curves predicted by 1D and 2D WL effects.

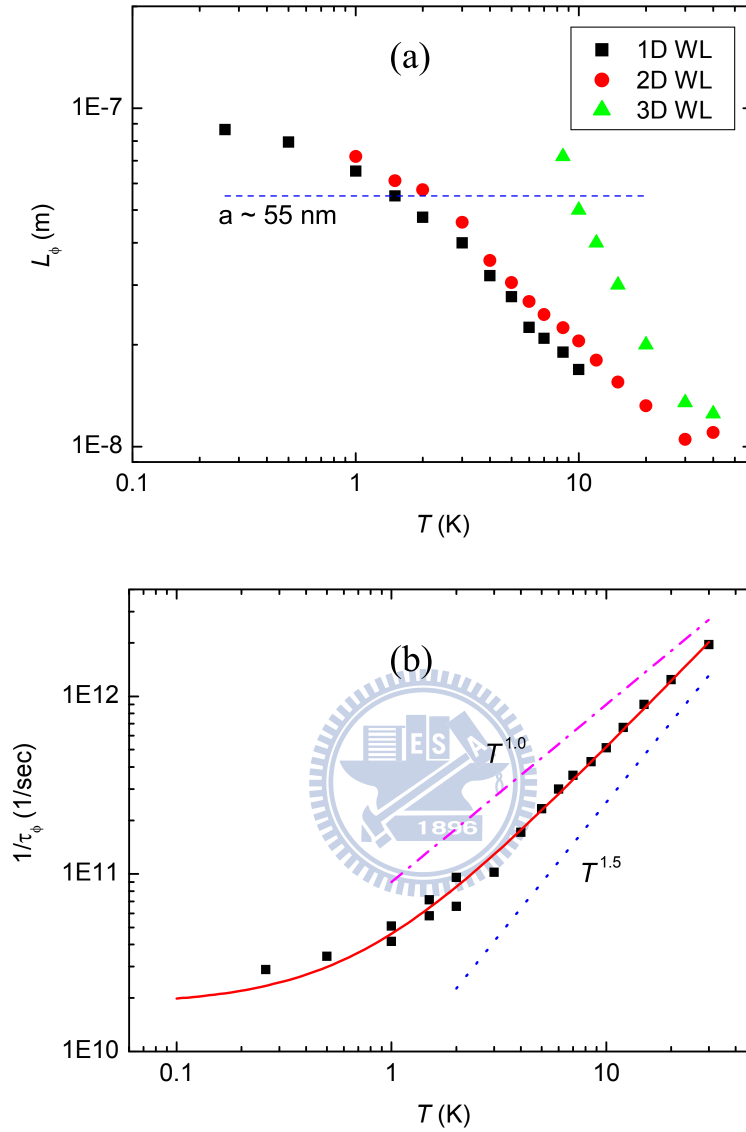

Figure 5.23: For sample PZOe. (a) The extracted phase coherent lengths, L_ϕ's, as a function of temperature. Dashed line marks the effective wire width, a. (b) Dephasing rates transferred from selected L_ϕ's as a function of temperature. The solid curve is theoretical curve by Eq. (5.8a).

WL effect. The L_ϕ's of 2D and 3D WL effects are starting to coincide together around 30 K, such that the 2D-3D dimensional crossover of WL effect is expected to occur at higher temperatures than 30 K (The 40 K data is not in line with the trend of other data, therefore we ignore it.). The L_ϕ of 30 K is around 10 nm, so that if core-shell-like structure exists, the shell thickness should be smaller than 10 nm.

We choose the L_ϕ's of 1D WL effect between 0.26 and 2 K and the L_ϕ's of 2D WL effect between 1 and 30 K to transfer to dephasing rate, τ_ϕ^{-1}, and plot them in the Figure 5.23(b). The τ_ϕ^{-1}'s can be well fitted to the Eq. (5.8a), and then related parameters (τ_0, A, and p) are extracted. We list the τ_0, A, and p in the Table 5.3. The value of p (p ~1.2) is a little smaller than those of In:ZnO nanowires. There are several candidate mechanisms related to this p value. The two-dimensional electron-electron scattering with small energy transfer gives p=1, i.e. $\tau_N^{-1} \sim T$. The two-dimensional electron-electron scattering with large energy transfer in the dirty metal limit gives $\tau_{i,ee}^{-1} \sim T \ln T$, where we use $\tau_{i,ee}^{-1}$ (and τ_N^{-1}) to distinguish the large and small energy transfer. Also, the three-dimensional case mentioned in section 5.3.3 gives $\tau_{i,ee}^{-1} \sim T^{3/2}$. Furthermore, considering the phonon dimension confined by the shell thickness, the exponent of the electron-phonon scattering rate may be reduced to this value (p~1.2).

5.4.3 *Electron-electron interaction and the nonlinearity of I-V curves*

Here the low-temperature resistances are measured in the 0-Tesla and 4-Tesla magnetic fields. We show the results in the Figure 5.24. As it's shown, the 0-Tesla data has a bending-down behavior around 0.6 K (marked by an arrow), which results from the domination of spin-orbit scattering below 0.6 K. The 4-Tesla data seems to possess two branches which ought to originate from the step-like fluctuations mentioned above. If we consider the lower branch, it shows a linear region between 2 K and 30 K under the logarithmic x-axis, manifesting the 2D e-e interaction ($\Delta\rho \sim \ln T$). We perform curve fitting on this region with Eq. (5.7) with dimensionality d=2 and extract the coupling constant of Hartree processes, $\tilde{F}$ ($\tilde{F}$ ~0.75). Comparing with the estimated L_T (L_T ~ 8 nm at 30 K) with the shell thickness (t < 10 nm), the 2D behavior is consistent with the relatively thin shell thickness in this sample. This behavior also implies the existence of 2D electron-electron scattering with large energy transfer and supports the exponent p extracted from τ_ϕ^{-1}.

This Pb:ZnO nanowire possesses a distinct property in its I-V curves. The Figure 5.25(a) presents the I-V curves at different temperatures between 1.35 and 12 K. The current range is

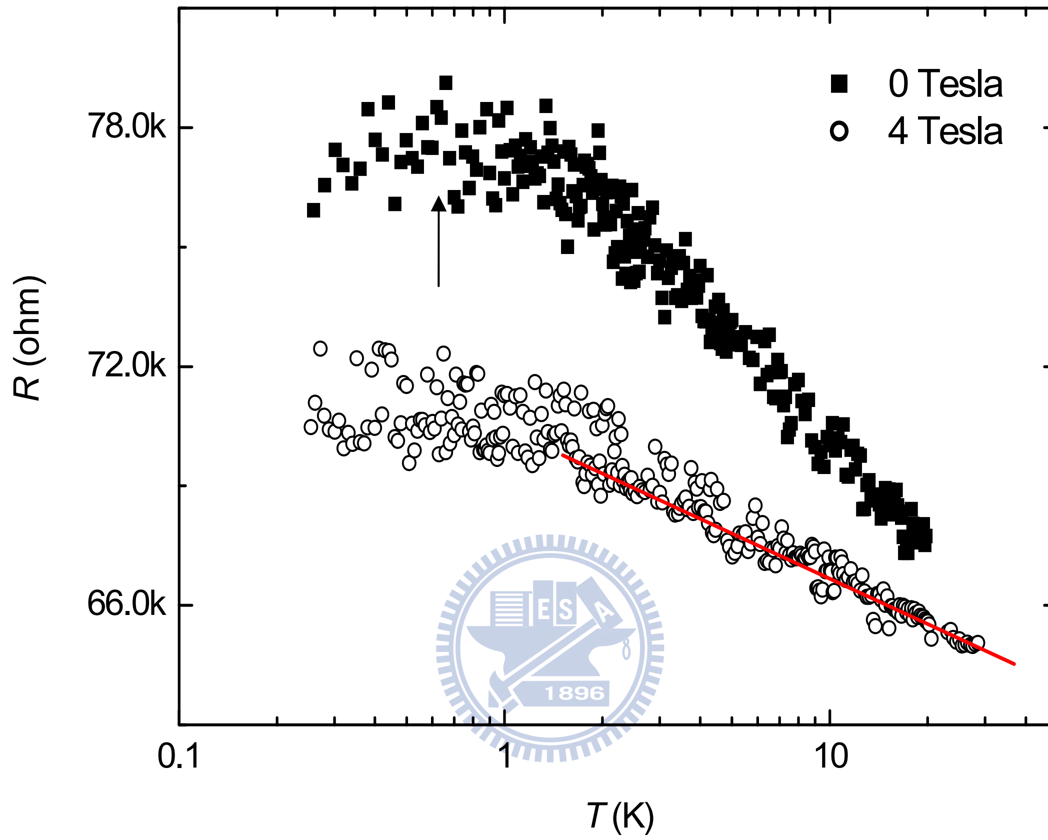

Figure 5.24: For sample PZOe, The symbols are the resistivities as functions of temperature in the 0-Tesla and 4-Tesla magnetic fields. Solid curve is the theoretical curve predicted by Eq. (5.7).

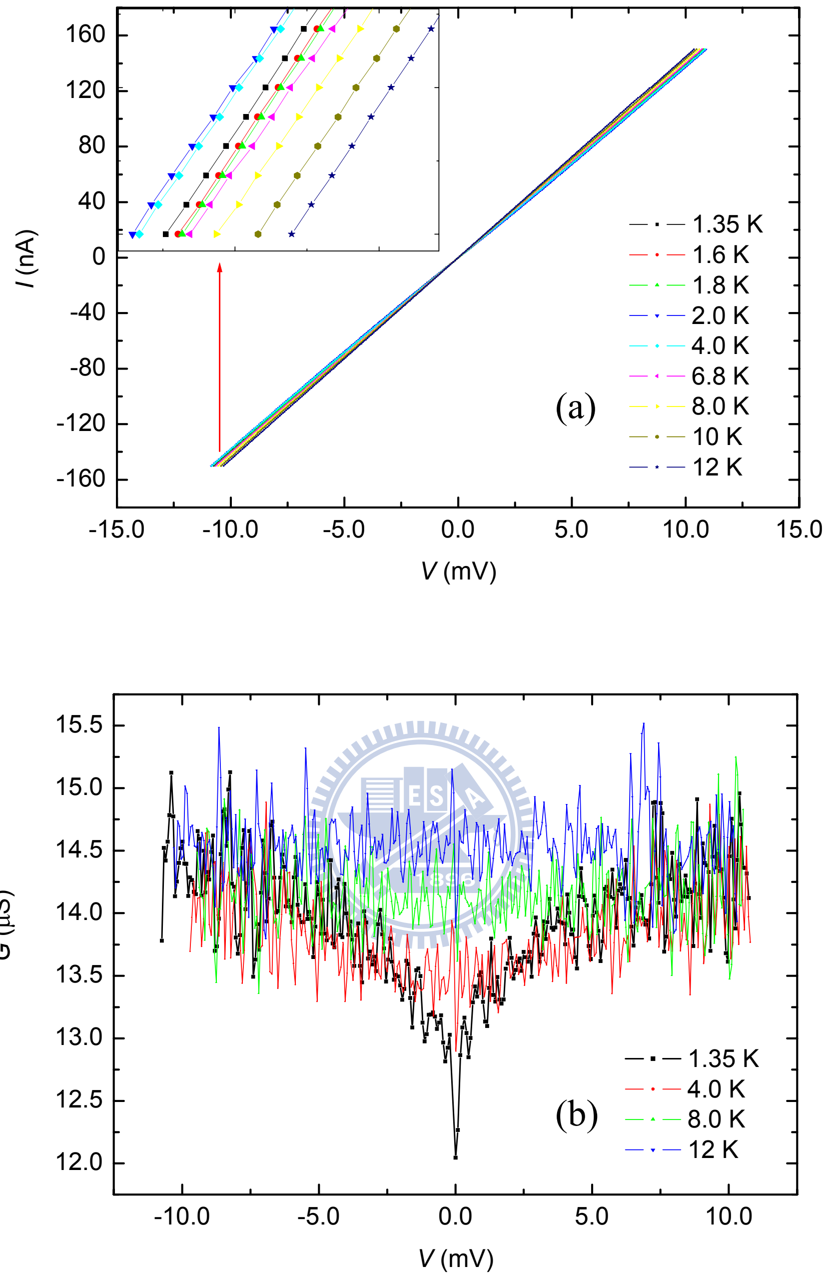

Figure 5.25: For sample PZOe. (a) The I-V curves at different temperatures. Inset is the zoom-in of high-bias region. (b) The $G(V)$ differentiated from I-V curves at different temperatures.

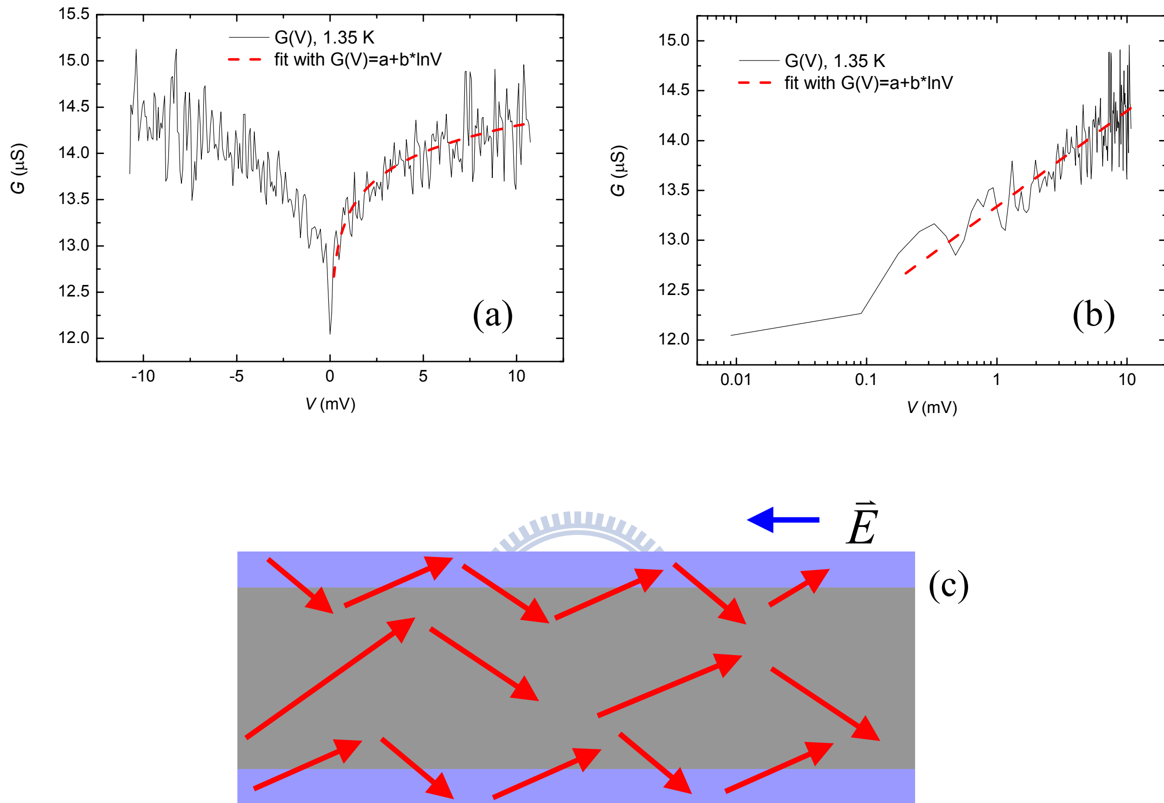

Figure 5.26: For sample PZOe. (a) The $G(V)$ differentiated from I-V curves at 1.35 K. Dashed curves is described by $G(V)=a+b*\ln V$. (b) The same content as (a) but plotted in logarithmic x-axis. (c) A scheme describes the electron transport through the interfaces of core and shell in nanowires.

up to 150 nano-Ampere (nA), which is much larger than the current employed to measure resistance (typically, 3 nA). The inset is the zoom-in of high-bias region. Taking a glance at these curves, they are fairly linear. However, if we differentiate the data and take the reciprocal, the conductance will be generated as a function of voltage, G(V), as shown in the Figure 5.25(b). Now, we can find there are conductance dips around zero-bias. Lower the temperatures, larger the dips. We choose the data of 1.35 K for qualitative analysis. As it's shown in the Figure 5.26(b), the $G(V)$ possesses a $\ln V$ behavior, so that the G(V) data is well described by the relation of $G(V) \sim a + b \ln V$, as displayed in the Figure 5.26(a). This result is analogue to the zero-bias anomaly in the tunneling junctions [39], which reveals the shape of the density of states of the thin conductors near the Fermi surface. Here, we suppose a physical picture (Figure 5.26(c)) that there are electron transport processes passing through the interfaces between the core and shell, analogous to the tunneling junction, thus the density of states of the shell affects the conductance and results the conductance dip at zero-bias.

5.5 Summary

The indium- and lead-doped ZnO NWs with diameters of 70 to 90 nm showed behavior of degenerate Fermi gas of their resistivities, $\rho(T)$. We have measured the MRs of several doped ZnO NWs between 0.25 and 70 K in magnetic fields with directions both perpendicular and parallel to the wire axes. Our quantitative analysis showed that we have to utilize the weak-localization (WL) effects of different dimensionalities to explain the MRs in different ranges of temperature. Otherwise, the MRs can not be satisfactorily described. A characteristic length, named the effective wire width, a, extracted from one-dimensional (1D) WL effect has been introduced. From the perpendicular and parallel MRs, another characteristic length, named the effective film thicknesses, t, was extracted under the framework of the two-dimensional (2D) WL effect. Hence, a core-shell-like structure inside individual nanowires is suggested. Within this model, as the electron phase-coherent length, L_ϕ, decreases with increasing temperature, a 1D-to-2D dimensional crossover of the WL effect occurs around the characteristic temperature where $L_\phi \sim a$, and also a 2D-to-3D dimensional crossover occurs around another characteristic temperature where $L_\phi \sim t$. The exponent of temperature, p, of the electron dephasing rate, τ_ϕ^{-1}, has been determined. The result suggests that the dephasing mechanisms could be due to the electron-electron (e-e) scattering with large energy transfer or the electron-phonon (e-ph) scattering with reduced phonon

dimensionality. In addition, the core-shell-like structure has been verified from the temperature behaviors of low-temperature resistivities in a moderately high magnetic field, which demonstrated the dominating electron-electron interaction (EEI) effect. A dimensional crossover of EEI was also observed under the condition that the thermal diffusion length, L_T, became close to the shell thickness t. In a lead-doped ZnO NW, the nonlinearity of the I-V curves around zero-bias is attributed to the 2D property of relatively small shell thickness and the electron motion across the core-shell interface.

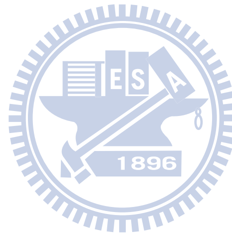

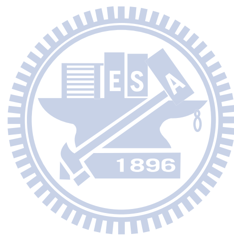

Chapter 6

Conclusion

Through the four-probe measurement, the intrinsic electrical properties of the individual NWs can be reflected on resistances (or resistivities) which depend on several physical quantities such as temperature, magnetic field, bias voltage, and so on.

With the ITO NWs as the example, although the contact resistances, R_c, show the metallic behavior and possess fairly small value, the two-probe resistance, $R_{2p}(T)$, is still easy to mislead the investigation of intrinsic electrical properties. Therefore the importance of four-probe measurement is without a doubt.

The high-temperature parts of measured $\rho(T)$ of the ITO NWs are dominated by the electron-phonon scattering which is known as the Bloch–Grüneisen law. The low-temperature parts of measured $\rho(T)$ obey the $T^{1/2}$-law, which is reminiscent of 3D electron-electron interaction (EEI). However, the resistivity rises are more than one order of magnitude, as would be expected from the corrections due to the 3D EEI and weak localization (WL) effects. The dynamic defects which often be modeled as two-level tunneling systems can lead to an additional $T^{1/2}$-correction to the low-temperature resistivity. The electron–dynamic defect scattering can be described in terms of the *nonmagnetic* two-channel Kondo effect as described in Eq. (3.2). The dynamic defects are likely associated with the numerous point defects which inevitably exist in as-grown ITO NWs.

The temperature behaviors of resistivity in both the semiconducting and the metallic-like ZnO NWs have been carefully measured and the conduction mechanisms satisfactorily explained. A particular band structure is form in the semiconducting ZnO NWs due to the intricate material properties, that is, they are natively moderately doped as well as slightly self-compensated. The slight self-compensation leads to the nearest-neighbor hopping in the lower D-band around Fermi energy. The E_3 is the order of energy level spacing of lower D-band. Moderate doping generates extended overlapping of wavefunctions originally located at different donor sites to form the upper D^--band. However, the dopant concentration is not high enough to drive the upper D^--band to overlap with conduction band. Therefore, we can see the E_2-conduction. As temperature rises above 100 K, the thermal energy is high enough to activate more localized electrons across the E_1-gap to the conduction band and then the electrical conduction is dominated by the free carrier concentration in the conduction band. In

a heavily doped, metallic-like ZnO NW, two-dimensional (2D) WL and EEI effects was observed, implying the surface-related conduction process. This feature also gives us a hint when we analyzed the transport properties of doped ZnO NWs.

The core-shell-like structure inside our doped ZnO NWs is inevitably built to explain the MRs, ρ(T)'s, and I-V curves in a satisfactory way. There are two important reasons why this structure can exists in our NWs. First, our wire diameters are not very small; otherwise the core-shell-like structure will collapse to the simple rod structure. Second, the surface of doped ZnO NWs is easy to be modified to a disordered configuration differing from the core of the NWs.

The shell thickness (or effective film thickness), t, phase coherent length, L_ϕ, and thermal diffusion length, L_T, play the important roles to characterize the two- and three- dimensional crossover of the WL and EEI effects. The condition of '$L_\phi \sim t$' causes the crossover of the 2D and 3D WL effects. Similarly, the condition of '$L_T \sim t$' results in the crossover of the 2D and 3D EEI effects. Another important length scale is the effective wire width, a. As the L_ϕ is close to a, the crossover of the 1D and 2D WL effects happens. The temperature behavior of the L_ϕ and the nonlinearity of I-V curves also respond to the core-shell-like structure. The smaller temperature exponent p of τ_ϕ^{-1} may originate from the electron-electron scattering with large energy transfer and the electron-phonon scattering of 2D phonons. The different dopants (In and Pb) cause the different spin-orbit coupling strength and seem to generate different types of resistance fluctuation. The reason why the In- and Pb-doped ZnO NWs possess different shell thicknesses is unclear and more experimental research is needed. From the results above, we know that the quantum interference effects could be the powerful probe to discover the microscopic properties in the mesoscopic nano-structures.

To further understand the properties of the core-shell-like structure in the doped ZnO NWs, several experiments are suggested. (a) The cross-wire devices act as tunneling junctions or quantum point contacts for discovering the surface (shell) properties. (b) If utilizing back-gate voltage to control the depletion region and form the remaining electrical conduction region on the top surface of the NWs, the measured resistivity will be almost contributed from the top surface. This experiment may reveal the electrical transport property of NW surfaces. (c) If utilizing Ω-shaped top-gate and back-gate voltage to control the depletion region and form the remaining electrical conduction region in the *core* of the NWs, the electrical transport properties of the core should be exhibited.

References

[1] S. Iijima, *Nature* **354**, 56 (1991).

[2] C. M. Lieber and Z. L. Wang, *MRS Bull.* **32**, 99 (2007).

[3] W. Lu and C. M. Lieber, *nature materials* **6**, 841 (2007).

[4] J. G. Lu, P. C. Chang and Z. Fan, *Mater. Sci. Eng. R.* **52**, 49 (2006).

[5] M. T. Björk, C. Thelander, A. E. Hansen, L. E. Jensen, M. W. Larsson, L. R. Wallenberg, and L. Samuelson, *Nano Lett.* **4**, 1621 (2004).

[6] Y. Hu, H. O. H. Churchill, D. J. Reilly, J. Xiang, C. M. Lieber, and C. M. Marcus, *nature nanotechnology* **2**, 622 (2007).

[7] T. Dietl, *Semicond. Sci. Technol.* **17**, 377 (2002).

[8] J. J. Lin, and J. P. Bird, *J. Phys: Condens. Matter* **14**, R501 (2002).

[9] Z. Fan, and J. G. Lu, *J. Nanosci. Nanotechnol.* **5**, 1561 (2005).

[10] Z. L. Wang, *J. Phys.: Condens. Matter* **16**, R829 (2004).

[11] R. S. Thompson, D. Li, C. M. Witte, and J. G. Lu, *Nano Lett.* **9**, 3991 (2009).

[12] X. F. Duan, C. M. Lieber, *Adv. Mater.* **12**, 298 (2000).

[13] J. F. Lin, J. P. Bird, L. Rotkina and P. A. Bennett, *Appl. Phys.Lett.* **82**, 802 (2003).

[14] H. Wang, J. Wang, M. Tian, L. Bell, E. Hutchinson, M. M. Rosario, Y. Liu, A. Amma and T. Mallouk, *Appl. Phys. Lett.* **84**, 5171 (2004).

[15] F. Vaurette, R. Leturcq, J. P. Nys, D. Deresmes, B. Grandidier and D. St´ıevenard, *Appl. Phys. Lett.* **92**, 242109 (2008).

[16] P. C. Chang, C. J. Chien, D. Stichtenoth, C. Ronning and J. G. Lu, *Appl. Phys. Lett.* **90**, 113101 (2007).

[17] S. Song, W. K. Hong, S. S. Kwon and T. Lee, *Appl. Phys. Lett.* **92**, 263109 (2008).

[18] F. J. Rueß, B. Weber, K. E. J. Goh, O. Klochan, A. R. Hamilton and M. Y. Simmons, *Phys. Rev.* B **76**, 085403 (2007).

[19] Y. H. Lin, Y. C. Sun, W. B. Jian, H. M. Chang, Y. S. Huang and J. J. Lin, *Nanotechnology* **19**, 045711 (2008).

[20] A. Motayed, A. V. Davydov, S. N. Mohammad and J. Melngailis, *J. Appl. Phys.* **104**, 024302 (2008).

[21] S. P. Chiu, Y. H. Lin and J. J. Lin, *Nanotechnology* **20**, 015203 (2009).

[22] X. S. Peng, G. W. Meng, X. F. Wang, Y. W. Wang, J. Zhang, X. Liu and L. D. Zhang *Chem. Mater.* **14**, 4490 (2002).

[23] Q. Wan, Z. T. Song, S. L. Feng and T. H. Wang, *Appl. Phys. Lett.* **85**, 4759 (2004).

[24] S. Y. Li, C. Y. Lee, P. Lin and T. Y. Tseng, *Nanotechnology* **16**, 451 (2005).

[25] K. P. Kalyanikutty, G. Gundiah, C. Edem, A. Govindaraj and C. N. R. Rao, *Chem. Phys. Lett.* **408**, 389 (2005).

[26] D. Lin, H. Wu, R. Zhang and W. Pan, *Nanotechnology* **18**, 465301 (2007).

[27] Z. Q. Li and J. J. Lin, *J. Appl. Phys.* **96**, 5918 (2004).

[28] X. D. Liu, E. Y. Jiang and D. X. Zhang, *J. Appl. Phys.* **104**, 073711 (2008).

[29] B. T. Lin, Y. F. Chen, J. J. Lin and C. Y. Wu, in preparation (2008).

[30] R. B. H. Tahar, T. Ban, Y. Ohya and Y. Takahashi, *J. Appl. Phys.* **83**, 2631 (1998).

[31] Q. Wan, E. N. Dattoli, W. Y. Fung, W. Guo, Y. Chen, X. Pan and W. Lu, *Nano Lett.* **6**, 2909 (2006).

[32] A. J. Chiquito, A. J. C. Lanfredi, R. F. M. de Oliveira, L. P. Pozzi and E. R. Leite, *Nano Lett.* **7**, 1439 (2007).

[33] Y. H. Lin, S. P. Chiu and J. J. Lin, *Nanotechnology* **19**, 365201 (2008).

[34] M. W. Larsson, L. R. Wallenberg, A. I. Persson and L. Samuelson, *Microsc. Microanal.* **10**, 41 (2004).

[35] T. Ohyama, M. Okamoto and E. Otsuka, *J. Phys. Soc. Japan* **54**, 1041 (1985).

[36] N. Mori, *J. Appl. Phys.* **73**, 1327 (1993).

[37] J. M. Ziman, *Electrons and Phonons* (Oxford: Clarendon, 1960).

[38] Y. L. Liu, Z. Y. Wu, K. J. Lin, J. J. Huang, F. R. Chen, J. J. Kai, Y. H. Lin, W. B. Jian and J. J. Lin, *Appl. Phys. Lett.***90**, 013105 (2007).

[39] B. L. Al'tshuler and A. G. Aronov, *Electron–Electron Interactions in Disordered Systems* ed. A. L. Efros and M. Pollak (Amsterdam: Elsevier, 1985).

[40] J. J. Lin and C. Y. Wu, *Phys. Rev.* B **48**, 5021 (1993).

[41] I. Affleck and A. W. W. Ludwig, *Phys. Rev.* B **48**, 7297 (1993).

[42] F. G. Aliev, V. V. Moshchalkov and Y. Bruynseraede, *Phys. Rev.* B **58**, 3625 (1998).

[43] T. Cichorek, A. Sanchez, P. Gegenwart, F. Weickert, A. Wojakowski, Z. Henkie, G. Auffermann, S. Paschen, R. Kniep and F. Steglich, *Phys. Rev. Lett.* **94**, 236603 (2005).

[44] O. N. Mryasov and A. J. Freeman, *Phys. Rev.* B **64**, 233111 (2001).

[45] H. Odaka, Y. Shigesato, T. Murakami and S. Iwata, *Japan. J. Appl. Phys.* **40**, 3231 (2001).

[46] C. Kittel, *Introduction to Solid State Physics* (New York: Wiley, 2005).

[47] J. Kondo, *Prog. Theor. Phys.* **32**, 37 (1964).

[48] S. J. Pearton, D. P. Norton, K. Ip, Y. W. Heo and T. Steiner, *Superlatt. Microstruct.* **34**, 3 (2003).

[49] Ü. Ozgür, Y. I. Alivov, C. Liu, A. Teke, M. A. Reshchikov, S. Do˘gan, V. Avrutin, S. J. Cho, and H. Morkoc, *J. Appl. Phys.* **98**, 041301 (2005).

[50] C. Klingshirn, *Phys. Status Solidi* b **244**, 3027 (2007).

[51] D. C. Look, G. C. Farlow, P. Reunchan, S. Limpijumnong, S. B. Zhang and K. Nordlund, *Phys. Rev. Lett.* **95**, 225502 (2005).

[52] C. G. Van de Walle, *Phys. Rev. Lett.* **85**, 1012 (2000).

[53] D. M. Hofmann, A. Hofstaetter, F. Leiter, H. Zhou, F. Henecker, B. K. Meyer, S. B. Orlinskii, J. Schmidt and P. G. Baranov, *Phys. Rev. Lett.* **88**, 045504 (2002).

[54] S. Lany and A. Zunger, *Phys. Rev. Lett.* **98**, 045501 (2007).

[55] F. A. Selim, M. H. Weber, D. Solodovnikov and K. G. Lynn, *Phys. Rev. Lett.* **99**, 085502 (2007).

[56] Y. W. Heo, D. P. Norton, L. C. Tien, Y. Kwon, B. S. Kang, F. Ren, S. J. Pearton and J. R. LaRoche, *Mater. Sci. Eng.* R **47**, 1 (2004).

[57] Y. W. Heo, L. C. Tien, D. P. Norton, B. S. Kang, F. Ren, B. P. Gila and S. J. Pearton, *Appl. Phys. Lett.* **85**, 2002 (2004).

[58] Y. J. Ma, Z. Zhang, F. Zhou, L. Lu, A. Jin and C. Gu, *Nanotechnology* **16**, 746 (2005).

[59] X. Lin, X. B. He, T. Z. Yang, W. Guo, D. X. Shi, H. J. Gao, D. D. D. Ma, S. T. Lee, F. Liu and X. C. Xie, *Appl. Phys. Lett.* **89**, 043103 (2006).

[60] E. Schlenker, A. Bakin, T. Weimann, P. Hinze, D. H. Weber, A. G¨olzh¨auser, H. H. Wehmann and A. Waag, *Nanotechnology* **19**, 365707 (2008).

[61] Z. Fan, D. Wang, P. C. Chang, W. Y. Tseng and J. G. Lu, *Appl. Phys. Lett.* **85**, 5923 (2004).

[62] J. Goldberger, D. J. Sirbuly, M. Law and P. Yang, *J. Phys. Chem.* B **109**, 9 (2005).

[63] P. C. Chang, C. J. Chien, D. Stichtenoth, C. Ronning and J. G. Lu, *Appl. Phys. Lett.* **90**, 113101 (2007).

[64] Y. F. Lin, W. B. Jian, C. P. Wang, Y. W. Suen, Z. Y. Wu, F. R. Chen, J. J. Kai and J. J. Lin, *Appl. Phys. Lett.* **90**, 223117 (2007).

[65] N. F. Mott and W. D. Twose, *Adv. Phys.* **10**, 107 (1961).

[66] Z. Y. Wu, I. J. Chen, Y. F. Lin, S. P. Chiu, F. R. Chen, J. J. Kai, J. J. Lin and W. B. Jian, *New J. Phys.* **10** 033017 (2008).

[67] H. Nishimura, *Phys. Rev.* **138**, A815 (1965).

[68] B. I. Shklovskii and A. L. Efros, *Electronic Properties of Doped Semiconductors* (New York: Springer, 1984).

[69] C. S. Hung and J. R. Gliessman, *Phys. Rev.* **96**, 1226 (1954).

[70] N. F. Mott and E. A. Davis, *Electronic Processes in Non-Crystalline Materials* (Oxford: Clarendon, 1979).

[71] P. Norton, *Phys. Rev. Lett.* **37**, 164 (1976).

[72] D. C. Look, C. Coskun, B. Claflin and G. C. Farlow, *Physica* B **340–342**, 32 (2003).

[73] M. I. Daunov, R. K. Arslanov, M. M. Gadjialiev, E. V. Kortunova, P. P. Khokhlachev and P. P. Shvansky, *Semiconductors* **40**, 1255 (2006). 4-29

[74] C. H. Seager and S. M. Myers, *J. Appl. Phys.* **94**, 2888 (2003).

[75] H. Fritzsche, *Phys. Rev.* **99**, 406 (1955).

[76] G. Sadasiv, *Phys. Rev.* **128**, 1131 (1962).

[77] E. A. Davis and W. D. Compton, *Phys. Rev.* **140**, A2183 (1965).

[78] J. Gu, T. Kitahara, K. Kawakami and T. Sakaguchi, *J. Appl. Phys.* **46**, 1184 (1975).

[79] J. R. Sites and A. K. Nedoluha, *Phys. Rev.* B **24**, 4309 (1981).

[80] F. A. J. M. Driessen, G. J. Bauhuis, S. M. Olsthoorn and L. J. Giling, *Phys. Rev.* B **48**, 7889 (1993).

[81] G. J. Bauhuis, F. A. J. M. Driessen and L. J. Giling, *Phys. Rev.* B **48**, 17239 (1993).

[82] N. V. Agrinskaya, V. I. Kozub, T. A. Polyanskaya and A. S. Saidov, *Semiconductors* **33**, 135 (1999).

[83] P. C. Chang and J. G. Lu, *Appl. Phys. Lett.* **92**, 212113 (2008).

[84] N. F. Mott and E. A. Davis, *Phil. Mag.* **17**, 1269 (1968).

[85] J. J. Lin and N. Giordano, *Phys. Rev.* B **35**, 545 (1987).

[86] S. Hikami, A. I. Larkin and Y. Nagaoka, *Prog. Theor. Phys.* **63**, 707 (1980).

[87] A. J. Chiquito, A. J. C. Lanfredi, R. F. M. de Oliveira, L. P. Pozzi and E. R. Leite, *Nano Lett.* **7**, 1439 (2007).

[88] D. C. Look, B. Claflin and H. E. Smith, *Appl. Phys. Lett.* **92**, 122108 (2008).

[89] O. Schmidt, P.Kiesel, D. Ehrentraut, T. Fukuda and N. M. Johnson, *Appl. Phys.* A **88**, 71 (2007).

[90] K. Ellmer, *J. Phys. D: Appl. Phys.* **34**, 3097 (2001).

[91] N. F. Mott, *Proc. R. Soc.* A **382**, 1 (1982).

[92] A. R. Hutson, *Phys. Rev.* **108**, 222 (1957).

[93] D. C. Look, D. C. Reynolds, J. R. Sizelove, R. L. Jones, C. W. Litton, G. Cantwell and W. C. Harsch, *Solid State Commun.* **105**, 399 (1998).

[94] W. L. McMillan and J. Mochel, *Phys. Rev. Lett.* **46**, 556 (1981).

[95] J. S. Dugdale, *The electrical properties of disordered metals*, (Cambridge, 1995).

[96] W. S. Baer, *Phys. Rev.* **154**, 785 (1967).

[97] S. P. Chiu, H. F. Chung, Y. H. Lin, J. J. Kai, F. R. Chen, and J. J. Lin, *Nanotechnology* **20**, 105203 (2009).

[98] B. L. Altshuler and A. G. Aronov, *JETP Lett* **33**, 499 (1981).

[99] F. Pierre, A. B. Gougam, A. Anthore, H. Pothier, D. Esteve, N. O. Birge, *Phys. Rev. B* **68**, 085413 (2003).

[100] N. Giordano, *Mesoscopic Phenomena in Solids* ed. B.L. Altshuler, P.A. Lee, and R.A. Webb (North Holland, 1991).

[101] B. L. Altshuler, A. G. Aronov and D. E. Khmelnitsky, *J. Phys. C: Solid State Phys.* **15**, 7367 (1982).

[102] S. Maekawa, and H. Fukuyama, *J. Phys. Soc. Japan*, **50**, 2516 (1981).

[103] G. Bergmann, *Phys. Rep.* **107,** 1 (1984).

[104] B. L. Altshuler, A. G. Aronov, M. E. Gershenson, Yu V. Sharvin, *Sov. Sci. Rev., Sect. A* **9**, 223 (1987).

[105] A. Sergeev, M.Yu. Reizer, and V. Mitin, *Phys. Rev. Lett.* **94**, 136602 (2005).

[106] J. Liu and N. Giordano, *Phys. Rev. B* **47**, 9693 (1993).

[107] A. G. Aronov and Yu. V. Sharvin, *Rev. Mod. Phys.* **59**, 755 (1987).

[108] A. Bachtold, C. Strunk, J.-P. Salvetat, J.-M. Bonard, L. Forro, T. Nussbaumer & C. Schönenberger, *Nature* **397**, 673 (1999).

[109] B. L. Altshuler, A. G. Aronov, and B. Z. Spivak, *JETP Lett*. **33**, 94 (1981).

[110] S. M. Huang, T. C. Lee, H. Akimoto, K. Kono, and J. J. Lin, *Phys. Rev. Lett.* **99**, 046601 (2007).

[111] A. Sergeev and V. Mitin, *Phys. Rev. B* **61**, 6041 (2000).

[112] Y. L. Zhong, A. Sergeev, C. D. Chen, and J. J. Lin, *Phys. Rev. Lett.* **104**, 206803 (2010).

[113] J. Liu and N. Giordano, *Phys. Rev. B* **43**, 3928 (1991).

[114] J. J. Lin, T. J. Li, and T. M. Wu, *Phys. Rev. B* **61**, 3170 (2000).

[115] J. F. DiTusa, K. Lin, M. Park, M. S. Isaacson, and J. M. Parpia, *Phys. Rev. Lett.* **68**, 1156 (1992).

[116] J. T. Karvonen and I. J. Maasilta, *Phys. Rev. Lett.* **99**, 145503 (2007).

[117] D. S. Yang, C. Lao, A. H. Zewail, *Science* **321**, 1660 (2008).